CHARACTERIZATION AND IN-PROCESS METROLOGY OF A LASER POWDER FUSION ADDITIVE MANUFACTURING MACHINE

by

William S. Land II

A thesis submitted to the faculty of
The University of North Carolina at Charlotte
in partial fulfillment of the requirements
for the degree of Masters of Science in
Mechanical Engineering

Charlotte

2015

Approved by:

_____
Dr. John Ziegert

_____
Dr. Jimmie A. Miller

_____
Dr. Tony Schmitz

ABSTRACT

WILLIAM S. LAND II. Characterization and in-process metrology of a laser powder fusion additive manufacturing machine. (Under the direction of DR. JOHN ZIEGERT)

Laser powder bed fusion is one of the most commonly used processes by which metal parts are produced through an additive manufacturing approach, and it is currently the topic of extensive research. This paper describes the study of two aspects of the laser powder bed fusion process through the testing of a prototype fusion chamber produced specifically for research purposes.

The laser fusion system studied herein utilizes a 2-axis galvanometer scanner system as a means of manipulating the planar position of a laser spot to produce sintering of the powder bed. As the scanner is the primary means of creating relative motion between the laser spot and the powder bed, its performance directly impacts the dimensional accuracy of the final part. As such, one aspect of the laser powder bed fusion process studied and discussed in this paper is the characterization of the scanner's ability to accurately position the laser spot over the powder surface.

The second aspect of the fusion process studied herein is the ability to collect in-situ data on the powder surface immediately before and after the fusion process as a means of improving the understanding of the process and for characterization of the part being produced. The complex metal parts produced by such processes are often very difficult to dimensionally characterize after the build process is complete. Therefore, it is valuable to the industry to measure each layer of the build process, while features that may eventually be obscured are still available for interrogation. This paper describes the development of a metrology system which performs areal height measurements of the powder surface to dimensionally characterize final part geometry on a layer-by-layer basis.

ACKNOWLEDGEMENTS

First and foremost, I'd like to acknowledge my research partner and colleague, Bin Zhang, for his unending work ethic and help in this project. So much of what is presented here was accomplished primarily at the labor of his hands and mind. There is little doubt that this project would have mired and failed without him. Secondly, I'd like to thank my advisory professors, Dr. John Ziegert and Dr. Angela Davies for their constant support, advice, and direction throughout the entirety of this project. I'd also like to thank my lab colleagues for their patience and willingness to help whenever asked along the way, in particular Dr. Christopher Tyler and Mr. John Troutman for their hours of machining assistance. Lastly, I would like to thank God and my parents, Cathy and Ron, for affording me the ability to be here in uncountable ways. To borrow a line from Alex Slocum, "…to the Almighty who gave us our curiosity and our puzzles, who gave us the ability to create or stagnate, who we must not let down" [6].

TABLE OF CONTENTS

LIST OF FIGURES

LIST OF TABLES

CHAPTER 1: INTRODUCTION

1.1 Laser Powder Bed Fusion Process

Additive manufacturing processes, although not a new concept, have been at the forefront of manufacturing research in recent years. Due to a myriad of technological and economic developments, industrial interest in additive manufacturing (or rapid prototyping) and its potential to revolutionize the field of engineering design has drastically increased across nearly all industry sectors. Investment in the development of the technology has likewise risen dramatically, as displayed below in Figure 1.1, showing the sales of additive based manufacturing machines over the last few decades as tracked annually by the Wohlers Report. Sales of additive manufacturing technology and related products is expected to exceed $3.6 billion dollars globally by year end of 2015 [1].

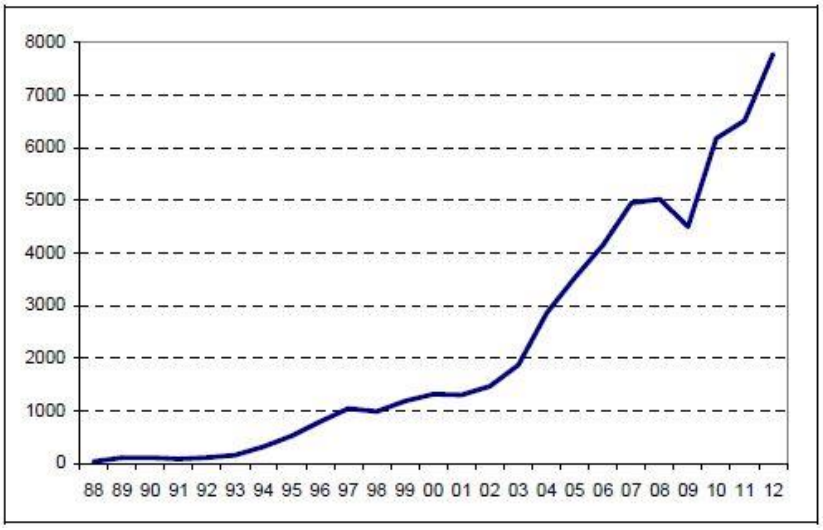

Figure 1.1: Estimates of units of industrial machines for additive manufacturing sold worldwide [1].

Much of the additive manufacturing research being done of interest to the precision engineering sector is in metal additive technologies. Recent improvements in metal additive manufacturing processes have generated massive opportunity for novel engineering within the design and implementation of precision, high functionality components. Many industries aim to take advantage of the assets metal additive manufacturing offers. However, to fully realize these potential benefits, further improvements are needed in all aspects of additively produced parts, from their metallurgical properties to their dimensional accuracy and surface finish.

One metal additive process needing improvements, which is the focus of this document, is laser powder bed fusion. The investigation of this particular additive manufacturing process has been motivated by several federal and industrial sponsors, but is primarily supported by the America Makes – National Additive Manufacturing Innovation Institute. As a collaborator, Edison Welding Institute in Columbus, Ohio, has built a working open source fusion chamber for the purpose of sensor integration and testing. The laser powder bed fusion process involves the direction of a focused laser beam via a galvanometer laser scanner over a flat bed of metal powder. As the laser beam is manipulated, the area of powder over which it traverses is fused together, forming a thin layer of solid metal. This metal/powder layer rests atop a build platform that then is lowered a nominal distance to prepare space for a new layer of powder. The new layer of powder is then spread across the previously fused layer, and a new area is then exposed to the laser beam. This process repeats, and in this fashion a part can be built up layer wise. A cartoon of the build process is shown below in Figure 1.2 [2].

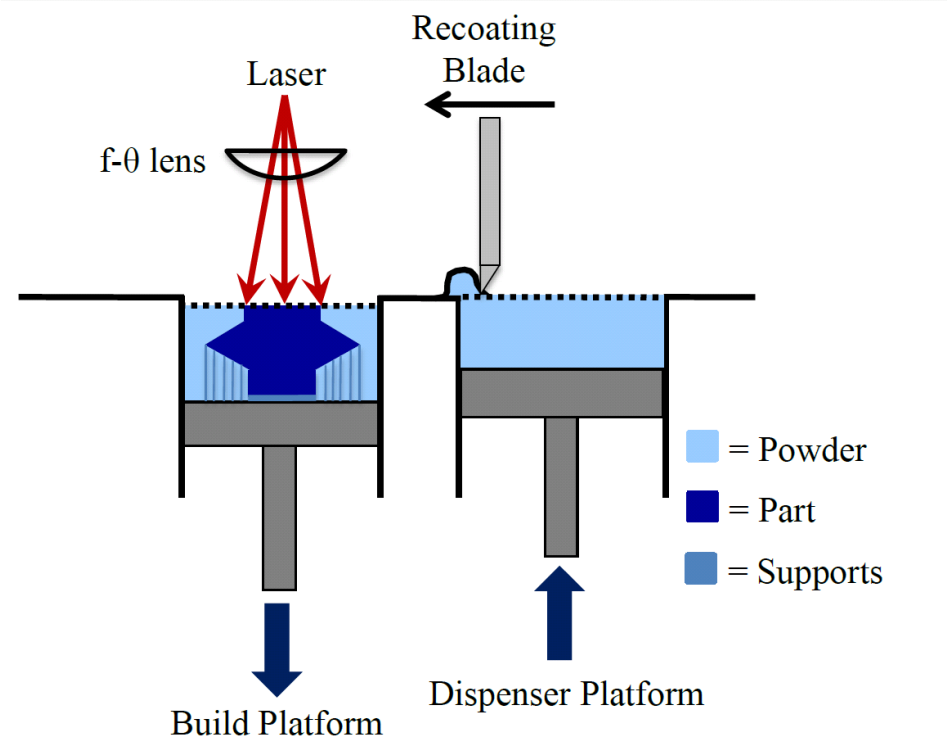

Figure 1.2: Schematic of the typical build process inside a laser powder fusion bed. Figure is curtesy of NIST Internal Report 8036 [2].

One of the many challenges associated with producing high precision parts additively, in particular understanding and improving their dimensional accuracy, is the relative inability to measure them by conventional means after they have been manufactured. Some of the most powerful advantages of producing parts with an additive process are the ability to include atypical geometries and complex internal structures within a design. Both of these hinder efforts to perform metrology on a completed part with many standard measurement tools. Current technologies produce surface finishes that are often much too rough to perform scans with a traditional touch probe without causing damage; key features are often obscured from view and inaccessible; internal structures are nearly impossible to measure with almost any contact or non-contact measurement approach outside of x-ray tomography which is very costly and complicated. Simply put, if a part can be readily

measured by common devices, whether contact or non-contact, it is likely readily made with a traditional machine tool, and is therefore likely an inappropriate candidate for additive manufacturing due to the current economic disadvantages of the technology. As such, measurements must be carried out during the manufacturing process, while all features are still accessible to probing, in order to fully characterize a part's geometry.

As a result of the layer-wise build process, the dimensional characteristics of a part are manifested in the boundary between areas that have been fused into solid metal and areas of unfused powder in each layer. Determining this boundary with high fidelity immediately after the lasing of each layer amounts to measuring a profile of the outer surface of the final part at the layer's respective height within the total build. Therefore, determining the solid-powder boundary for every layer sequentially allows for the boundaries of the entire part to be created by digitally stacking the individual layer boundaries, ending in characterization of all surfaces by profile lines at a resolution of the build layer thickness. In addition to mapping each layer of the part as it is being made, monitoring the area height profile of each layer is expected to provide insight into other quality issues such as splatter of molten material, interstitial void formation due to bubbles, and general information on the surface structure of the powder bed.

1.2 Project Scope

1.2.1 Characterization of Laser Spot Motion

Typically, laser powder fusion bed systems use a galvanometer laser scanner to direct the laser beam over the powder surface. Such is the case in the powder fusion chamber studied here. One of the deliverables of this project is to characterize the motion of the laser spot at the powder surface. It is valuable to both part designers and operators to know

the capability of the machine used to produce parts, and in this fusion bed, the laser scanner is the primary instrument of concern when it comes to geometrical part accuracy during the build. Specifically, this project aims to characterize the static placement accuracy of the laser spot throughout the portion of the scanner's field of view where part builds are taking place. The laser scanner system, its error sensitivities, and the testing procedure used to characterize its accuracy will be discussed in more detail in Chapter 2.

1.2.2 In-Situ Metrology System Development

As stated, there is potentially great value in the ability to measure each sintered layer during the build process. As a result, the second major deliverable of this project is the development of an areal surface metrology system for the explicit measurement of each powder layer during every step of the laser powder fusion build process. The approach to measuring each layer described here involves the combination of a traditional machine vision system and a digital fringe projection system.

The fringe projection technique is used to calculate the area height profile of each layer, while a machine vision algorithm provides the proper lateral mapping from camera pixels to in-plane object coordinates. The process involves the use of one digital single-lens reflex (SLR) camera and a digital light processing (DLP) projector. Three cameras have been integrated into the fusion chamber for the purpose of future advancement of the measurement process. The availability to measure the powder surface from multiple angles will provide means for a more robust measurement as the project progresses.

Potentially, the areal surface measurements could be used to differentiate fused powder from unfused. As previously stated, this could lead to full 3D characterization of the built part. The primary means of determining the solid-powder boundary within each sintered

layer of a build would be the through observed relative height changes in the powder surface. The laser powder bed fusion system studied here uses IN625 nickel alloy powder as its printing media. The solidification of this particular powder by sintering causes approximately a 40-50% increase in density. Therefore, the powder regions exposed to the laser during sintering will experience a measureable drop in height as compared to the unaltered regions. By comparing the surface profile of a layer after sintering to a baseline area profile of that same layer prior to laser exposure, it is thought that one might distinguish solidified area from powder by examining relative height change. As noted, the measurement of lateral and vertical coordinates within the powder bed occur independently of each other, and as such, each requires its own calibration and data processing procedure, as will be discussed in detail in future chapters.

1.3 Literature Review

There is a plethora of research currently being conducted on all aspects of the laser powder bed fusion process. A variety of institutions are interested in everything from the material characteristics of built parts and their correlation to build parameters, to qualification and standardization of various aspects of the process for its transition into highly regulated industries. Mani et al. break down current research in the field into three subcategories. The categories include control schemes currently used in additive manufacturing, manufacturing process measurements, and modeling and simulation [2]. The work conducted in this project falls squarely into the process measurement category.

Mani subdivides the process measurement category of research in additive manufacturing into pre-process measurements, in-process measurements, and post-process measurements [2]. Pre-process measurement research includes work on the

characterization of different powder production techniques, such as that performed by Slotwinski and Simchi, and structural characteristics of metal powder as it is fused together such as that done by Xiao and Zhang [3-5]. Little research work is being done on the actual characterization of the machine tool components, as this work has been well developed and published for many years. While it is still a necessary pre-process measurement, there are no notable recent publications on rigid body error measurements. Textbooks, such as Slocum's Precision Machine Design, and many other have thoroughly laid out the best practices for machine tool measurement and the implications of machine tool errors on many systems [6].

Research being conducted in the in-process measurement category is much more limited. Several groups are performing in-process thermography measurements using infrared thermal cameras. Moylan, Dressler, and Dinwiddie are just a few examples of this type of work [7-9]. The majority of the in-process measurement work underway now is focused on characterizing the melt pool temperature and size as it moves during the build process. This information is largely pertinent to the mechanical properties of the fused material, but not necessarily the geometrical qualities of the part. In this way, the work presented herein fits in a relatively rare category of in-process measurements.

Finally, post-process measurement research currently underway can be described by several additional subcategories, primarily the mechanical properties and the geometric accuracy of the output part. Several groups are currently working on artifact designs meant to test machine performance over a range of different part feature types. Some of the most in-depth work done in the design of standardized test artifacts is that being carried out by Moylan et al. at the National Institute for Standards and Technology [10]. However, they

are certainly not the only group developing test artifacts for standardization of post-process machine performance testing. The machines performance is characterized by the geometric accuracy of the artifact, whose measurement is in itself a research area. Groups such as Bauza et al. are using computed tomography measurements to do such geometrical characterization with varied success [11]. Lastly, a large volume of research is being conducted on the post-process mechanical properties of the metal parts that are produced via laser fusion. Kruth and Gibson are two examples of this work, and there are many more [12, 13].

In summary, there is a tremendous volume or research currently being conducted in relation to metal additive manufacturing. Specifically the laser powder bed fusion processes is drawing much attention from the research community, as would be expected by the high level of global investment in the industry. Although there is much work being done in both pre-process and in-process measurement strategies, the machine characterization and areal surface metrology system described herein still provide valuable insight into laser powder bed fusion processes.

CHAPTER 2: MACHINE CHARACTERIZATION

As with all machine tools, the creation of parts which conform to dimensional specification is largely a function of precise, accurate, and deterministic control over the relative motions of the key machine components. Not unlike traditional three axis subtractive machine tools, each laser powder bed fusion chamber consists of motion axes which can be analogously compared to the nominally orthogonal XYZ coordinate system with which the manufacturing industry is intimately familiar. Therefore, error motions of the components of the machine, when unaccounted for, impart inaccuracies in the resulting part geometry. Additionally, the laser powder bed fusion manufacturing approach incorporates the added complexities of transforming spherical coordinates into planar Cartesian coordinates via a lens assembly within the laser scanner assembly. Needless to say, metrology and characterization of the key motion components within the powder bed fusion system is necessary in order to achieve the high level of dimensional conformity sought by the modern industrial marketplace. The key motion axes in a laser powder bed fusion chamber are, in ascending order of influence on part accuracy, the powder recoating arm, the build platform (Z-axis analog), and the laser scanner system (X & Y-axis analog).

For the purpose of this report, the powder recoating arm and build platform components will only be referred to with respect to their potential impact on part geometry. The scope of this project, as previously stated, did not include the investigation of these components in a quantitative sense, and therefore, they are only being discussed here qualitatively.

2.1 Key Component Description

2.1.1 Powder Recoating Arm

As described in Section 1.1 above, the powder recoating arm is responsible for recoating the exposed fused surface of the unfinished part with fresh powder. Although this may seem like a relatively trivial task, the uniformity of the thickness as well as the surface profile of the new powder layer can impact the part's geometry and material characteristics. The volume of powder distributed above the already fused area will determine the volume of fused material added in each lasing operation. Variations in powder thickness will therefore lead to local height variations on the upward facing surface of each fused layer. These variations will be imprinted into surface features on any upward facing surface in the final part. Additionally, relative thickness variations of the powder can impact the necessary laser power density required for proper material fusion, causing variations in the quality of material fusion. The local height variations in the powder surface will also impact the lateral accuracy and precision of the laser spot placement by the laser scanner. This fact will be discussed in more detail below. More importantly than random thickness variations, however, are systematic variations in powder distribution thickness, such as a wedge distribution or waviness. These will likewise cause a corresponding systematic variation in local height of the fused surface. Due to the layering process, systematic powder thickness variations can accumulate into larger corresponding geometric errors in the final part.

In the case of the open source powder fusion bed being studied herein, there are several rigid body error motions of concern in the linear motion axis responsible for moving the powder recoating arm. The stage, in this case, is a ball-screw driven linear actuator

mounted on the back wall of the powder fusion chamber. An aluminum bracket constitutes what has been described here as the powder recoating arm. As seen below in Figure 2.1, the arm is extended a substantial distance from the center of stiffness of the stage carriage's bearing supports within its body, producing what is commonly referred to as abbe offset. Additionally, it is supporting a heavy load of manual adjustment positioners, sensors, and recoating hardware. As a result, the roll error motion of the carriage will be exaggerated by this loading and abbe offset, likely causing significant unwanted vertical (Z-axis) motion of the recoating blade tip. Likewise, flatness error motions of the stage's carriage will combine with those created by the roll of the carriage and the sum has the potential to create the substantial local thickness variations in powder referred to above as problematic. In the interest of producing the most accurate parts, these two rigid body errors should be characterized and minimized to an acceptable level so as to not impart intolerable variations in each layer of distributed powder.

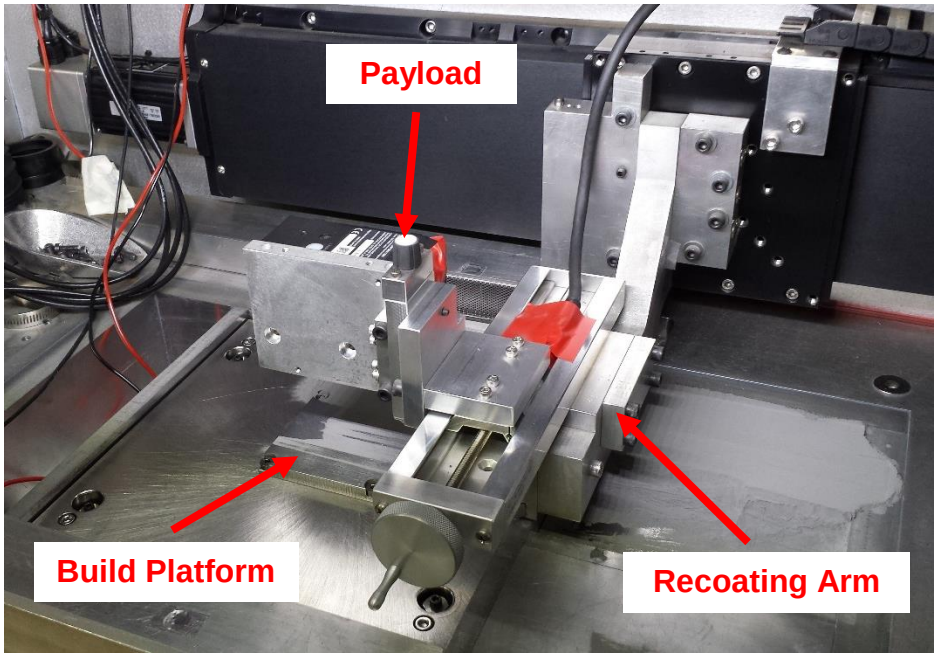

Figure 2.1: Image of powder recoating arm traversing the build platform. Notice the large payload and substantial cantilever off of the motion stage to which it is attached.

2.1.2 Build Platform

The axis of motion carrying the build platform is also a ball-screw driven linear actuator mounted vertically below the chamber housing. Just as in the case of the powder recoating arm, the build platform has several rigid body error motions which will impact the accuracy of geometric features in the final part. These influences, however, can be much larger as the build platform is responsible for maintaining the orientation and relative position of each subsequent layer throughout the build process. Since the area of the powder fusion is determined by the path of the laser spot within the scanner's field of view and this field of view remains static with respect to its position within the build chamber, any and all unwanted motion of the build platform relative to the static focal plane of the laser scanner system will directly cause geometric errors in the part. Unfortunately, all of the error motions of the build platform are of concern as a result. Each will cause its own part errors of varying severity. For instance, scale errors in the stage's motion will induce the variations in powder layer thickness described above. More drastic illustrations of how the build platform's error motions will impact the part's geometry are demonstrated below in Figure 2.2. As with the powder recoating arm, the build platform's error motions should be characterized and their effects minimized to an acceptable level if high accuracy geometric control of built parts is of interest.

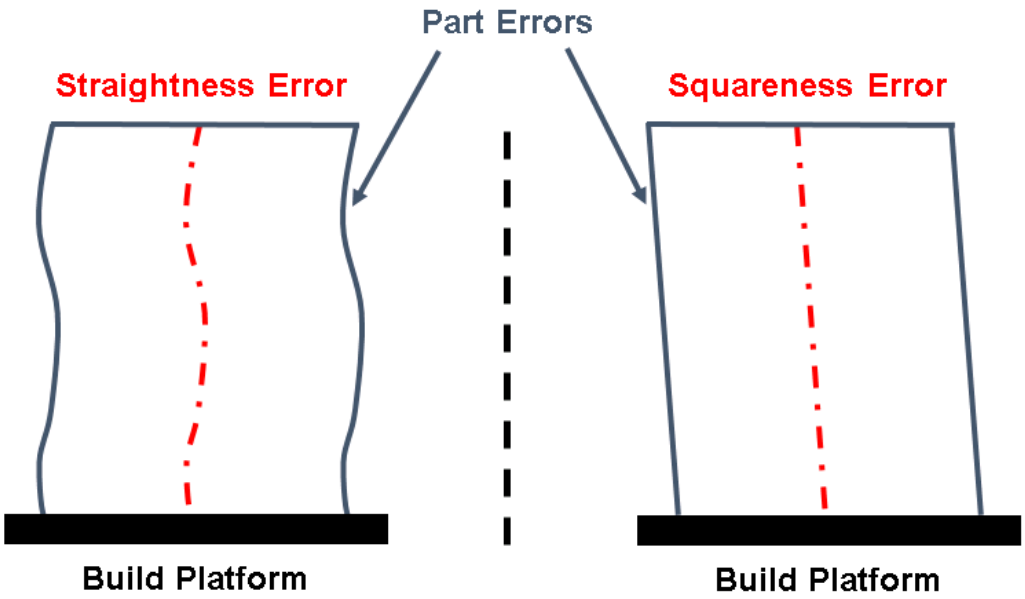

Figure 2.2: Schematic showing that the build platforms two directional straightness error is imprinted directly on the side walls of the part being built (left), and that a squareness error in the alignment of the build platform's stage relative to the laser axis will also directly result in part perpendicularity errors (right).

2.1.3 Laser Scanner

The laser scanner consists of two galvanometer motors with mirrors attached to their shafts. These galvanometers are situated in a housing in such a way that when a laser beam is passed into the housing the rotary motions of each mirror cause independent linear motion of the projected laser spot at a plane below the scanner. A simplified depiction of two galvanometer motors arranged as described is shown below in Figure 2.3. This arrangement allows for rapid motion control of the laser spot through the magnification of the mirrors' controlled motion via a large lever arm. As these mirrors and rotors are designed to have extremely high stiffness to inertia ratios, fast rotary control of the galvanometer motors can lead to dramatic dynamic performance of the laser spot in the XY-plane in which it is projected. However, there are several complexities that arise from using such a devise for in-plane 2D motion control.

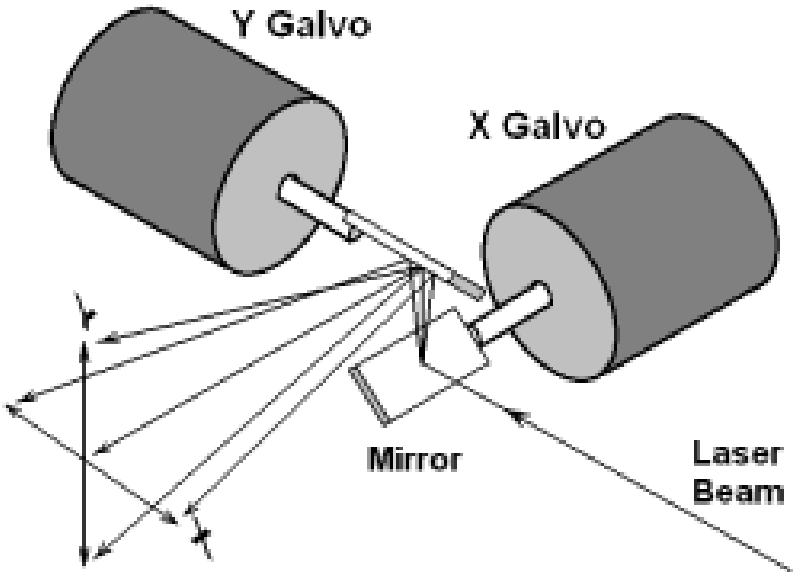

Figure 2.3: Simplified schematic of a galvanometer scanners principle of operation.

First, due to the offset in the mirrors' locations in the beam path, the projection of the laser beam onto a plane does not constitute rectilinear motion as shown by Figure 2.3. As a result of increased projection distance as the laser spot is directed through the range of travel, the actual projected area covered by the beam will look like Figure 2.4. This 2D profile is solely a result of the practical necessity of two, single degree of freedom axes rather than an idealized single axis with two degrees of freedom. This distortion from the desired projected coverage of laser travel could be easily calculated and corrected for on the surface. Unfortunately it combines with a more important complexity in scanner systems which arises from focusing the laser beam.

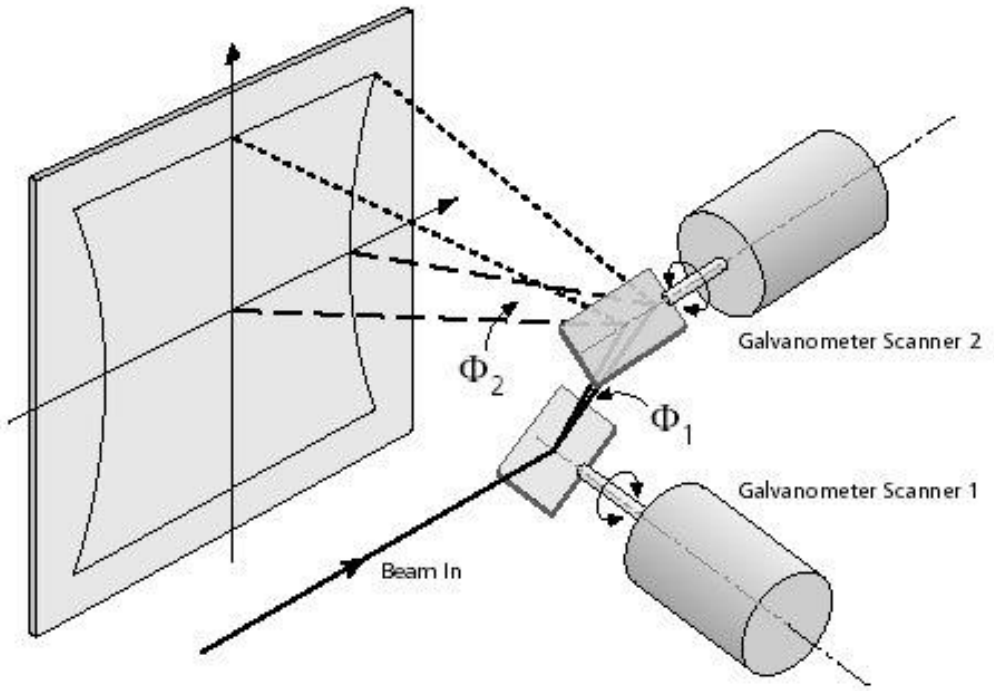

Figure 2.4: Demonstration of the distortion imparted to the planar motion of the laser spot due to offset mirror locations within a galvanometer scanner.

Laser beam focus in two axis scanner systems requires the use of an f-theta lens, also known as a field flattening objective, placed in the optical path after the galvanometer mirrors. Since the laser beam is being directed through an arc by the galvanometer mirrors, a simple focusing objective would cause the beam to focus on a hemispherical surface. As planar laser processing is desired, a more complicated lens arrangement must be used to focus the beam on a plane. Focusing on a plane requires that the focal length of the lens assembly increase as the incident angle of the incoming beam increases. The increase in focal length compensates for the added length of beam path as the laser is directed at a non-normal incident angle to the surface where processing is desired. The term "f-theta lens" means that the focal length, "f", is a function of the incoming beam angle, "theta", to the input aperture of the lens. Lens manufacturers provide what is called an Effective Focal Length (EFL) which can nominally be multiplied by the angle of the incoming beam to the

lens in radians to determine the lateral projected distance of the laser spot in the specified focal plane. This lateral projected distance is specified relative to where a normally incident beam to the lens is projected in the focal plane. The distance from a datum surface on the lens to the focal plane is also specified, allowing end users to integrate the scanner-lens system into a machine such that the focal plane coincides with the desired processing plane.

Although the use of an f-theta lens allows for planar laser processing, the lens causes substantial distortion of both the laser spot's lateral placement within the focal plane and its power density profile. These will have large impacts on the accuracy and success of laser processing to be done by the scanner. The distortion due to the f-theta lens combines with the distortion depicted in Figure 2.4 to create a total planar distortion that resembles that in Figure 2.5, below, often referred to as barrel-pincushion distortion. Although the barrel-pincushion distortion is actually the combination of mirror offset and the lens elements, this distortion is commonly referred to as theoretical lens distortion within the scanner industry; therefore, from here on the distortion depicted in Figure 2.5 will be titled theoretical lens distortion with the acknowledgement that not all components of it are caused by the f-theta lens. The scanner unit's manufacturer will typically provide a correction to be implemented in order to remove the theoretical ideal lens distortion shown in Figure 2.5. However, this theoretical correction is never completely valid due to laser alignment issues discussed later, in Section 2.3.4. Therefore, the residual distortion in the beam spot's lateral position within the focal plane must be measured and additionally corrected in order for any scanner system to produce accurate process results.

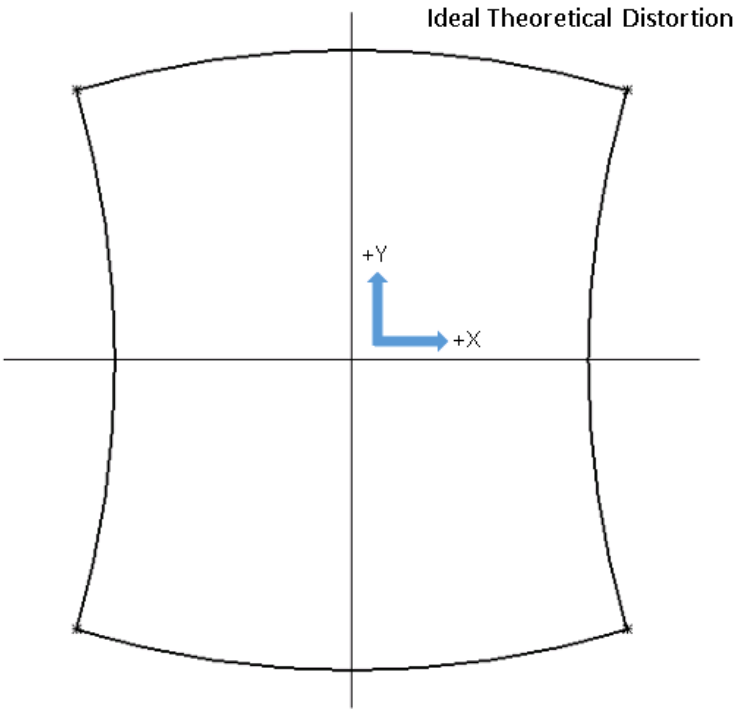

Figure 2.5: Generalized shape of ideal theoretical planar distortion of laser spot motion when an f-theta lens is used in conjunction with a galvanometer scanner.

As discussed in Section 1.2, characterizing the laser spot placement errors at the build plane of the scanner being used within EWI's laser powder bed fusion chamber is one of the primary objectives of this project. The remainder of this chapter will discuss error sensitivities in scanner systems and how they will potentially cause laser spot placement errors during the fusion chamber's use. Additionally, the approach used to measure the actual laser spot's motion and the results of that testing will be presented and discussed.

2.2 Mark & Measure Technique

The principal and most popular characterization and calibration technique used for nearly all laser processing systems is to mark patterns on a material, measure the pattern in the global space, and to use the difference between each mark's desired and measured location as a correction factor in future commanded moves with the system's controller. This approach is known colloquially as the "mark-and-measure" technique, and, for

reasons beyond the scope of this paper, was determined to currently be the most practical and viable method of characterizing the laser scanner and f-theta lens system being used in the fusion chamber. The specific procedure used to measure the scanner's performance is covered in detail in Section 2.4, but it involved the marking of coated glass substrates within the chamber and the use of a microscope measuring machine to investigate the marked substrates produced by the fusion chamber. Grid patterns were burned into the substrates over various areas of interest within the scanners field of view in order to get a clear picture of the scanner system's ability to position the laser spot as commanded by the controller. The data taken by the microscope measuring machine were appropriately post processed and turned into two dimensional error arrays. Commonly, these error arrays are collected for the purpose of implementation into a correction file in the scanner's controller. Upon doing so, subsequent substrates can then be marked and measured to determine the effectiveness of the correction file. This correction process was not carried out in this project, as the means were not present to actively interact with the scanner's control architecture. However, there are a number of factors that determine the potential marking accuracy a particular scanner system is capable of achieving, all of which are vital to understand in order for the laser powder bed fusion system to eventually manufacture precision parts.

2.3 Error Sensitivities in Galvanometer Scanner Systems

The accurate marking of substrates and therefore the accurate processing of metal powder is affected by several factors involving the physical setup of the fusion chamber. Marking field to focal plane parallelism, working (marking) height consistency, process flatness, and input beam alignment consistency all will influence the resultant accuracy,

and marking consistency of any laser processing. Unfortunately, these factors are not mutually exclusive, and their independent effects on the lasing process are not easily differentiated, and often combine. As a result, each is specifically defined and its impacts on process accuracy described below, in order to clarify their individual importance to the use of the laser scanner in EWI's powder bed fusion chamber. Previous validation of the error sensitivities discussed was published by Land in 2014 [14].

2.3.1 Marking Field & Focal Plane Parallelism

As used in this document, the "marking field" is defined as the planar surface on which the laser beam is intended to mark; in this case, the marking field is the build plane, or the upper surface of powder that is deposited by the recoating arm. Additionally, the "focal plane," as described above, is defined as the virtual plane over which the f-theta lens focuses the laser beam; it is bounded by the available scan area of the particular scan head/lens combination in use. The parallelism of these two planar surfaces is defined here as the magnitude of the angle between the normal vectors of each plane, and when referring to the effects of this parallelism, it is assumed that the centroid of each plane is coincident with one another and that both are perfectly flat. Through previous testing, the alignment of the two was found to have an impact on the spot placement accuracy, and therefore, the scanner's effectiveness in high accuracy powder fusion.

As the input beam is directed through travel by the scanner, it inherently has an incident angle greater than zero as it falls on the focal plane (except for where the beam enters the lens coincident, and parallel to the lens' axis.) Any misalignment between the marking field and focal plane causes the beam to be projected a distance that is different than the

intended working height, and, as a result of the non-zero incident angle at the focal plane, a linear marking error is induced on the marking field as shown below in Figure 2.6

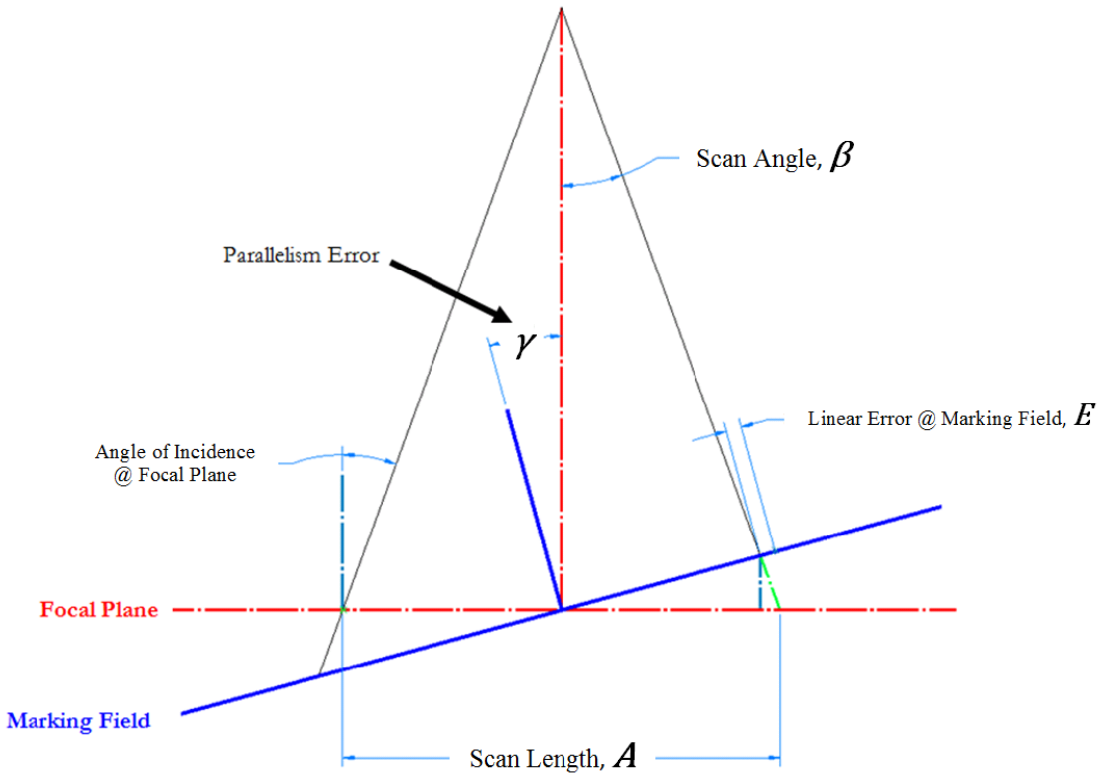

Figure 2.6: A simplified representation of marking field and focal plane misalignment showing an induced, linear laser spot placement error at the marking field.

The total (pk-pk) induced error over the marking field from a parallelism error can be approximated using the terms in Figure 2.6 as:

$$E_{Total} = \frac{A}{\cos(\gamma)}(1 - \tan(\gamma)\tan(\beta) - \cos(\gamma)) \quad (1)$$

Given that the output scan angle of the laser beam at any given location in the focal plane is roughly dictated by the lens' f-theta relationship as previously discussed, the angle can be approximately expressed as a function of spot location in the focal plane in terms of vector distance from the centroid of the plane. Figure 2.7, below, shows the approximation of parallelism induced error for one axis of scanner motion over the full field of view for the lens and scanner in use by the laser powder bed fusion chamber.

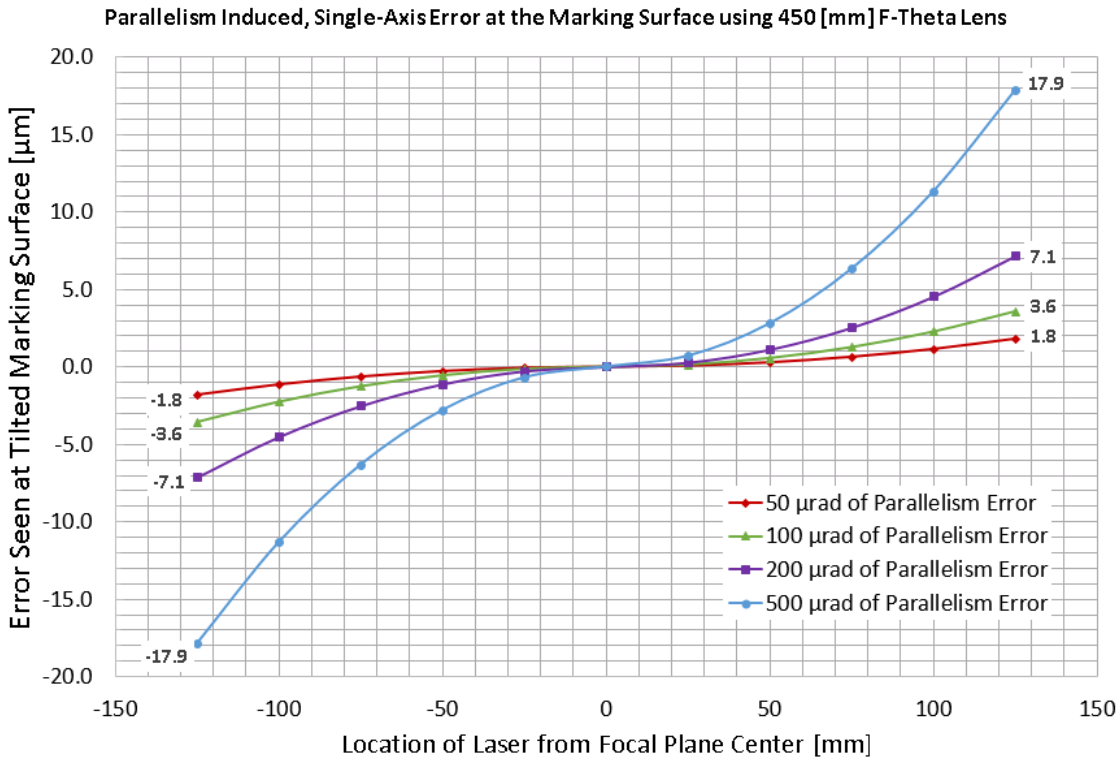

Figure 2.7: Theoretical, parallelism induced, laser spot placement error approximation for the laser scanner and f-theta lens combination employed within the EWI laser fusion chamber. (Error is defined as the difference between the magnitude of a uni-directional move seen in the marking field's coordinate frame, and the magnitude of the same uni-directional move as commanded in laser scanner coordinates.)

As long as the angular alignment between the marking field and focal plane is consistent from part to part, its effects on marking accuracy can be calibrated quite effectively if desired. However, any inconsistency in their alignment directly creates a non-repeatability in marking accuracy described by the same relationship shown in Figure 2.7. Most commonly, inconsistency in the alignment of the marking field and focal plane is introduced by the part being marked (the marking field.) In this specific case, the misalignments and motion errors of the powder recoating arm will dictate the parallelism of the marking field (powder surface) and the focal plane of the f-theta lens. The magnitude of the tolerance deemed acceptable for the recoating arm's parallel motion to the focal

plane depends on the level of desired spot placement accuracy. However, the realization of this tolerance is difficult in practice, as the exact location and orientation of the focal plane is impossible to know. Best practice dictates that the necessary parallelism be applied between the mounting datum surface of the f-theta lens at the laser scanner and the average linear motion of the powder recoating arm.

An additional concern arises if large misalignment exists between the marking field and the focal plane. Large misalignments between the scanner's focal plane and the powder surface, as shown earlier in Figure 2.6, will cause the effective working height to change through travel. This can cause the laser spot to go progressively out of focus as the beam is directed through the extent of travel. The extent to which parallelism errors between focal plane and marking field affect focus depends on both the range of incident angles produced by the lens assembly, the level of misalignment, and the focal depth of the lens assembly. With the specific hardware being investigated here, the focal depth of the lens assembly is large enough that it is unlikely that misalignments will lead to beam defocus. Some quick tests showed depth of focus for the f-theta lens in use to be greater 0.5 [mm], which would equate to a parallelism error of 4 mrad, or nearly 900 arc-seconds of angle.

2.3.2 Working (Marking) Height Consistency

Similar to errors caused by marking field and focal plane misalignment, errors can be induced when the marking field is placed at a different distance from the lens than the theoretical location of the focal plane. In the case of the laser fusion chamber, these types of errors will result from improper installation height of the powder redistribution blade and potentially improper placement of the powder surface by the build platform. As

discussed here to isolate height variation's effects, the marking field and focal plane are assumed to be perfectly flat and parallel, but are separated by a constant offset in the direction of the lens axis. Errors induced by this height differential are once again a result of a non-zero incident angle of the laser beam at the focal plane, as seen in Figure 2.8 below.

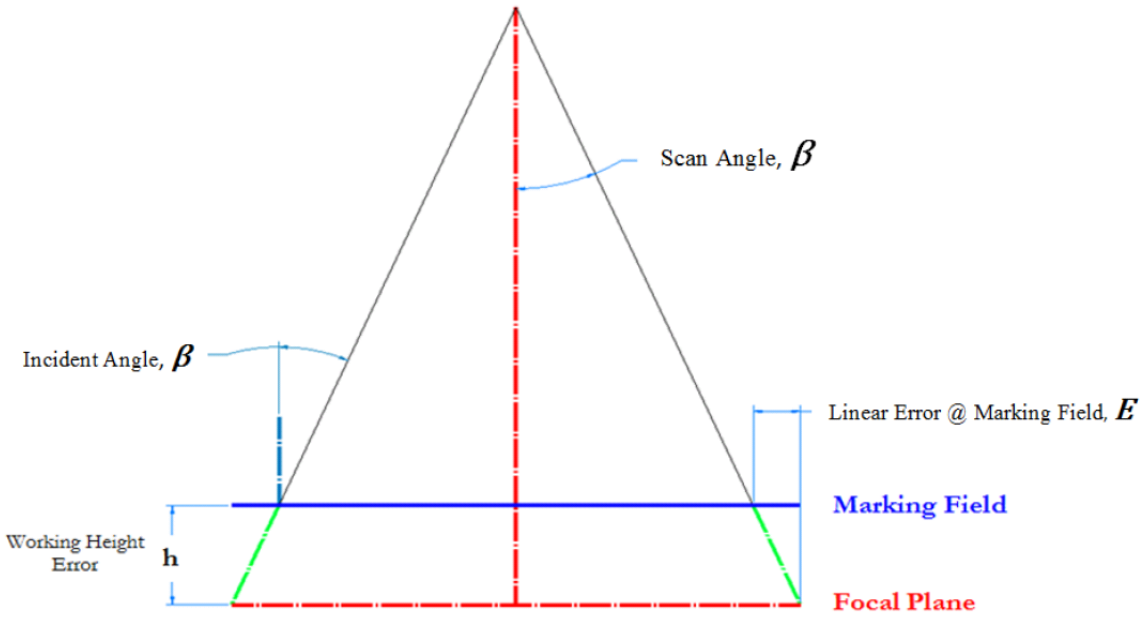

Figure 2.8: A simplified representation of a marking field and focal plane height differential showing the induced, linear laser spot placement error at the marking field.

The total (pk-pk) induced error over the marking field from a working height error can be approximated using the terms in Figure 2.8 as:

$$E_{Total} = h * \tan(\beta) \quad (2)$$

Once again, the output scan angle from the lens can be approximated by the F-Theta relationship of the lens, and, therefore, an approximation of marking error induced by working height error can be made over the entire field for the specific lens in use by the fusion chamber. See Figure 2.9 below.

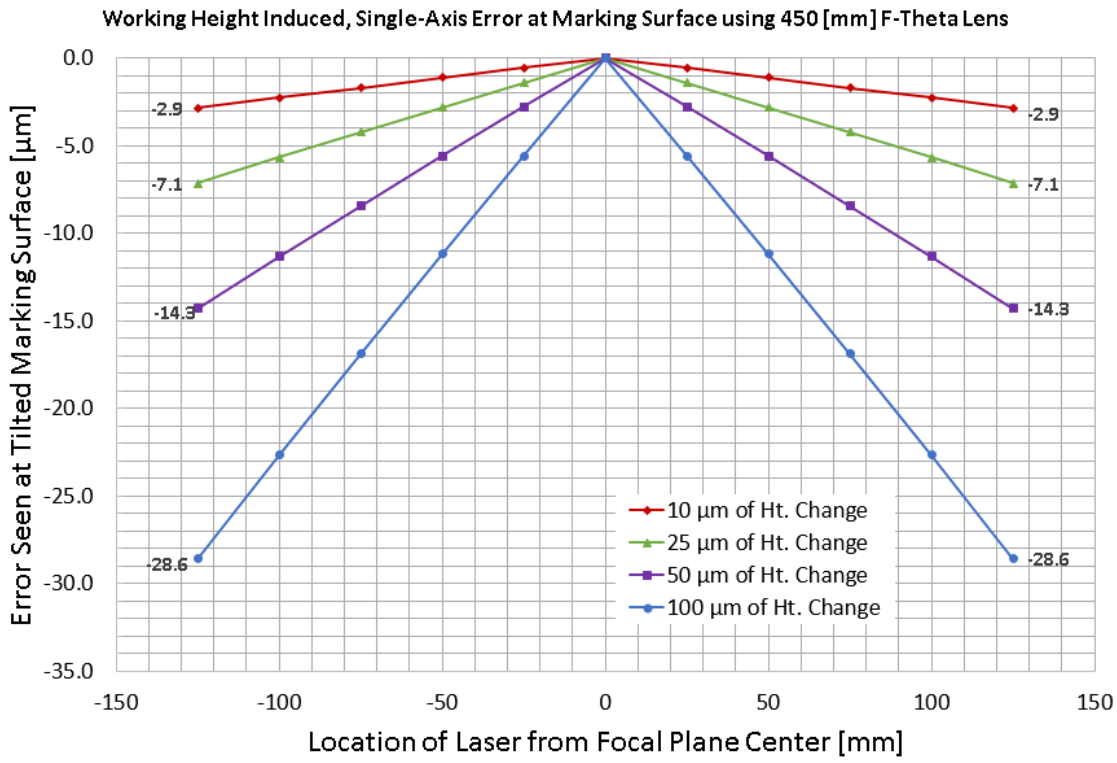

Figure 2.9: Theoretical approximation of error induced by changes in working height for the specific laser scanner and f-theta lens combination employed in the EWI laser fusion chamber. (Error is defined as the difference between the magnitude of a uni-directional move seen in the marking field's coordinate frame, and the magnitude of the same uni-directional move as commanded in the laser scanner coordinates. A positive height change is defined as the marking field moving toward the f-theta lens.)

As before, while the offset between the marking field and focal plane remains constant, its effects on marking accuracy can also be calibrated very effectively. However, it is important to note just how sensitive marking accuracy can be to changes in working height. In the case of the fusion chamber, the f-theta lens causes a large maximum scan angle (>15 degrees), where a change in height as small as .001" [0.025 mm] can induce substantial marking error, upwards of .0003" [0.007 mm].

Just as in the previous section, marking accuracy's high sensitivity to height changes is vital for the operator of the laser fusion chamber to appreciate. The thickness tolerance of the individual build platforms loaded into the chamber for each subsequent build, if not

individually measured and accounted for, will substantially add to non-repeatability in laser spot placement accuracy. The same care should be applied to establishing the height of the recoating arm's blade relative to the f-theta lens' datum mounting surface. The conversion in the controller from rotary angles of the galvanometer mirrors to lateral laser spot displacement is only valid at the exact focal plane height. Any offset in the blade's height from the focal plane will cause what is analogous to a relative scale error in spot placement dictated by Eq. 2.

A significant offset between the marking field and focal plane is more likely in cases where the depth of focus of the lens assembly is substantial. Unfortunately, this is precisely the case in the scanner system employed by the laser powder bed fusion chamber used in this investigation. Typically, a focusing routine is performed prior to establishing the marking field's location to ensure that it is coincident with the focal plane, thus setting the working distance for the given process. Since the depth of focus of the system in question is so large, it becomes difficult to precisely locate what in this case is the position of the powder recoating arm before a mark and measurement procedure has taken place. It is then also difficult to retroactively go back and adjust hardware heights if such adjustments have not already been built into the design. As mentioned before, these errors can be corrected in software as long as the height offset of the marking field remains constant. At the very least, it is important to account for small variations in build platen thickness at the start of each build when operating the laser fusion chamber.

2.3.3 Process Flatness

Flatness, in terms of its effect on the marking accuracy of a laser processing system, can be described as localized variation in working distance. Flatness induces error into

marking accuracy in the same manner described in Section 2.3.2, only the working distance is changing at each location on the powder surface being processed rather than layer to layer or build to build. As used here, "process flatness" is defined as the combined flatness of all components affecting the marking process. In the case of the laser fusion chamber, this simply refers to the flatness or surface profile of each layer of powder prior to fusion. Given that errors induced by changes in working distance are known to be a function of both location within the focal plane (through the output beam angle and f-theta relationship,) and the working height error at that given location, it is very difficult to predict the impact flatness will have over the field without a full map of the powder surface before each fusion. As a result, the errors predicted from process flatness below are calculated based on a worst case scenario, and considered a non-repeatability. Figure 2.10, below, illustrates how process flatness variably impacts marking accuracy.

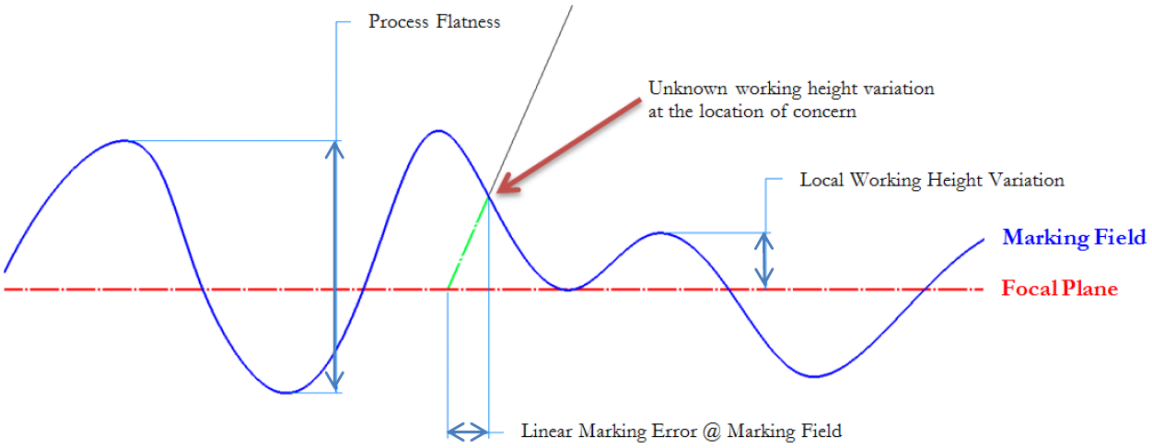

Figure 2.10: A simplified representation of flatness as localized height differentials, and the potential of induced laser spot placement error at the marking field.

Using Equation 2, above, the maximum potential error between subsequent locations in the marking field was approximated for various levels of process flatness given the

particular lens in use by the laser fusion chamber. The results are plotted in Figure 2.11, below.

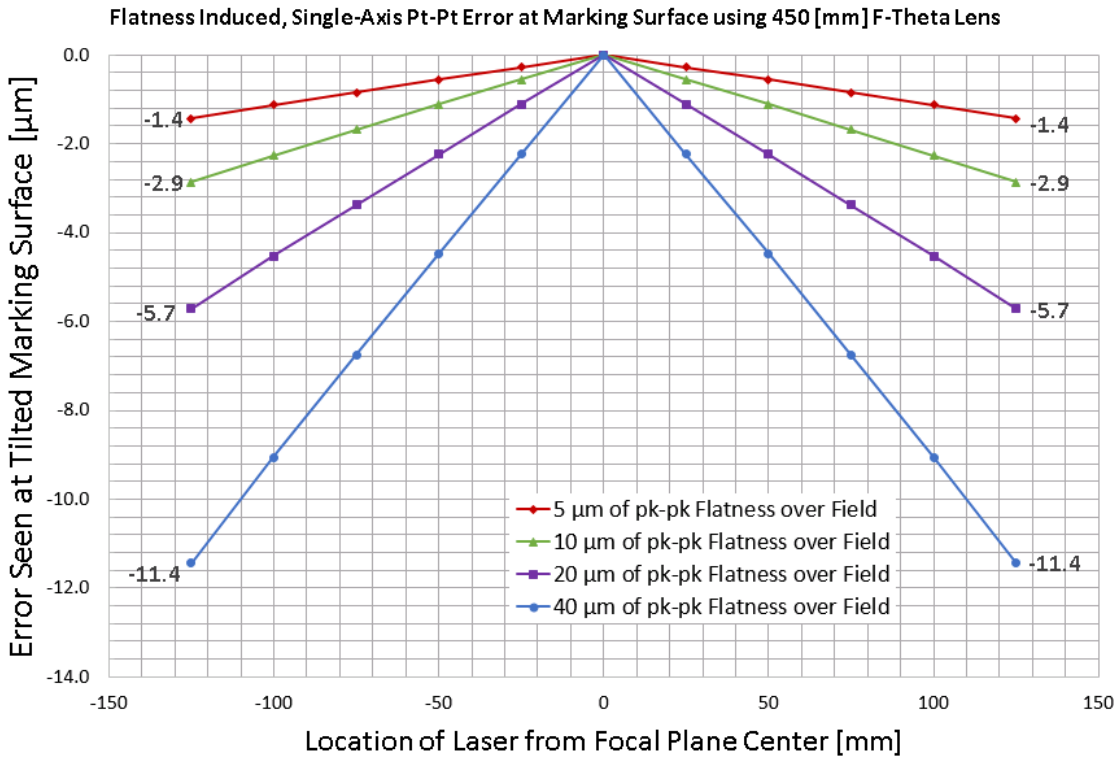

Figure 2.11: Theoretical approximation of maximum point to point error induction by process flatness for the laser scanner and f-theta lens combination employed in the EWI laser fusion chamber. (Error is defined as the difference between the magnitude of a uni-directional move seen in the marking field's coordinate frame, and the magnitude of the same uni-directional move as commanded in laser scanner coordinates. All deviations in marking height resulting from process flatness are assumed to be a reduction in height for simplicity.)

To reiterate, scanner systems, such as the one in use in this case, which involve large incident beam angles at the marking field are highly sensitive to height fluctuations. As stated before, only .001" [.025 mm] can produce non-negligible spot placement errors. This is of note because the nominal particle diameter in use in the chamber is .0015" [.040 mm]. Therefore, regardless of how perfect the powder recoating arm is able to spread the

powder, just the surface features caused by the granules themselves will influence laser spot placement accuracy.

2.3.4 Laser Alignment (Zero Offset Error)

The final error sensitivity of major concern in the employment of scanner units is that associated with laser alignment. The largest part of the marking error inherent in scanner systems is injected from the f-theta lens' distortion of the focal plane's coordinate frame, referred to as total theoretical lens distortion in Section 2.1.3. The exact manner in which this distortion is manifested over the focal plane depends on the boundaries of the laser beam's entrance into the lens. The lens' distortion of the beam's projected position on the focal plane is a function of the incoming beams distance from the axial center of the rear lens objective. The center point of the focal plane, or "zero" location of commanded moves, ideally corresponds with the laser beam passing coincident and parallel to the lens' axis. In this ideal condition, the theoretical lens distortion of the focal plane is axisymmetric about the lens' principle axis, which coincide with the (X) and (Y) axes of the focal plane, as defined by the laser spot's motion. Realistically, the beam incoming to the scan head is never perfectly aligned, and as a result, the laser beam being projected to the commanded center point of the focal plane is linearly offset from the axial center of the lens as it enters the rear objective. This is what is referred to herein as a "zero offset." Due to this zero offset, the actual lens distortion imparted on the focal plane is asymmetrical

As with all of the error sensitivities discussed within Section 2.3, as long as the alignment of the laser entering the scanner unit remains constant, whether there's a significant zero offset or not, the marking error induced by the lens' distortion of the focal plane can be corrected. However, any change in either the linear or angular alignment of

the input beam to the scan head will induce significant errors, in this case, at the focal plane itself (independent of the previously mentioned error sensitivities.) The level of this induced error is significantly more sensitive to angular changes in the alignment of the input beam. Angular changes in the input beam are projected through the scan head over a long enough distance that even a small change can create a substantial change in zero offset at the lens' rear objective.

The manner in which a change in the zero offset of a scanner system induces error is through the shift between the location of the f-theta lens and the incoming laser beam, and the associated shift in the focal plane's distortion. For example, when applying the manufacturer's provided correction table via a calibration file as previously mentioned, each value in the correction table is associated with a commanded position in the focal plane. However, the magnitude of each value is associated with where the laser beam passes through the lens relative to its axis when at its associated command position. Therefore, when a change in zero offset occurs, there is a relative shift between the commanded locations in the focal plane, and the location of the laser beam with respect to the lens. This shift destroys the validity of the connection between the magnitude of a correction in the table and the location it's associated with. As depicted in Figure 2.12, below, a zero offset shift from (X_0, Y_0) to (X'_0, Y'_0) changes every position of the laser beam throughout the focal plane the same amount relative to the lens' axis, thereby changing the magnitude by which the lens distorts each commanded position's global location on the focal plane. This relative shift between the focal plane and the lens' distortion map is depicted by the shift in (X_1, Y_1) to (X'_1, Y'_1) and (X_2, Y_2) to (X'_2, Y'_2). As a result of this shift, the correction counts intended to correct the lens' distortion at (X_1,

Y_1) over correct for the distortion that exists at (X'_1, Y'_1) because it is now closer to the lens' axis and is distorted a lesser amount. Likewise, the correction counts intended to correct the lens' distortion at (X_2, Y_2) are now not enough to fully correct the distortion seen by (X'_2, Y'_2) because it is farther from the lens' axis and is thereby further distorted. Therefore, the amount of error induced by a change in input beam alignment is dependent on the magnitude and type of the change, the size of beam path offset between laser mount and the scanner mirrors, and the slope of the manufacturer provided correction table being employed. The setup used in the laser powder bed fusion chamber has very large beam path offset between the laser collimator mounting fixture and the input aperture at the back of the f-theta lens. There are several redirecting optics used to steer the beam into the scan head, and it is therefore very susceptible to beam misalignment, likely rendering the manufacturer provided lens calibration invalid. The induced spot placement errors associated with this offset are discussed quantitatively in Section 2.5 and can be quite large.

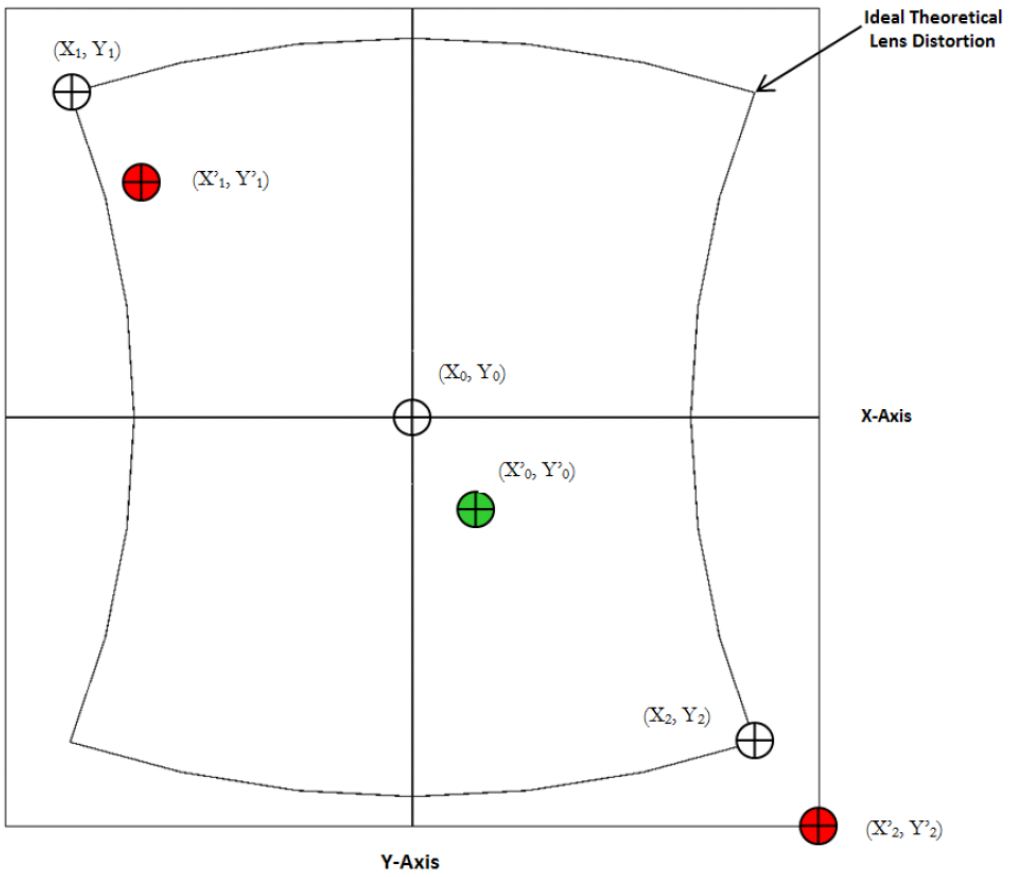

Figure 2.12: Depiction of a relative shift between commanded locations on the focal plane, and a map of the ideal distortion created by an f-theta lens, referred to as a change in zero offset.

Lastly, it should be reiterated that any additional distortion in laser beam placement at the focal plane coincides with additional power density distortion of the laser spot itself. As a zero offset changes the distortion imparted on the focal plane's coordinate frame, it coincidentally changes the spot size deviation throughout the plane of motion. If the laser parameters for the fusion process were selected assuming the manufacturer's specified beam diameter variation through the field of view, the user should be aware that the spot size deviation will be higher than calculated by optical software in some areas as a result of imperfect input beam alignment to the f-theta lens.

2.4 Substrate Viability & Mark Quality

In addition to the error sensitivities discussed in Section 2.3, the effectiveness of measuring the scanner's performance via a mark and measure technique is also largely dependent on the substrate being used, as well as the quality of marks being made on that substrate. As previously mentioned, the characterization of the laser spot placement employs the use of a microscope measuring machine. As such, the level to which the mark and measure procedure can characterize a scanner's performance is directly affected by the quality of the mark made by the laser system, and the microscope camera's ability to accurately measure each mark in the grid patterns being created. The marked substrate must produce a high level of contrast in the camera image; it must have exceptional surface finish to provide a solid background; lastly, the marks should be small and have crisp edges in order to produce the highly repeatable marking and measuring necessary for low uncertainty measurement via machine vision. These substrate features are demanded in addition to those geometric constraints required to minimize the induction of error as described in all of Section 2.3.

2.4.1 Measurement Repeatability & Marking Repeatability

Two major factors in the uncertainty of measuring marked substrates are the consistency with which the camera determines the center of a given mark, and the consistency with which the laser makes marks on the substrate of choice. The nomenclature coined to represent these two factors is "measurement repeatability" and "marking repeatability." Measurement repeatability is defined herein as the maximum peak to peak difference in the measurement of a mark's center between subsequent measurements of the same grid of marks. Conversely, marking repeatability is defined as

the maximum peak to peak difference in the measurement of subsequently marked grids, assuming an identical setup and marking field to focal plane relationship. As such, marking repeatability can never be exclusively determined because it is inherently inclusive of measurement repeatability and the aforementioned error sensitivities. It must be estimated using good statistical practices. An illustration of measurement and marking repeatability is provided in Figure 2.13, below. Combined, the measurement repeatability and marking repeatability establish the portion of measurement uncertainty associated with the machine vision determination of mark placement.

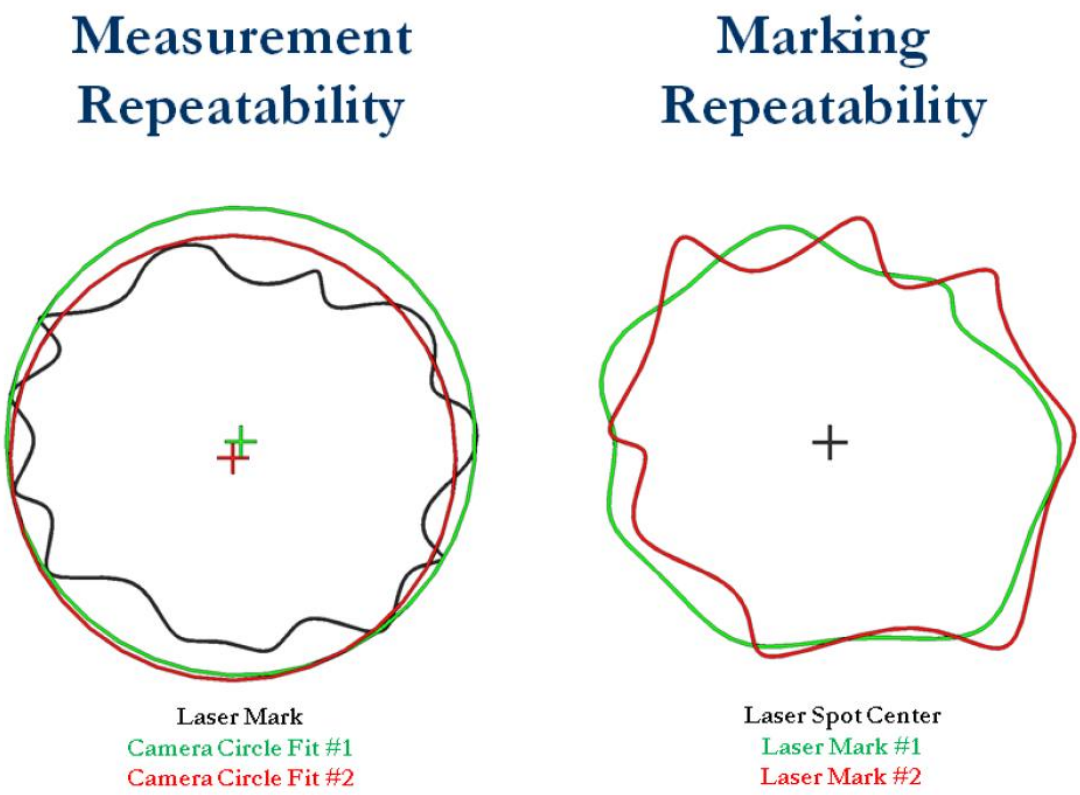

Figure 2.13: An illustration of measurement repeatability (left) and marking repeatability (right). The left shows the camera fitting two slightly different best fit circles to the same mark between subsequent measurements. The right shows two slightly different mark shapes made between subsequent markings created with the same relative laser spot center.

Through previous work, it was found that thin marks produce the best results in both measurement and marking repeatability. Thinner marks produce better results because they fundamentally do the least amount of damage to the substrate, and thereby impart the least amount of heat into the substrate. This causes very thin marks to have minimal heat affected areas and insignificant mark growth. Mark growth due to excess heat and/or a large heat affected area are major causes of mark randomness in addition to substrate surface consistency. Minimizing excess heat input is the key to increasing the repeatability of a mark's shape (marking repeatability.) Also, minimizing damage and heat input makes the contrast transition band between marked area and background very narrow in the camera image. The abrupt contrast change is what is described here as "crisp" marking. Having very crisp marks provides fewer inputs to the camera's edge search algorithms, reducing the total number of influences on its opinion of a mark's center. Limiting the amount of pixels involved in the camera's search algorithm, therefore, gives it fewer items to change its opinion over, and has shown to improve measurement repeatability substantially. As a result, the laser parameters used in the marking process should be adjusted until mark widths approach or become smaller than the anticipated laser spot diameter (the $1/e^2$ Gaussian value), or until the laser power is as low as can be consistently output as specified by the manufacturer. Unfortunately, the laser being used in the laser powder fusion chamber is of high output power, as a necessity for metal fusion. As a result, the minimum consistent continuous power output possible was nominally 50 watts. This proved to be in excess of what was required to make qualitatively high quality marks. The resulting measurement uncertainty, however, was still over an order of magnitude lower than the measured errors, as will be discussed below.

2.4.2 Making High Quality Laser Marks

The ability to make the small, crisp, high quality marks described above is dependent on two factors, substrate selection and the laser parameters used for marking. Both are important to achieving high quality marks, but the ideal laser marking parameters for making a high quality mark can differ from substrate to substrate.

As mentioned above, low uncertainty characterization via a mark-and-measure procedure using machine vision requires that the substrate have superb surface finish, produce crisp marks with good contrast, and be strictly dimensionally controlled. As such, it was found that glass substrates with optical quality thin film coatings make good substrate candidates. However, using a coated substrate requires certain considerations in the selection of laser parameters. When the laser has to drill through any thickness of coating to make a mark readable, it will impart more energy to the surface layer than is required to do damage as the beam drills through the coating's thickness. This naturally causes an increase in heat affected area and mark growth at the surface layer, which is the camera's image plane. Not only is the mark, therefore, inherently bigger than the laser spot, but also it inherits randomness in its size, edge, and overall shape. All three reduce the overall fidelity of the measurement (marking & measuring repeatability.) It is imperative to impart as little heat as possible to the area of surface layer surrounding the laser spot while fully burning or ablating the area underneath the spot to achieve high quality marks. An illustration of mark growth and an enlarged heat affected area produced by drilling through a coating is provided below in Figure 2.14.

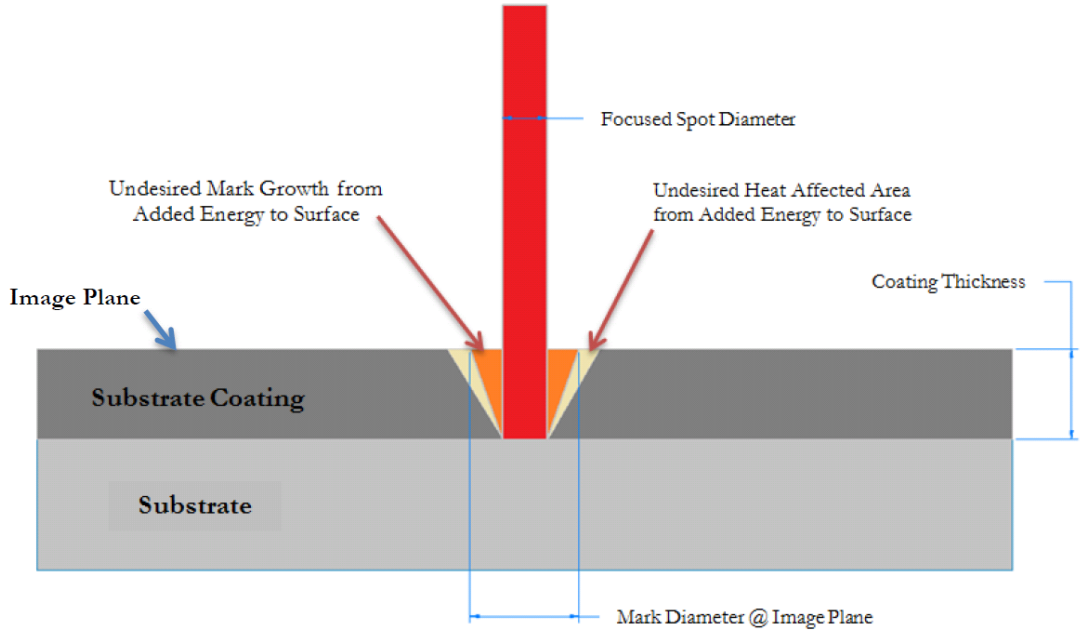

Figure 2.14: An illustration of mark growth at the image plane and induced heat affected area caused when drilling through a substrate's coating. As the mark grows at the image plane, its size and shape become less a function of the laser spot, and are more so dictated by the surface material's reaction to the thermal energy imparted to it. As a result, the heat affected area also widens, simultaneously decreasing the crispness of the enlarged mark. Both of these related thermal effects are practically random, and drastically reduce the calibration resolution for a grid of marks.

The thermal effects discussed above, mark growth and heat affected area, are not unique to marks made on coated substrates; they are only magnified by the coating. Low uncertainty measurement using the mark and measure technique, as previously stated, demands that these effects be minimized regardless of the materials and processes used for marking. This minimization is typically achieved through the selection of the laser marking parameters.

Typically, the operator of a laser marking system has control of certain explicit laser marking parameters, such as average output power or pulse energy, pulse width, the pitch and period between pulses, marking speed, etc. However, it is the implicit marking parameters that determine the overall quality of a mark, specifically average power density,

pulse power density, and average power seen by the substrate. The key to making high contrast marks that approach the theoretical laser spot size without producing the undesired thermal effects is to achieve high average and pulse power densities while reducing the average power dumped into the substrate. Unfortunately, the powder fusion chamber did not afford the ability to select much in terms of laser parameters apart from continuous laser output power. Since this parameter was only able to be minimized to 50 watts of continuous wave output, little could be done in terms of optimizing mark quality on the substrates. However, the general principle of high power densities and low average power input was adhered to as best as possible.

2.5 Machine Testing

2.5.1 Substrate Selection

As briefly discussed in Section 2.2, a mark and measure technique was used to characterize the laser spot placement accuracy of the scanner system within the laser fusion chamber. In order to minimize the influence of the error sensitivities discussed above, precision float glass slabs coated with a thin layer of evaporated silver were selected as the preferred marking substrate. There are several advantages to using such a substrate. First and foremost is the ability to achieve desirable dimensional characteristics at a relatively low cost. The substrates are of fairly uniform thickness with the surface flatness as well as the parallelism of the front and back surfaces being held to less than .0003" [.008 mm] over their full 6.0" [150 mm] square area. This minimizes the contributions of flatness induced errors in grid marking; their greatest potential influence at the margins of the available marking area are reduced to less than .0001" [.002 mm]. This tolerance would seem to eliminate the influence the of parallelism induced errors as well, however, due to the

building process this becomes difficult. Since the marking substrate will lie on the build platform during machine characterization, the upper surface of the substrate does not reflect the planar sweep of the powder recoating arm. During an actual build, the marking field (upper powder surface) location is dictated by the motion of the arm rather than the plane of the build platform's surface. Therefore, it is difficult to accurately place and level the marking substrate such that its upper surface is parallel and coincident with the sweep of the recoating arm. As a result, the level of parallelism induced error into the machine characterization is difficult to know, and the results do not necessarily exactly reflect the motion of the laser spot on any future powder surface. Additional beneficial characteristics of the silver coated glass slabs are the minimal thickness and low damage threshold of the silver coating that has been applied. These features help maximize the quality of laser marks as they pertain to the issues discussed in Section 2.4 and minimizing measurement uncertainty.

The goal of minimizing the influences of the error sensitivities discussed above through substrate selection is to solely capture the beam placement errors induced by the f-theta lens distortion and systematic mirror motion errors. If these influences are characterized to a low uncertainty, they can be readily corrected as they remain static through the life of the scanner. As a result, the influences of the error sensitivities discussed can be regarded as non-repeatabilities in the setup and operation of the machine. Knowing the capabilities of the scanner assembly in an idealized scenario gives insight into process influences on accuracy when those capabilities are not reached.

2.5.2 Testing Procedure

Prior to marking grids, the build platform was aligned to the sweep of the powder recoating arm by the operator via a three point tip tilt screw adjustment built into the platform's mounting. The operator used qualitative judgment of the uniformity of a subsequent single layers of distributed powder in order to determine the proper alignment of the platform. No quantitative measurements of parallelism were carried out. Once the platform was aligned to the recoating arm, the chamber was cleared of powder and thoroughly cleaned. Substrates were then introduced into the chamber to capture marking operations. Each substrate's thickness was individually measured with a micrometer to adjust the build platform height appropriately. The upper surface of each substrate was nominally located at the marking field (vertical position where recoating arm hypothetically lays the powder surface). Rough alignment of each substrate to the axes of laser motion was carried out with the red laser diode incorporated into the laser system to ensure that each grid would fit on the available marking area.

After a substrate was placed on the build platform and aligned, a grid of laser marks was made on each, as stated above. Each grid consisted of 121 marks in an 11 by 11 equally spaced array. Grid marks consisted of single laser pulses of 50 watts, for a duration of 1 millisecond, providing a single circular mark of 200 μm diameter at each grid location. With a pitch of 10 millimeters, each grid encompassed a 100 by 100 millimeter area. This grid size was selected due to the range limitation of the Nikon microscope measuring machine being used to characterize the relative mark locations within each grid. Therefore, substrates had to be marked in various locations on the build platform in order to fully characterize spot placement accuracy over the full 250 millimeter square field of view of

the scanner. A single substrate was marked in each quadrant of the scanner's field of view, with the appropriate corner of each grid collocated with the scanner's zero location. This arrangement of grid patterns allows for a characterization of the scanner's full field of view. Figure 2.15 below, is a schematic of the covered scanner field of view by the 5 subsequently marked grids described above.

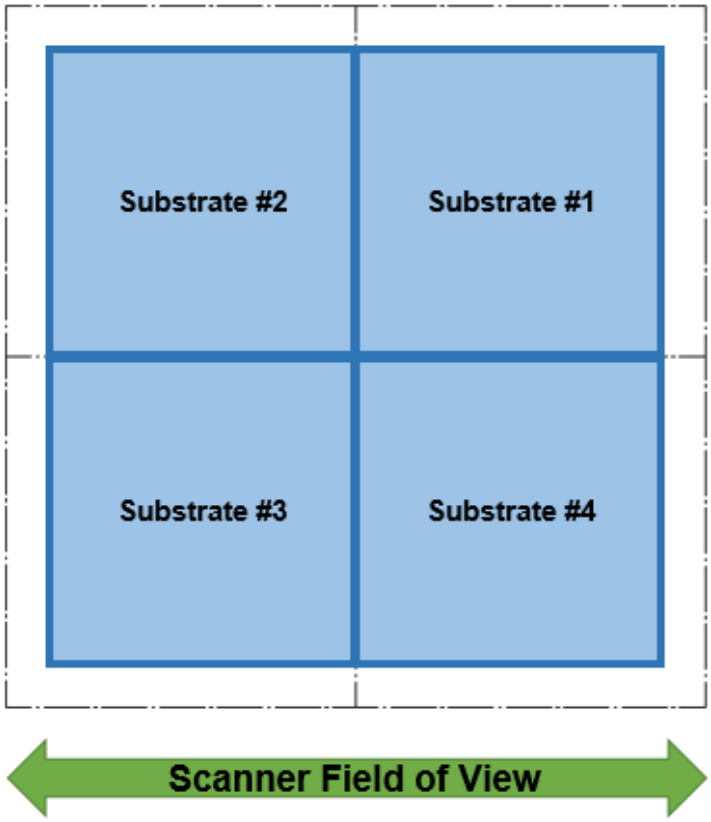

Figure 2.15: Schematic showing the field of view tested when marking the first four coated glass substrates during machine testing. Each quadrant was used to mark a 100 square millimeter grid pattern with overlap at the origin.

In addition to characterizing the full field of view of the scanner, a more focused characterization was carried out of the specific build area being used by the operators at EWI. Four substrates were marked in the same manner as above, but the grids encompassed the 100 by 100 millimeter area currently being used to build parts. This area

is outlined by the four corners (5, -25), (105, -25), (5, 75), and (105, 75) [mm] in scanner coordinates and a schematic showing its relative position to the scanner's full field of view is shown below in Figure 2.16. Each of the four substrates were marked in the same fashion, in as rapid succession as accurately feasible. The repeated marking of grids in the build area is necessary to capture the statistical deviations in laser spot placement caused by the fore mentioned marking and measuring repeatability needed to perform a full measurement uncertainty analysis.

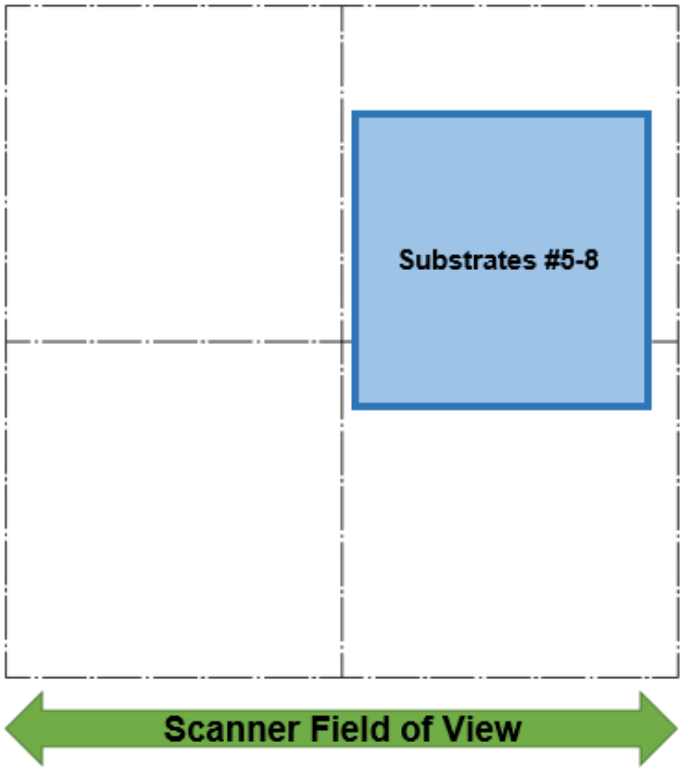

Figure 2.16: Schematic showing the field of view tested when marking the fifth through the eighth coated glass substrates during machine testing. Multiple substrates were captured over the same field of view of statistical analysis of marking and measuring repeatability.

2.5.3 Results

Below are the results of the eight substrates marked and measured as described above. Each grid measurement is presented as a series of surface plots representing laser spot

placement error as a function of position within each grid respectively, plus a raw two dimensional plot of the grids themselves with no alterations. The first two surface plots for each grid show X and Y axis laser spot placement error respectively as a function of grid position. Error is defined as the difference between the each laser spot's measured position and its nominal position, relative to the center mark of the grid. The third surface plot is the vector sum of the X and Y axis laser spot placement error in each grid, showing the radial placement error of each mark from its nominal position as a function of location within the grid. The results of grid measurements covering the build area are the average of the four marked substrates covering that location in the scanner field of view (FOV).

2.5.3.1 Quadrant One Scanner Accuracy

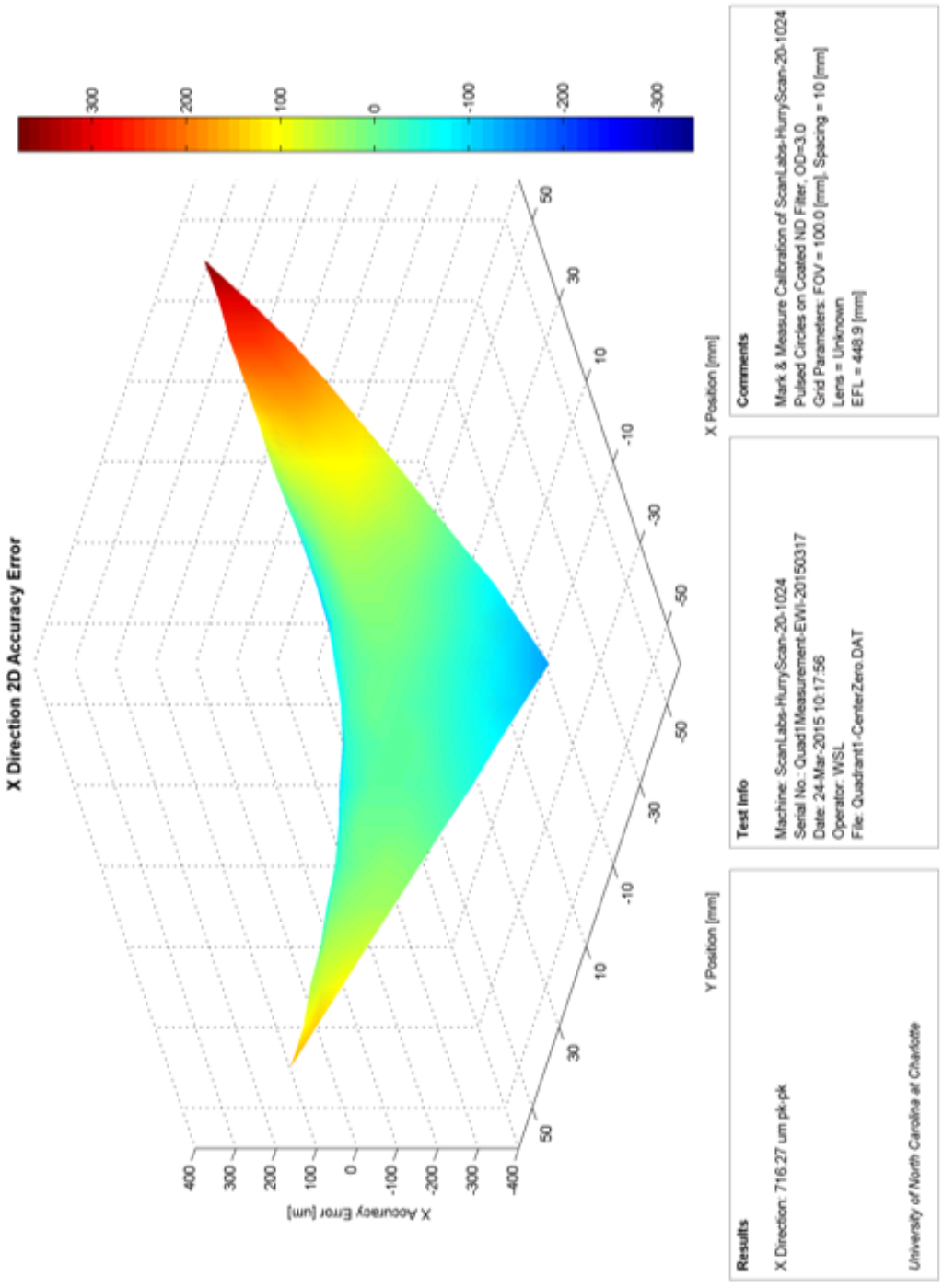

Figure 2.17: Map of laser spot placement error for the X-axis over the first quadrant of the scanner's field of view.

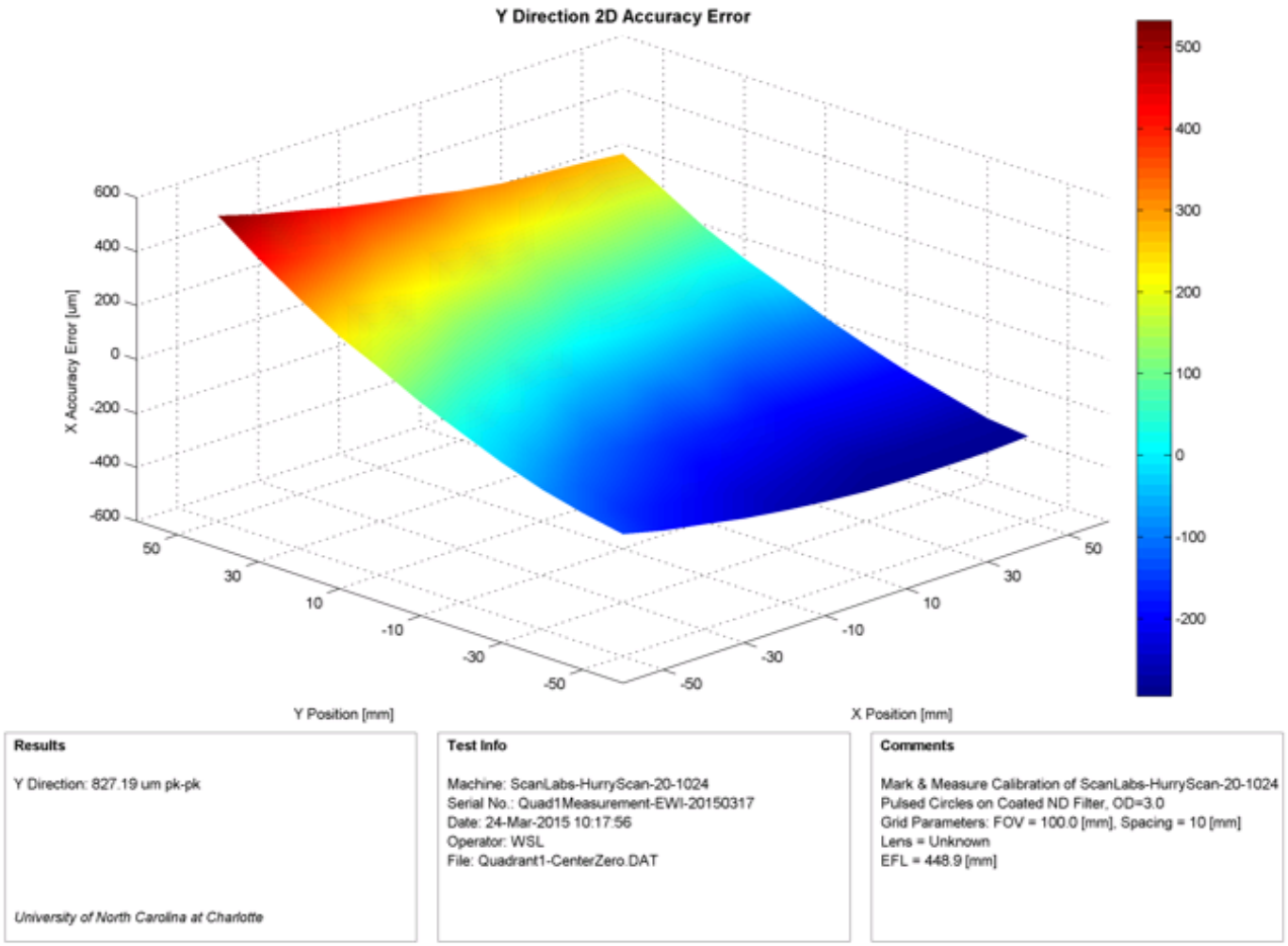

Figure 2.18: Map of laser spot placement error for the Y-axis over the first quadrant of the scanner's field of view.

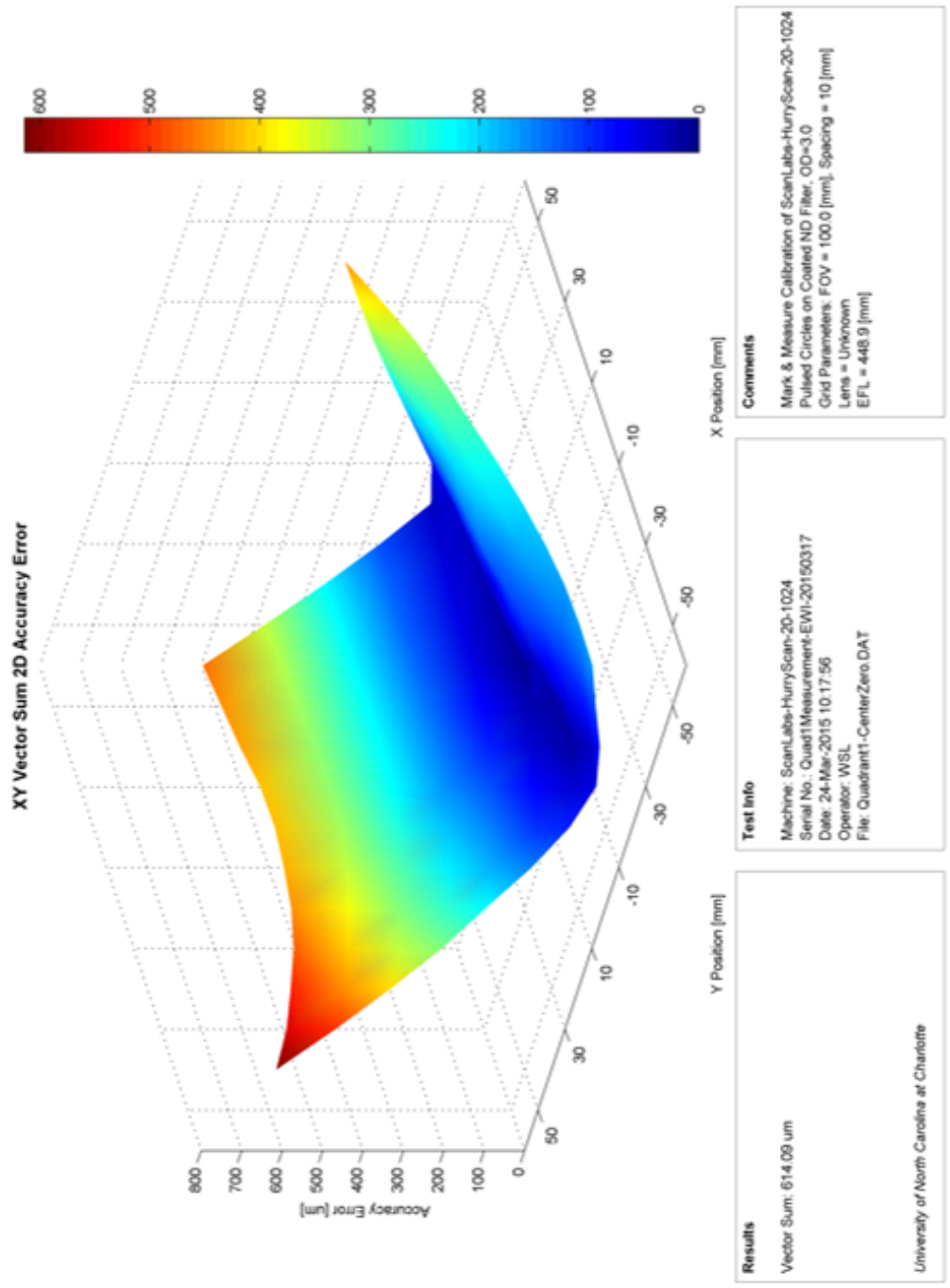

Figure 2.19: Map of the vector sum of laser spot placement error over the first quadrant of the scanner's field of view.

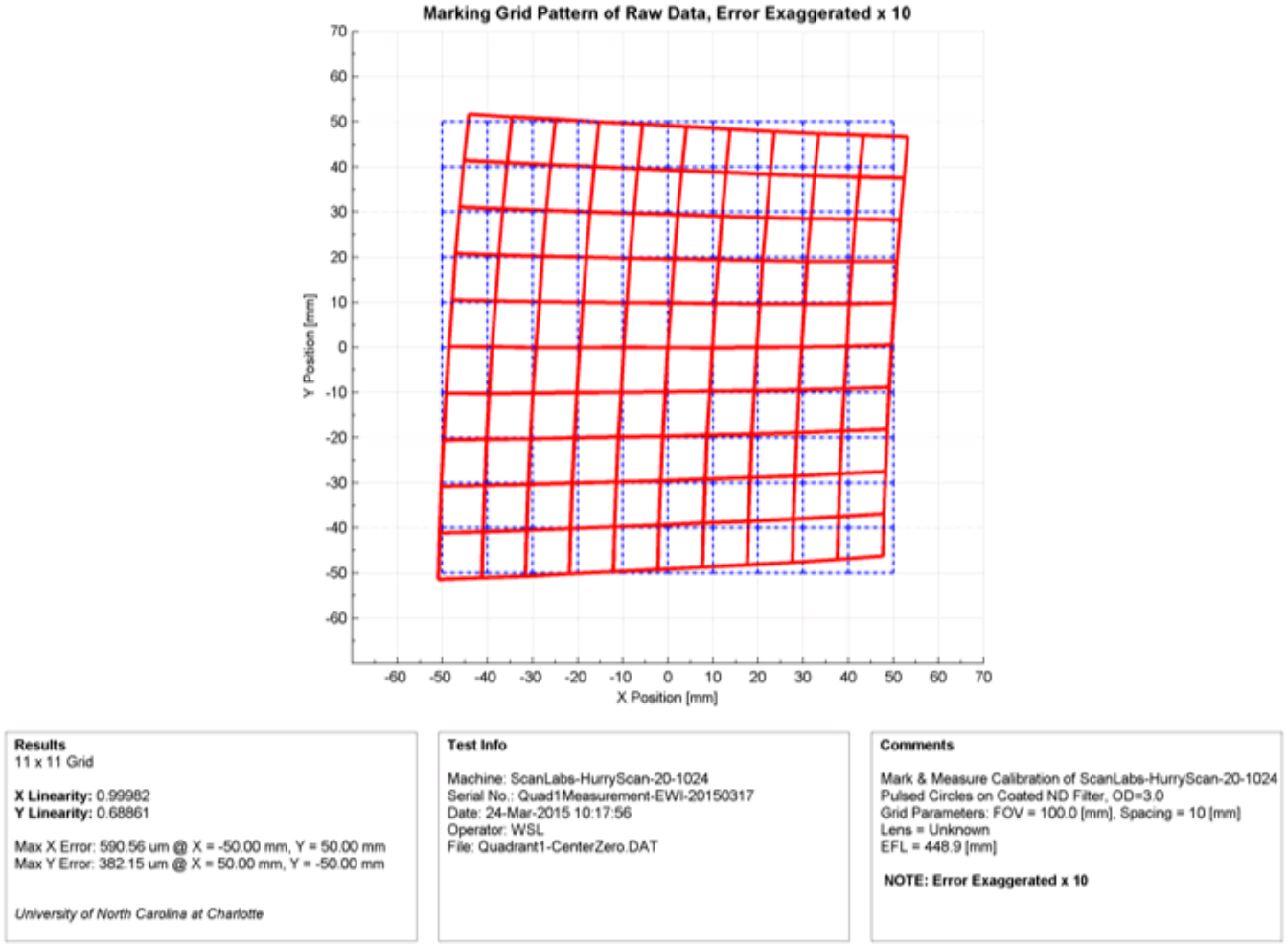

Figure 2.20: Grid plot of measured mark position in the first quadrant relative to nominal with errors exaggerated tenfold.

2.5.3.2 Quadrant Two Scanner Accuracy

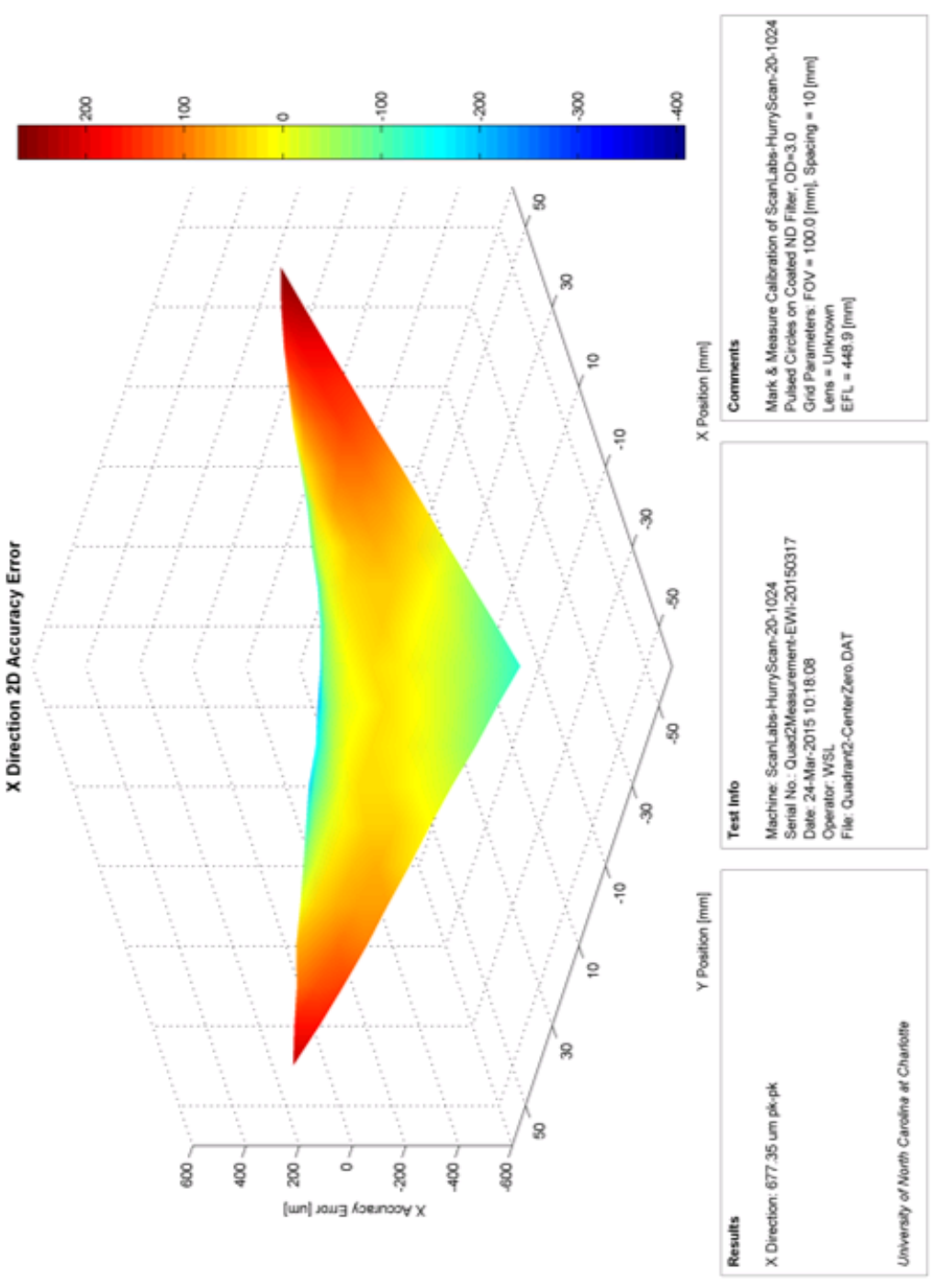

Figure 2.21: Map of laser spot placement error for the X-axis over the second quadrant of the scanner's field of view.

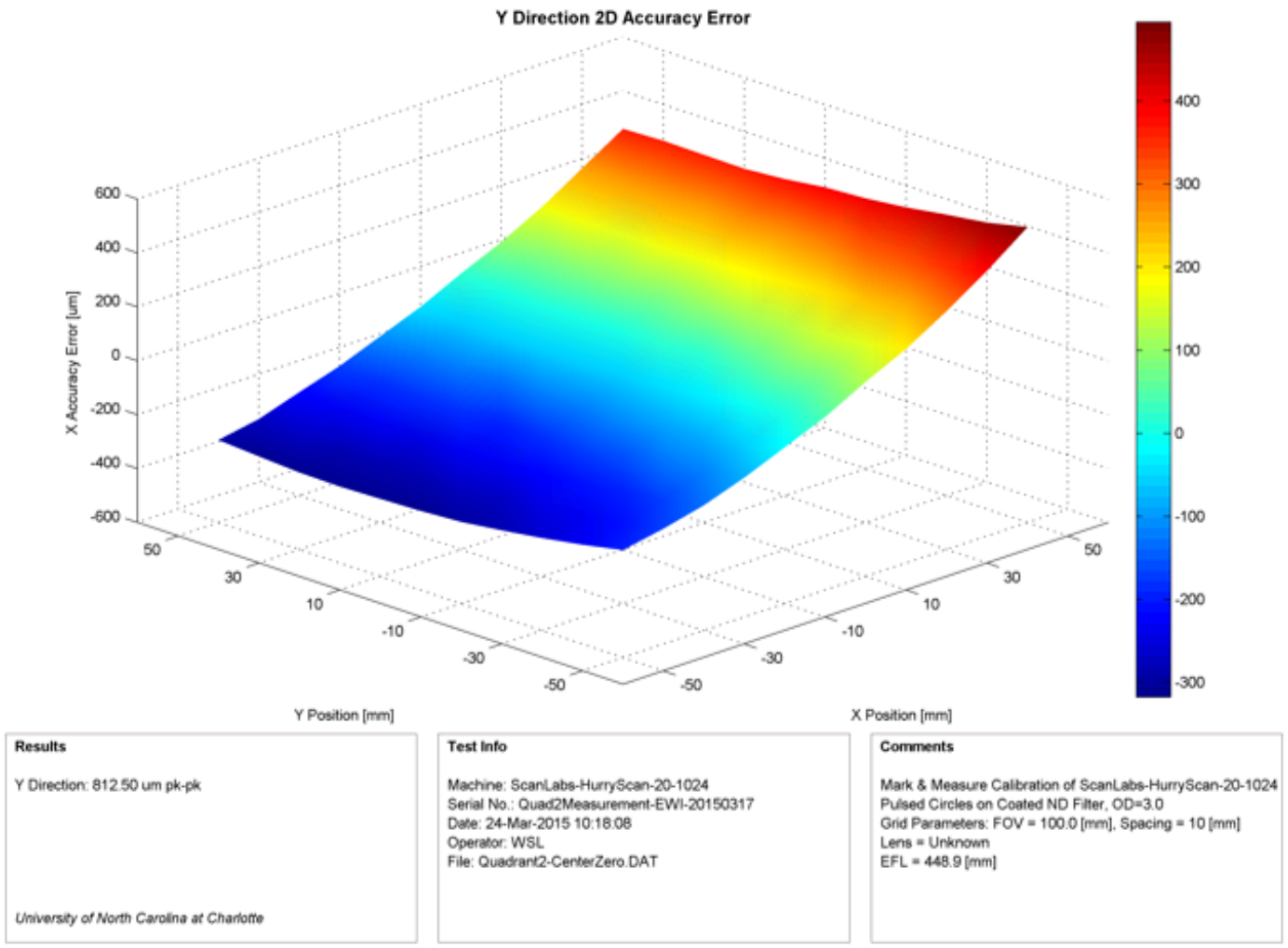

Figure 2.22: Map of laser spot placement error for the Y-axis over the second quadrant of the scanner's field of view.

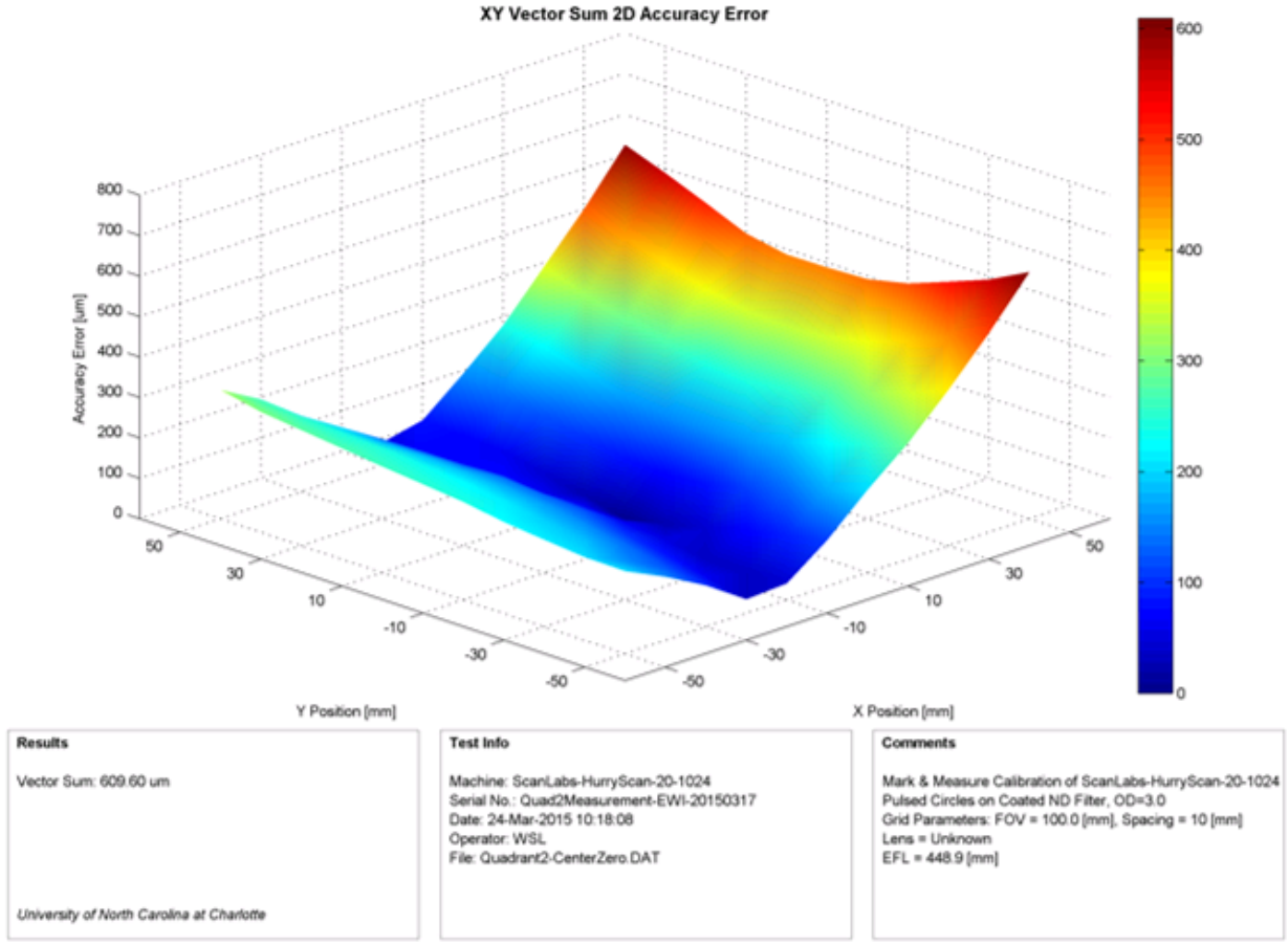

Figure 2.23: Map of the vector sum of laser spot placement error over the second quadrant of the scanner's field of view.

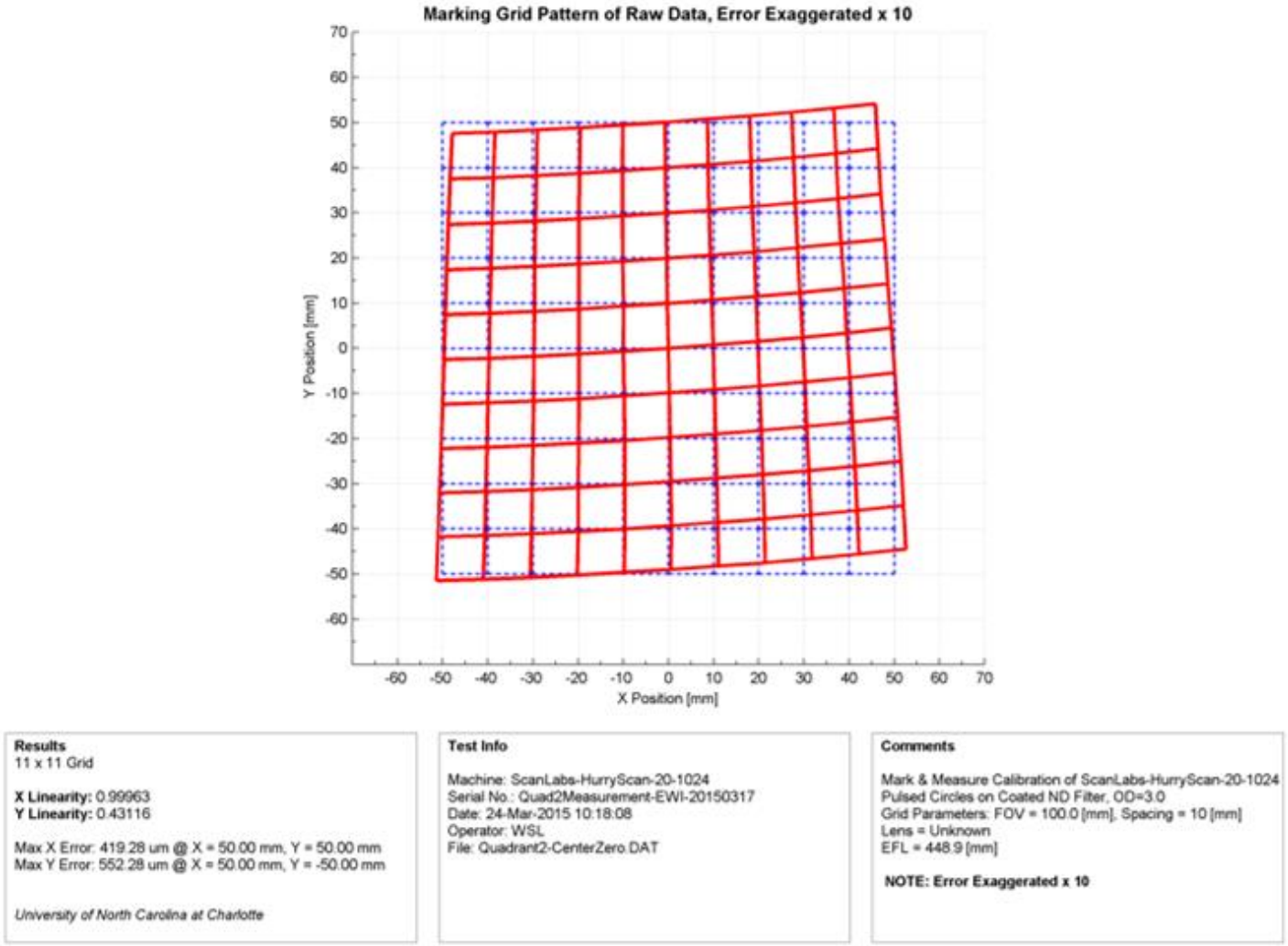

Figure 2.24: Grid plot of measured mark position in the second quadrant relative to nominal with errors exaggerated tenfold.

2.5.3.3 Quadrant Three Scanner Accuracy

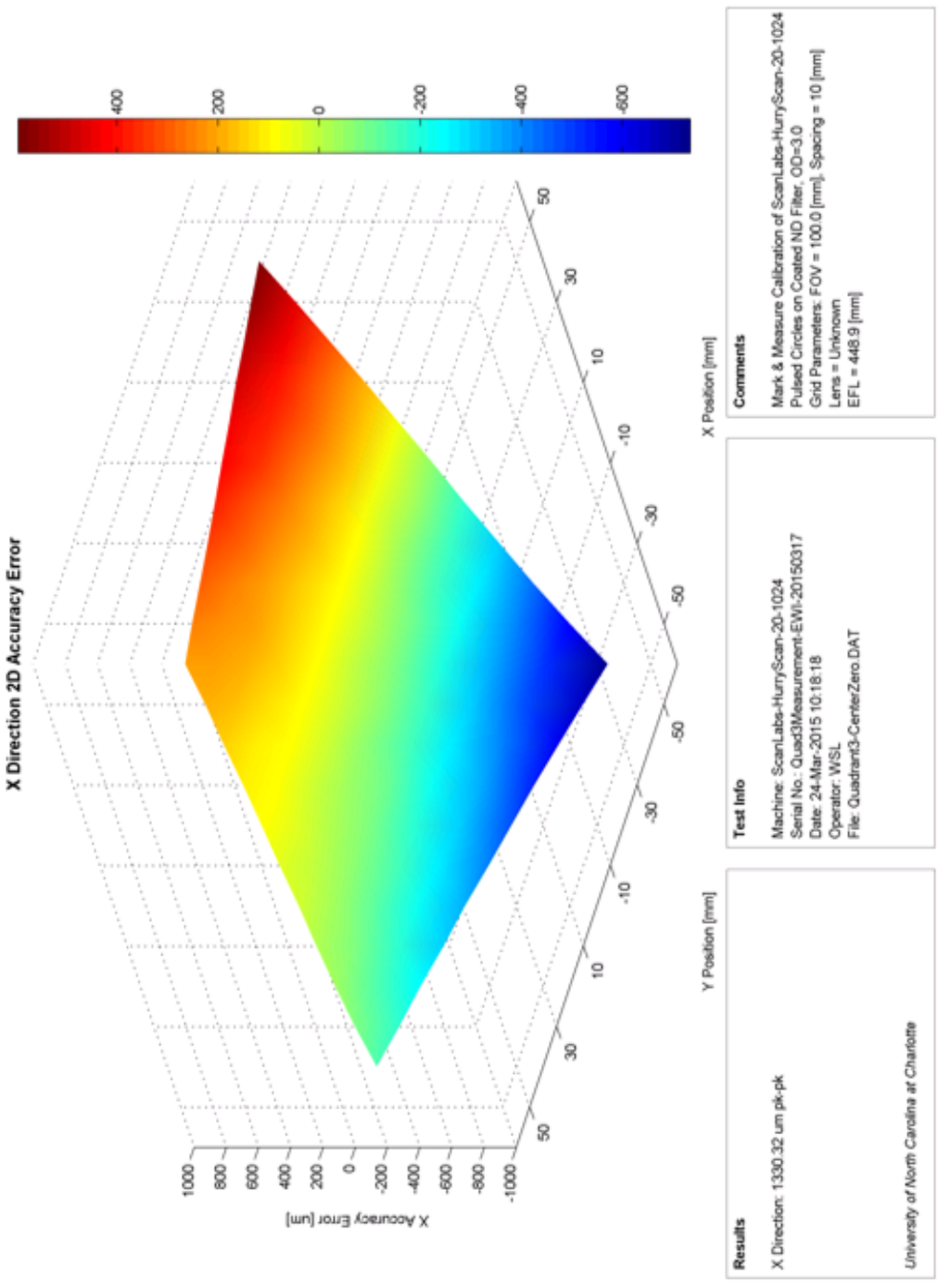

Figure 2.25: Map of laser spot placement error for the X-axis over the third quadrant of the scanner's field of view.

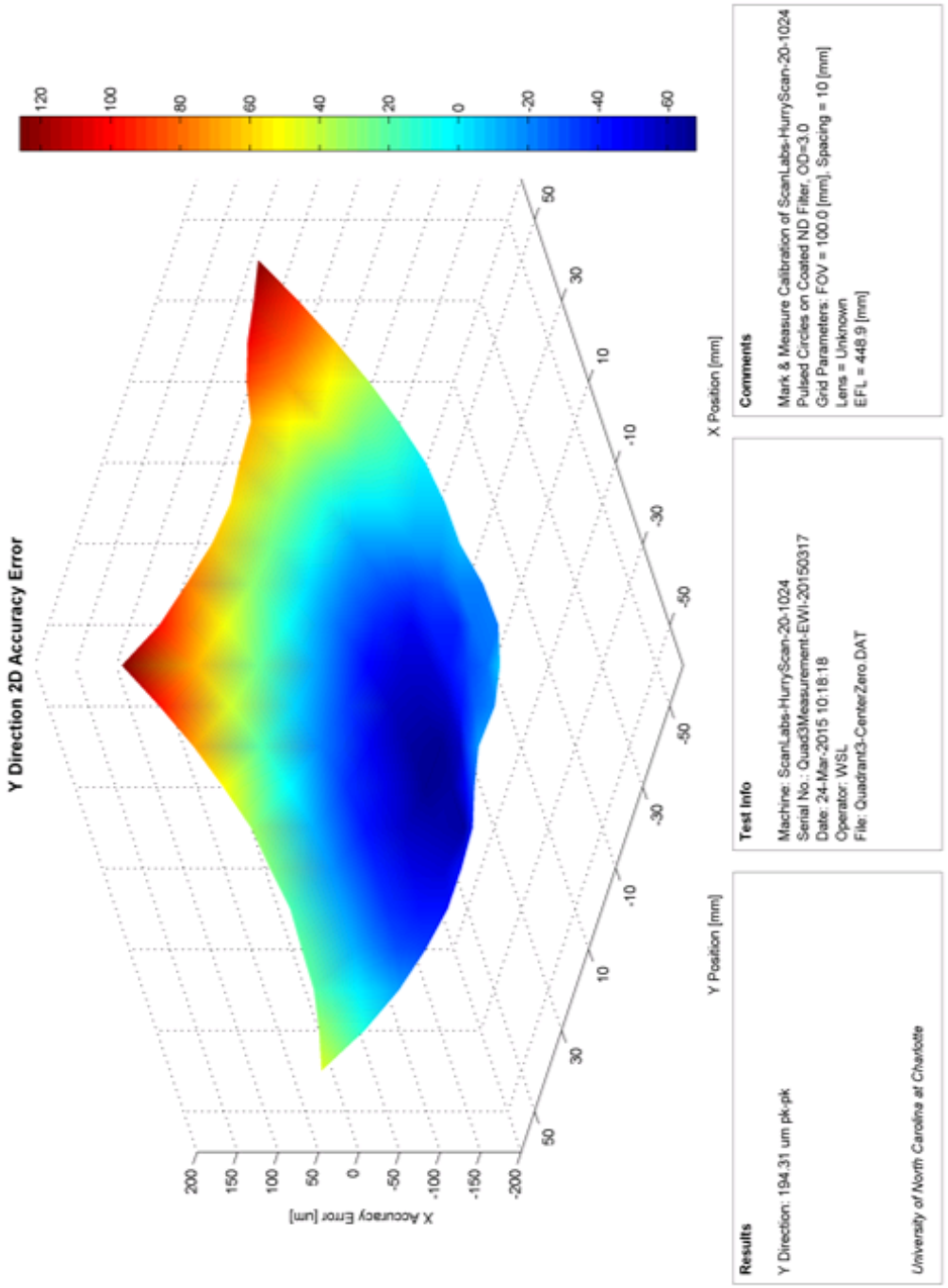

Figure 2.26: Map of laser spot placement error for the Y-axis over the third quadrant of the scanner's field of view.

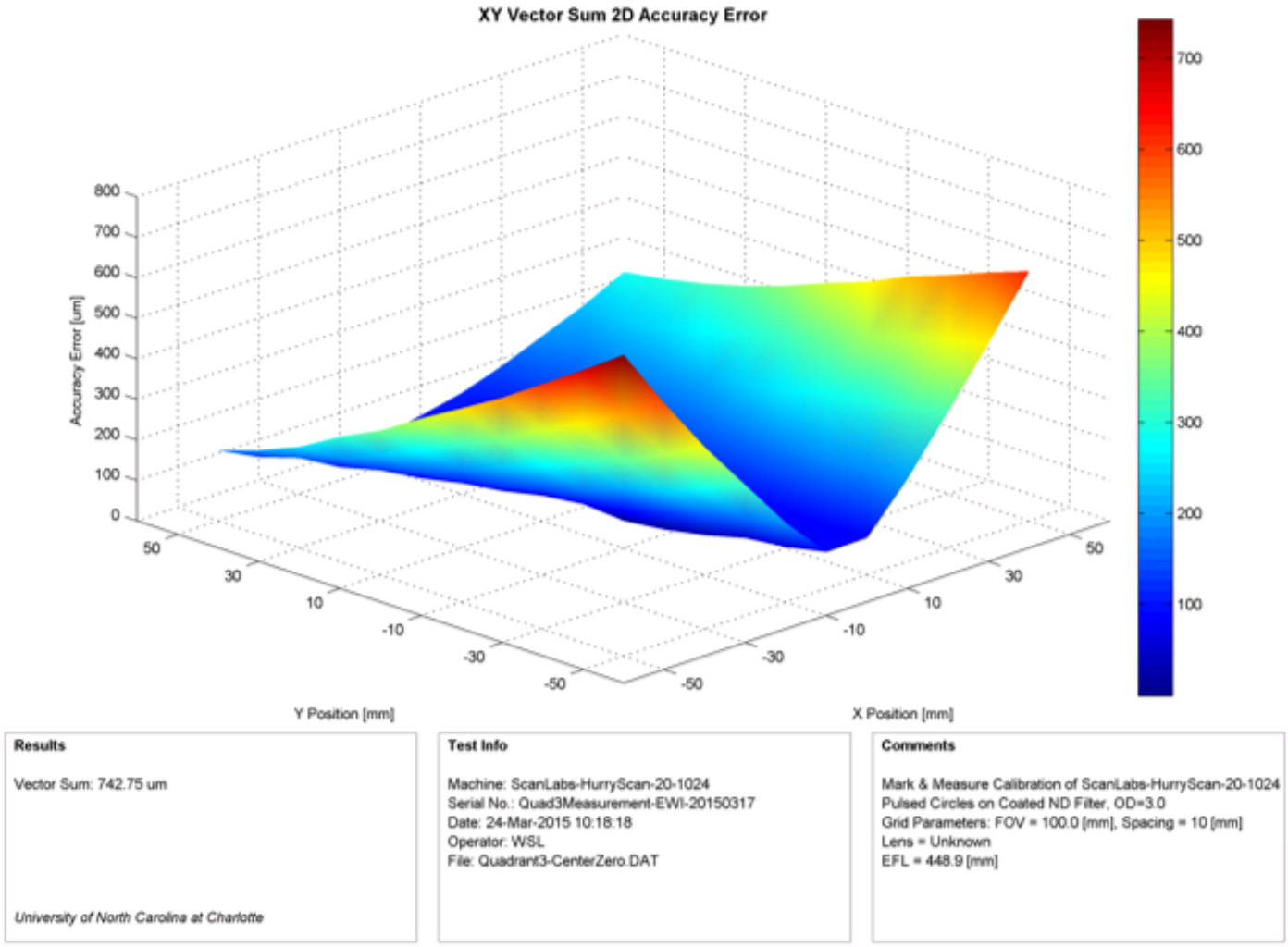

Figure 2.27: Map of the vector sum of laser spot placement error over the third quadrant of the scanner's field of view.

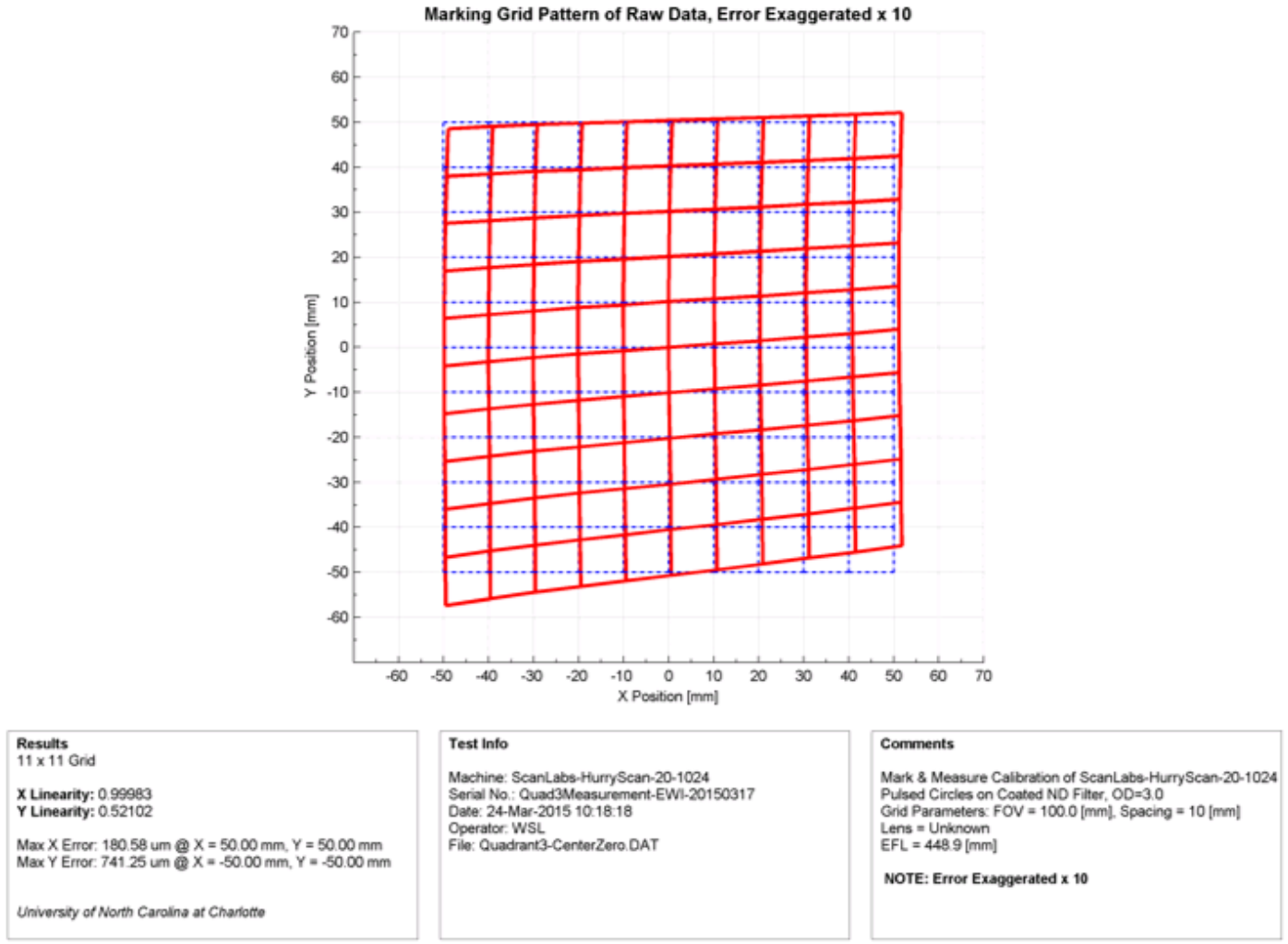

Figure 2.28: Grid plot of measured mark position in the third quadrant relative to nominal with errors exaggerated tenfold.

2.5.3.4 Quadrant Four Scanner Accuracy

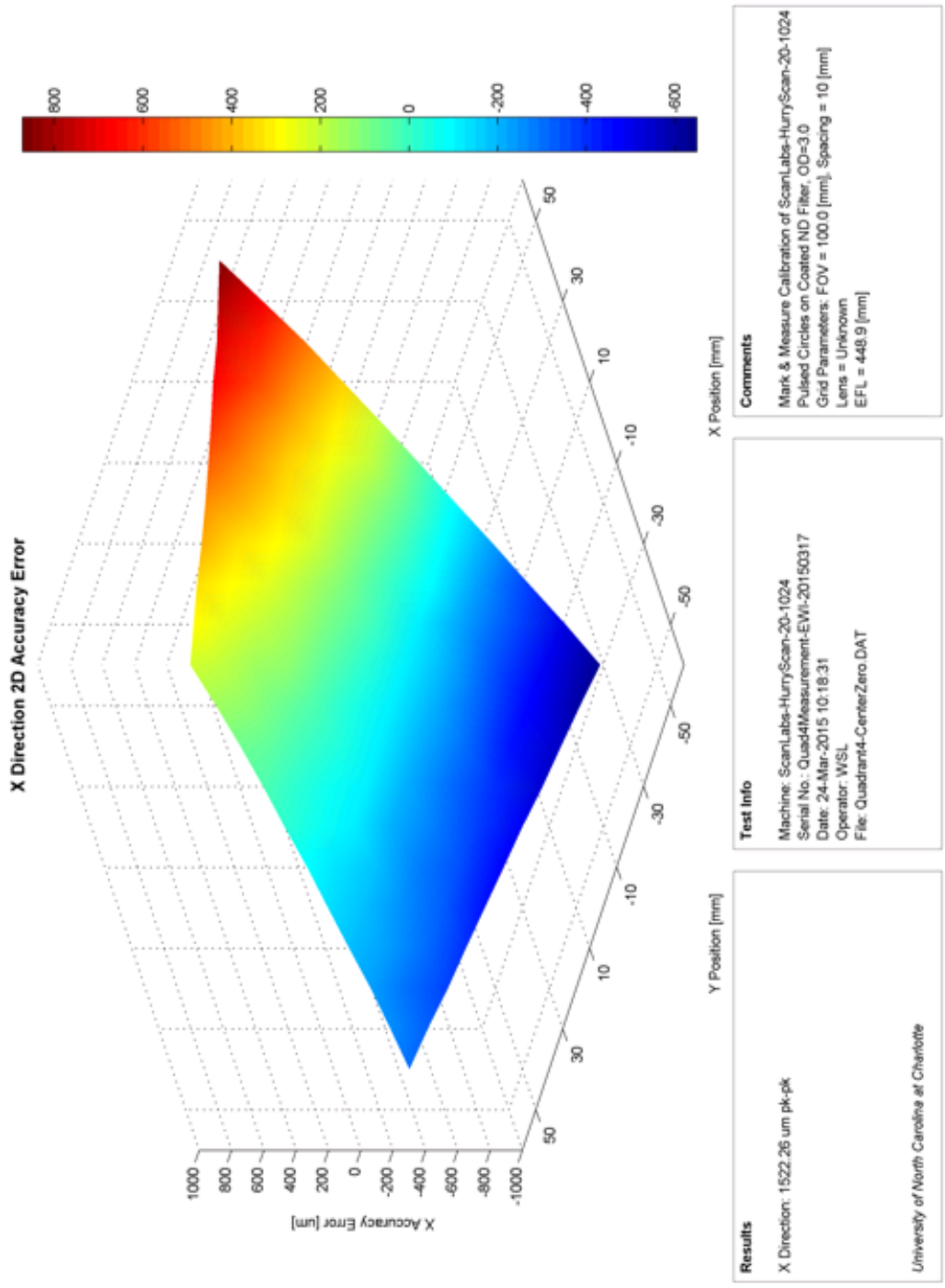

Figure 2.29: Map of laser spot placement error for the X-axis over the fourth quadrant of the scanner's field of view.

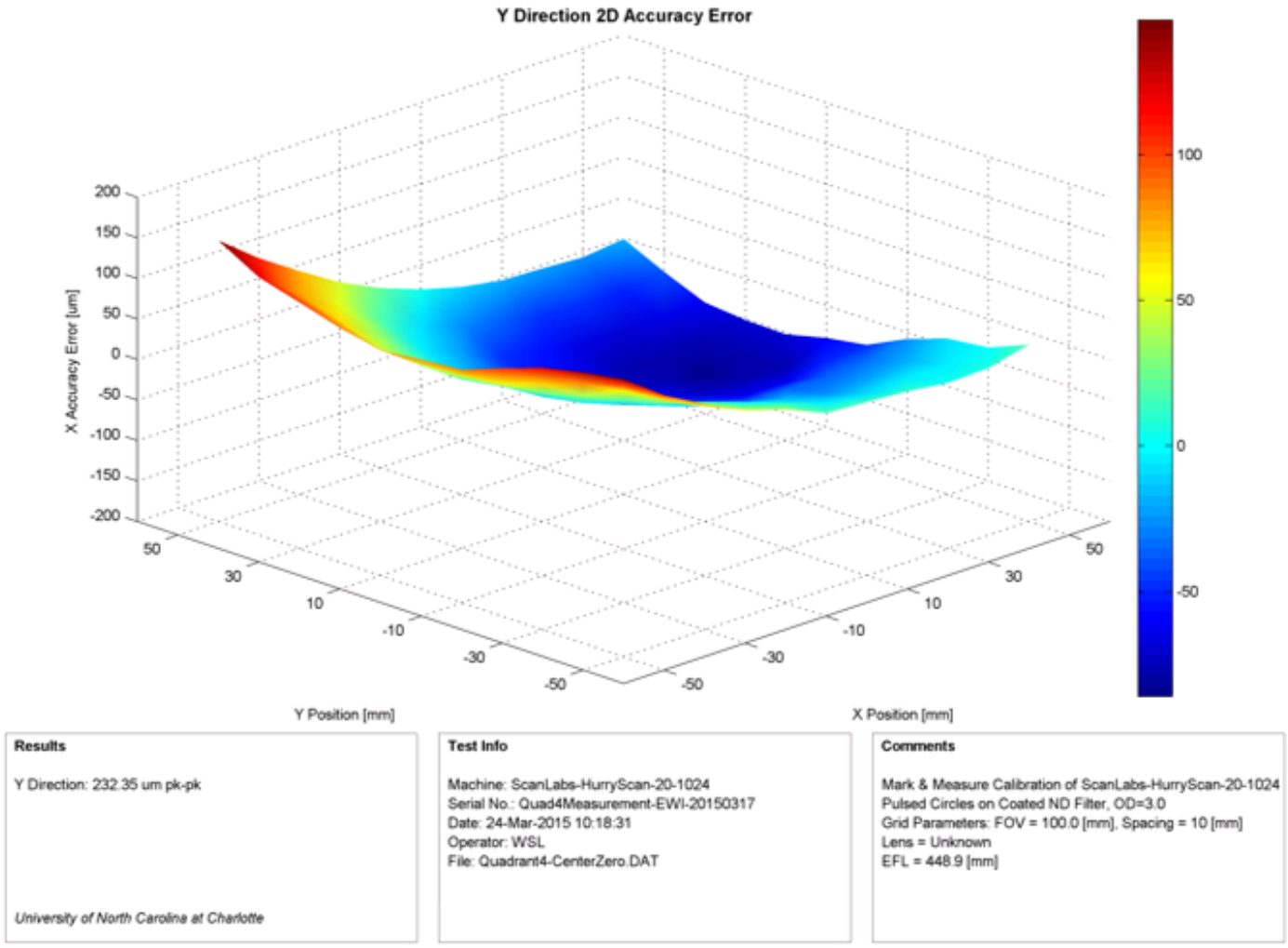

Figure 2.30: Map of laser spot placement error for the Y-axis over the fourth quadrant of the scanner's field of view.

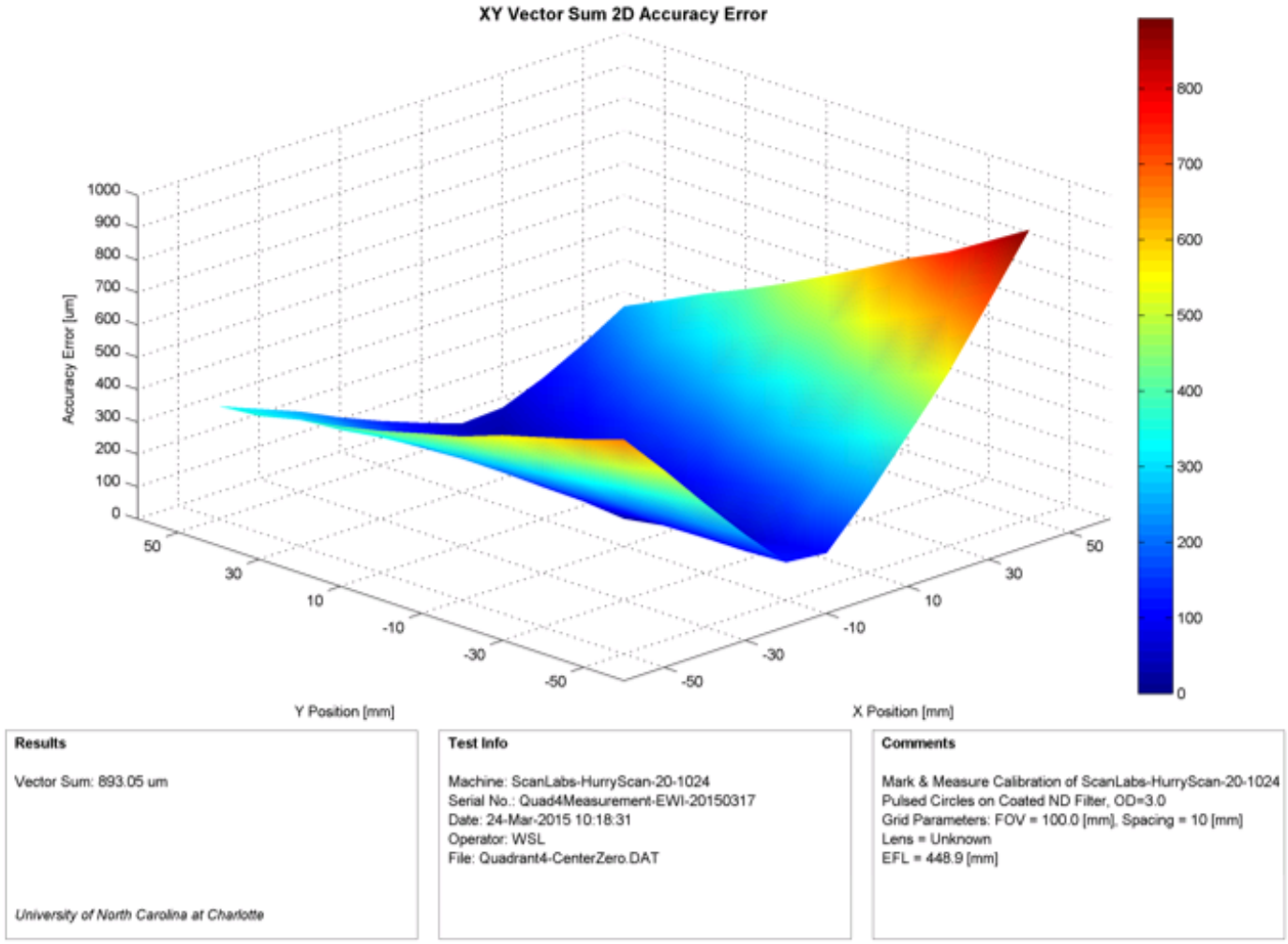

Figure 2.31: Map of the vector sum of laser spot placement error over the fourth quadrant of the scanner's field of view.

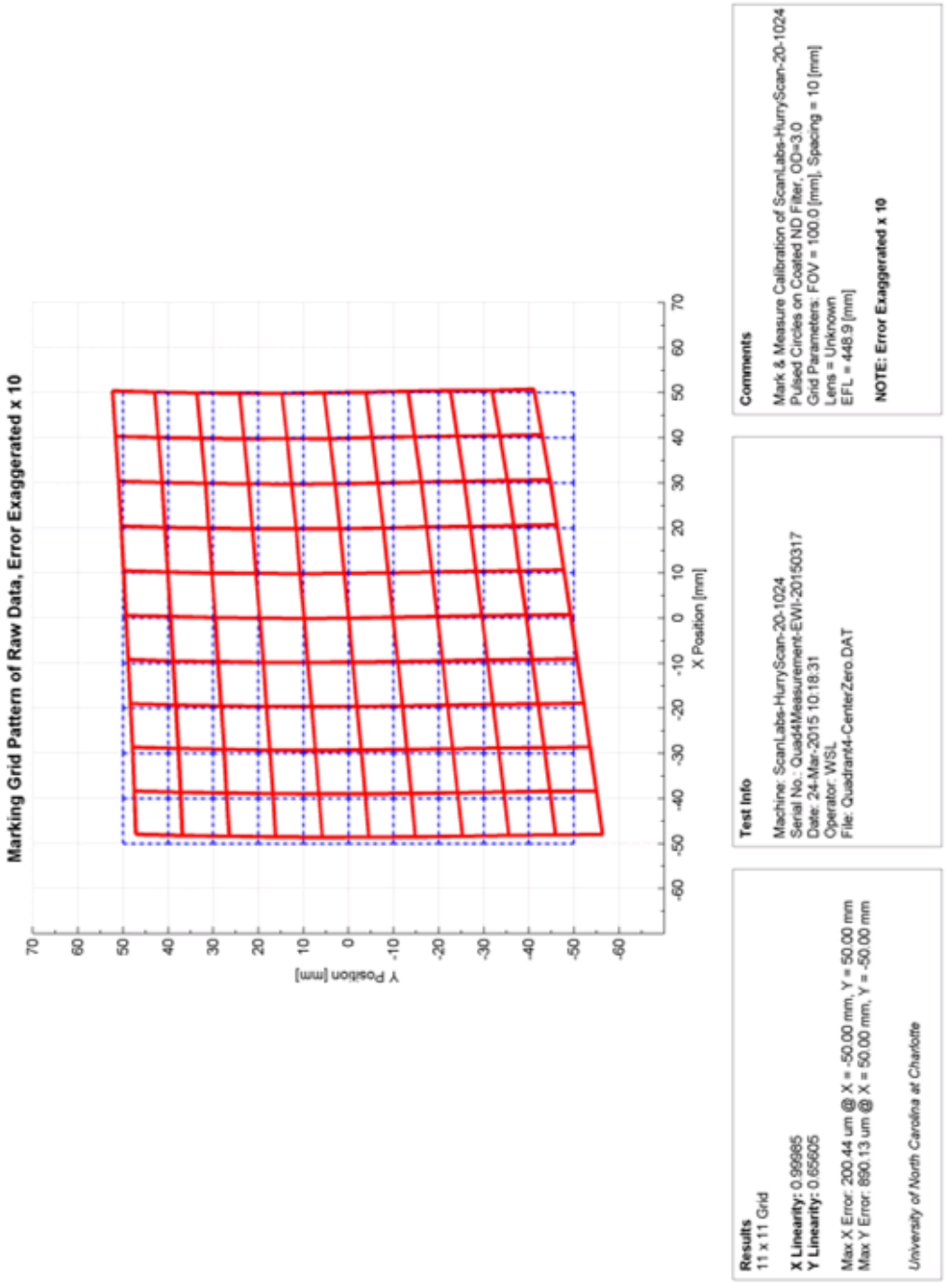

Figure 2.32: Grid plot of measured mark position in the fourth quadrant relative to nominal with errors exaggerated tenfold.

2.5.3.5 Average Measured Build Area Scanner Accuracy

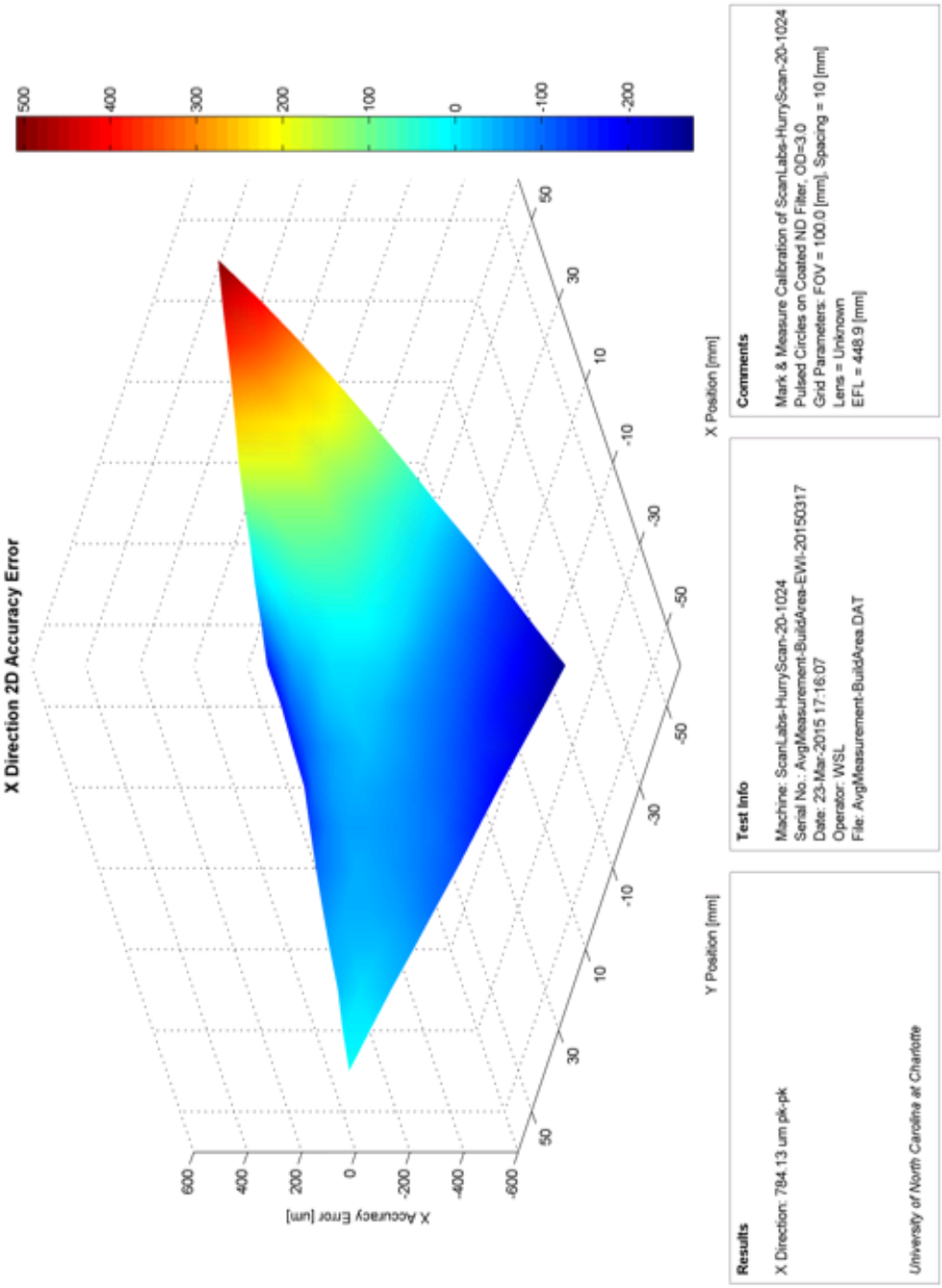

Figure 2.33: Map of average laser spot placement error for the X-axis over the portion of the scanner's field of view being used during build.

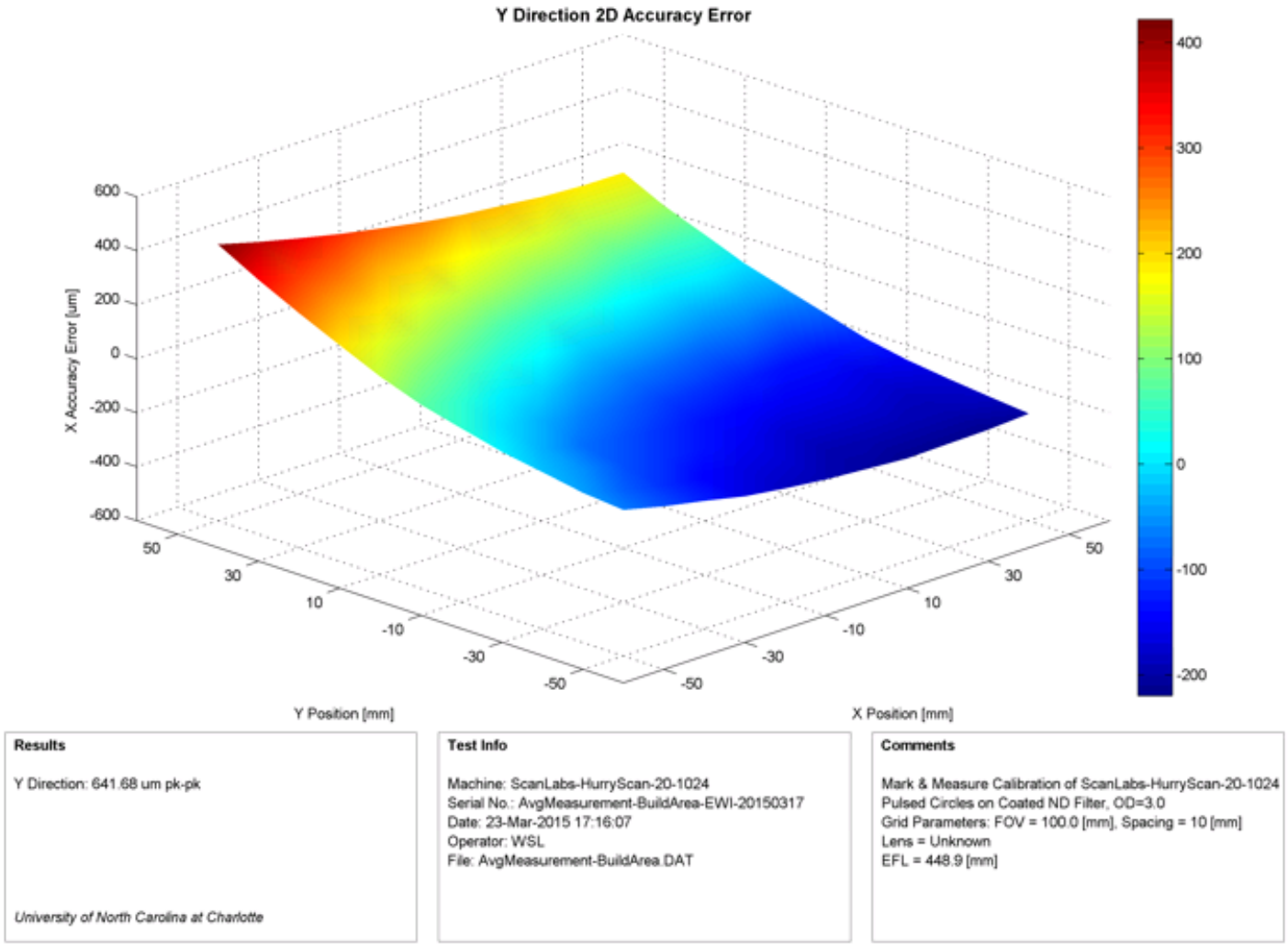

Figure 2.34: Map of average laser spot placement error for the Y-axis over the portion of the scanner's field of view being used during build.

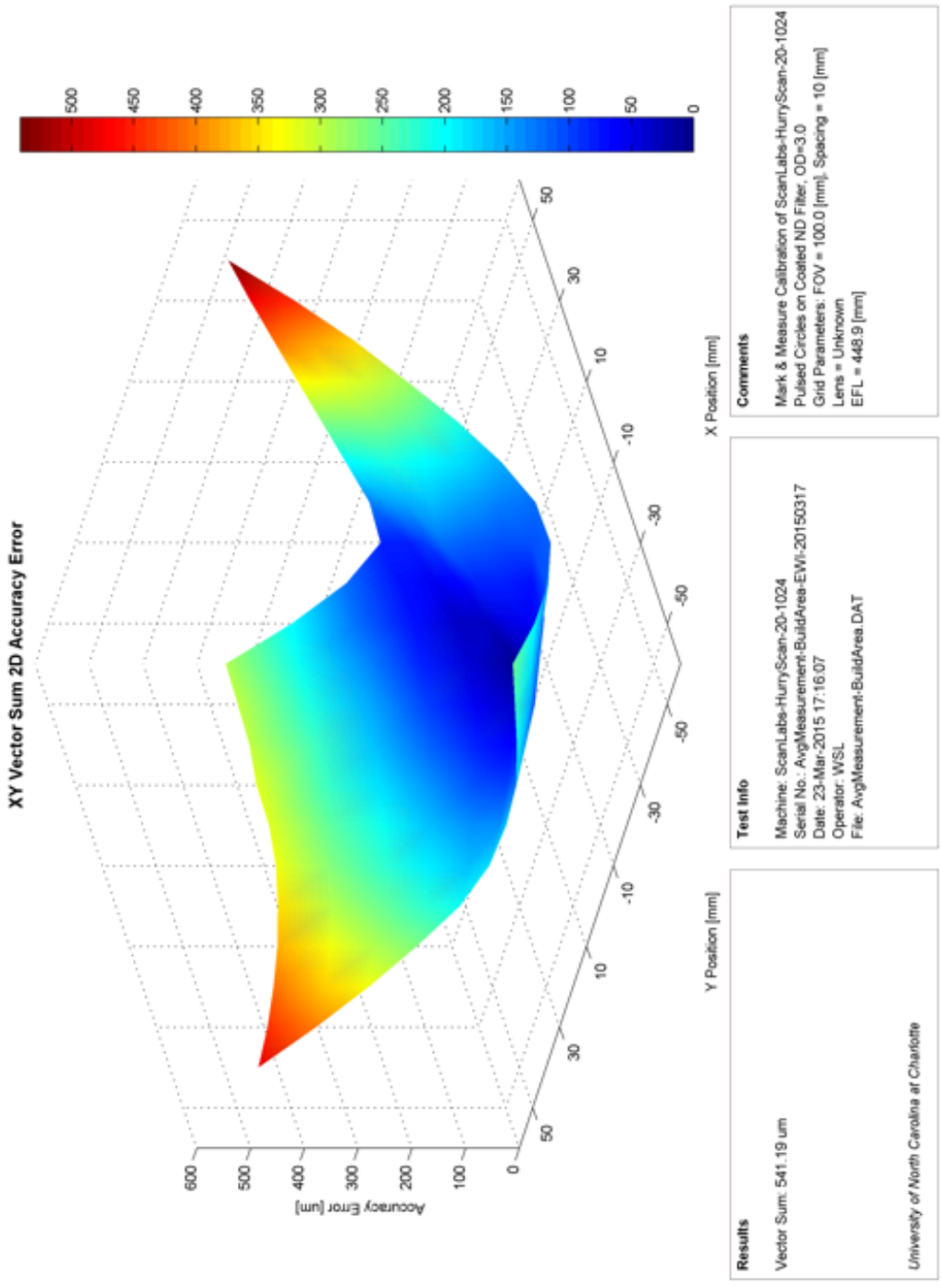

Figure 2.35: Map of average vector sum of laser spot placement error over the portion of the scanner's field of view being used during build.

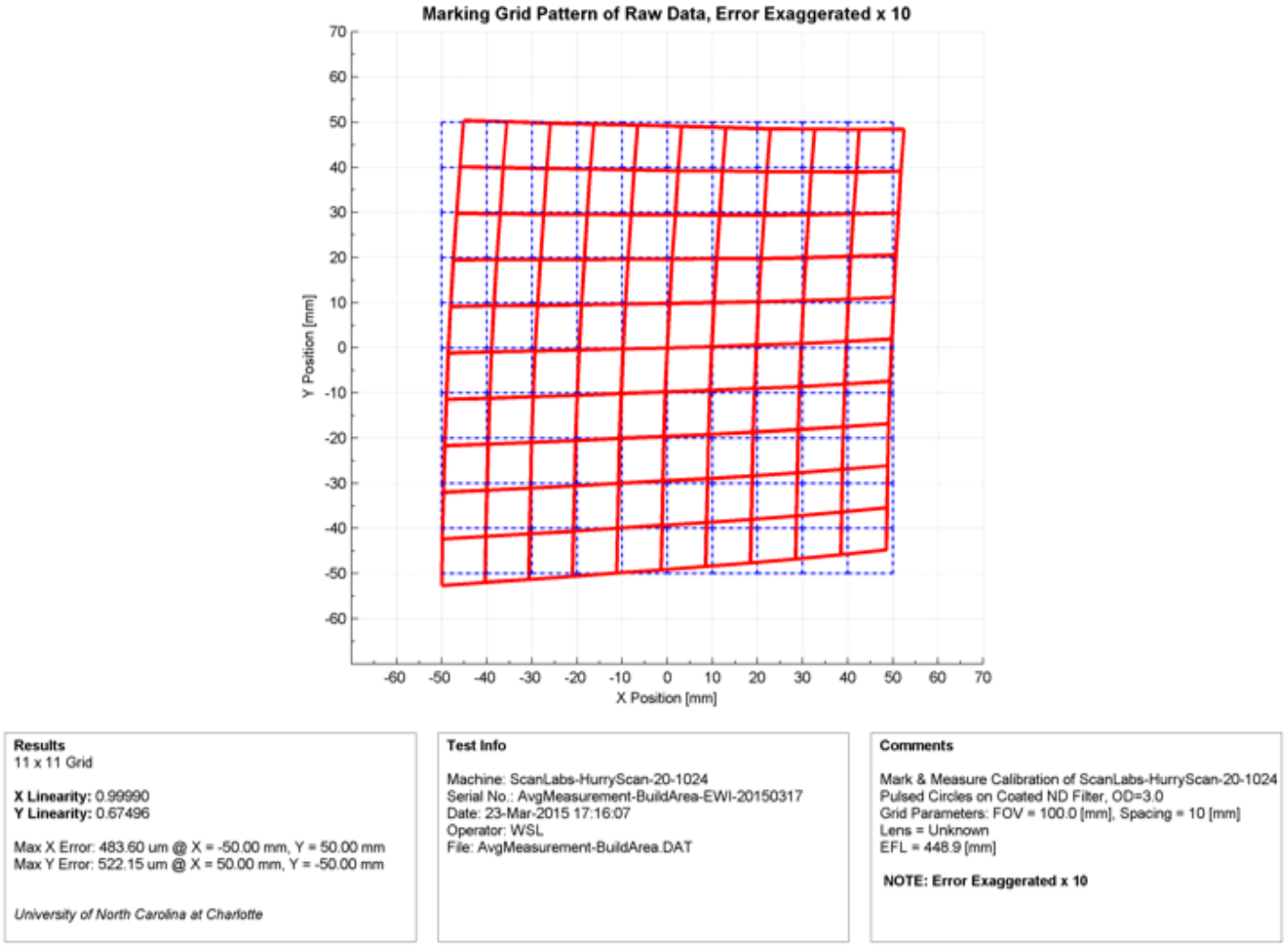

Figure 2.36: Grid plot of the average measured mark position the fusion chambers build area relative to nominal with errors exaggerated tenfold.

2.5.4 Summary & Conclusions

The most notable feature of the measurement results presented above is the overall magnitude of the scanner errors present over its entire field of view (FOV). This is not unexpected as scanners not calibrated via an in-situ mark and measure have displayed similar levels of inaccuracy in previous work. As mentioned, the goal of the chosen substrate and marking procedure was primarily to isolate spot placement errors associated with laser alignment (also known as zero offset) error, as described in Section 2.3.4. The errors captured in the marked grids clearly show spatial distortion of laser spot placement due to the lens assembly. Although the operator was using a manufacturer prepared theoretical lens correction file, the corrections made by the file are invalidated by the laser's imperfect alignment to the scanner system. In the powder fusion chamber's particular optical path setup, there is approximately 300 millimeters of beam path between the laser collimator, and the entrance aperture of the scan head. Inside the scan head itself there is approximately an additional 150 millimeters of beam path before the focused beam enters the f-theta lens' aperture. Therefore, a one degree misalignment in the mounting of the laser collimator would cause approximately 7.8 millimeters of lateral shift in where the zero beam hits the input aperture of the f-theta lens. (To reiterate, the zero beam is the location of beam spot placement when scanner axes are commanded to nominal zero.) Between this lateral shift and the effects of the 1 degree incoming beam angle applied to the f-theta characteristic of the lens, the lateral shift of the beam spot within the focal plane would approximately be 15.7 millimeters of zero offset. This means that the magnitude of each correction provided by the manufacturer's theoretical calibration would be disassociated with its proper position in the FOV by this 15.7 millimeters. Such a zero

offset error will cause hundreds of microns of spot placement error, and is likely the cause of most of the distortion seen in the figures presented above. Without a complete spot placement simulation from the lens manufacturer it is difficult to accurately state quantitatively the zero offset shifts error contribution.

An additional source of notable error in the measured marked grids is the constant overshoot in grid spacing from commanded nominal. This larger grid pitch manifests as a tilted plane in each of the X and Y axis error plots, and is more easily described by the average step size of each measurement. Such a consistent oversizing of each marked grid is indicative of an offset in marking height, as described by Section 2.3.2. The laser beam is projected through a range of non-normal incident angles on the substrate surface, and an increase in distance between the scanner's lens assembly and the substrate would produce larger than commanded grid pitches as described. Therefore, it is hypothesized that the selected marking field, or vertical placement of the powder surface relative to the scanner, is slightly off from the nominal position of the f-theta lens' focal plane. This can be a common problem in such laser systems because of the relatively large depth of focus produced by many f-theta lens. If the assembler of the fusion chamber could not determine a change in the laser's focused spot diameter via mark quality, then determining the appropriate working height of the powder surface is difficult to select with any level of precision. Given that the particular scanner system employed by the laser fusion chamber produced a maximum scan angle of approximately 15 degrees, a vertical offset between the marking field and focal plane of less than a half a millimeter would produce the average overstep of 40 micrometers seen over the measured FOV. This seems reasonable as no

apparent change in laser spot focus could be quantitatively measured through a marking field height change of over 1 millimeter.

Beyond the two specifically discussed potential causes of the scanner's spot placement error, it is difficult to precisely determine all error contributors. The main takeaway of these results should be that laser scanner spot placement can contain large errors even though the scanner system may come with a theoretical correction file from the manufacturer. The error sensitivities discussed throughout Section 2.3 can drastically impact laser placement, and without a measurement of their influence an operator cannot be assured of any level of laser spot placement accuracy. Below, in Table 1, is a summary of the measurements from each of the scanner's FOV quadrants, as well as the average of the four substrates marked in the specific build area portion of the scanner's FOV.

Table 2.1: Summary of laser spot performance over its entire field of view, and its performance over the area of used during part builds.

		Quadrant 1	Quadrant 2	Quadrant 3	Quadrant 4	Build Area
Measured FOV Range	**X-Axis [mm]**	[0, 100]	[-100, 0]	[-100, 0]	[0, 100]	[5, 105]
	Y-Axis [mm]	[0, 100]	[0, 100]	[-100, 0]	[-100, 0]	[-25, 75]
Peak-Peak Accuracy	**X-Axis [µm pk-pk]**	716.3	677.4	1330.3	1522.3	784.1
	Y-Axis [µm pk-pk]	827.2	812.5	194.3	232.4	641.7
Vector Sum Error [µm pk]		614.1	609.6	742.8	893.1	541.2
Nominal Grid Spacing [mm]		10.000	10.000	10.000	10.000	10.000
Average Measured Grid Spacing [mm]		10.035	10.030	10.045	10.052	10.040
X-Y Orthogonality [arc-sec]		785	404	439	593	737

2.6 Uncertainty Analysis of Machine Characterization

There are two major uncertainty contributors to the marked substrate measurements presented in Section 2.5. One major contributor to measurement uncertainty is the influence of the measurement machine's rigid body error motions on its output. The second

is the combination of measurement and marking repeatability previous discussed in Section 2.4.1, caused by the fitting of circles to non-circular, quasi-randomly shaped burn marks. The quantification of these contributions was carried out independently.

The machine used to measure each substrate was a Nikon MM-400 measuring microscope. It consists of a machine vision system positioned vertically over a two axes XY stack of manually operated lead screw driven stages. Each stage has a linear optical encoder, which provides positioning resolution below a tenth of a micrometer. The measurement range of the device is approximately 105 millimeters square, and offers top surface and back surface illumination for light field and dark field imaging techniques. A Nikon provided image of the device is given below in Figure 2.37.

Figure 2.37: An image of a Nikon-MM400 Measuring Microscope used for marked substrate measurement

Several of the Nikon microscope's rigid body error motions were characterized so that their effects on measurement accuracy could be quantified. The impacts of machine rigid

body error motions is widely known throughout many industries, and is well documented in a plethora of texts, including Slocum's Precision Machine Design [6].

The linear accuracy of both the X and Y axis' scale was validated by a two point measurement of a 4" lab grad 00 gauge block. (A copy of the gauge block set's calibration certificate can be found in the Center for Precision Metrology's metrology lab at UNC Charlotte.) The 4" gauge block was rung together with two smaller gauge blocks of arbitrary length at both ends and put on the microscope table top. Then the machine vision system was used to fit a line, using a proprietary contrast transition algorithm, to the ringing film at one end of the gauge block stack. The stage under measurement was then translated, recording the distance traveled, until the ringing film at the other end of the 4" gauge block was directly underneath the machine vision objective. Another line fit was created, and the distance between the ringing films at either end of the 4" gauge block was recorded. This process was repeated 10 times for both the X and Y axis, producing a peak to peak measurement error of approximately 1 micrometer.

Next, the straightness of the each axis was checked using a Brown & Sharpe digital indicator and a steel reference square. (A copy of the steel reference square's calibration certificate can be found in the Center for Precision Metrology's metrology lab at UNC Charlotte.) As the form errors associated with the steel reference square were well below the level of measurement uncertainty required by the marked substrate measurements, no reversal techniques were used to remove them from the measurement. Several validation measurements of each axis were carried out, showing a maximum straightness error of either axis to be approximately 0.75 micrometers.

The squareness of the two axes was also measured using the aforementioned indicator and steel square. The squareness measurement, using a two point line fitting approach, yielded 60 microradians. Applied over the full grid measurement area of 100 millimeters could lead to a maximum measurement error of approximately 6 micrometers.

The yaw of the X-axis carriage was measured by an Elcomat autocollimator, using a flat mirror mounted to the center of the microscopes tabletop. The error motion proved to be less than 20 microradians, the minimum resolution of the autocollimator model in use. The X-axis measurement were taken to be indicative of the Y-axis error motion considering the similar construction and previous performance of the two stages. Again, applying this level of carriage yaw over the full 100 millimeter measurement area could yield a maximum of approximately 1.8 micrometers of error.

Finally, the parallelism of upper and lower surfaces of the individual glass substrates being measured and its effect must be taken into consideration. Just as during the marking of each substrate as discussed previously, the parallelism of the upper surface of the marked substrate to the microscope's plane of motion will impact measurement accuracy. This parallelism is specified by the manufacturer to be less than 100 microradians, resulting in maximum measurement error of less than 1 micrometer. The machine rigid body error motions described above are assumed to be uncorrelated, and therefore, their total contribution to measurement uncertainty is estimated by their sum in quadrature. A table summarizing their overall contributions to uncertainty is presented below in Table 2.2.

Table 2.2: Summary of measurement uncertainty contribution from the rigid body error motions of the Nikon Microscope Measuring Machine during characterization of laser marked grid plates.

Nikon Measuring Microscope Rigid Body Error Motion Uncertainty Contribution	
Uncertainty Source	Contribution [µm]
Linear Accuracy, < 1.0 [µm]	1.0
Squareness, < 60 [µrad]	6.0
Straightness, < 1.0 [µm]	1.0
Estimate of Yaw, < 20 [µrad]	1.3
Substrate Parallelism, < 100 [µrad]	1.0
Combined Standard Uncertainty	6.4

The second major contributor to the uncertainty of measuring the marked substrates, previously discussed as measuring and marking repeatability in Section 2.4.1, had to be quantified via a Type A, or statistical uncertainty analysis, as outlined by the guide to the expression of uncertainty in measurement (GUM) [15]. Each mark's position in any of the measurements mentioned hereafter was determined by producing 100 data points equally spaced around the mark at the position of highest contrast transition. A least squares parametric circle fit was then applied to the set of 100 points, and the center of this best fit circle is claimed to be the center of each laser mark. The microscope was slightly defocused as to smooth the contrast transition between dark to light; it was found to reduce uncertainty in the measurement of a spot center. As mentioned, the specific contrast transition algorithm used by the Nikon machine to determine the best location of each of the 100 data points per mark is unknown. However, its repeatability and contribution to the measurement uncertainty for each grid can be quantified via statistical testing. An example of an individual laser mark, its defocused image, and the machine vision's fit of

data points to the image of a different mark are shown below in Figure 2.38 and 2.39 as examples.

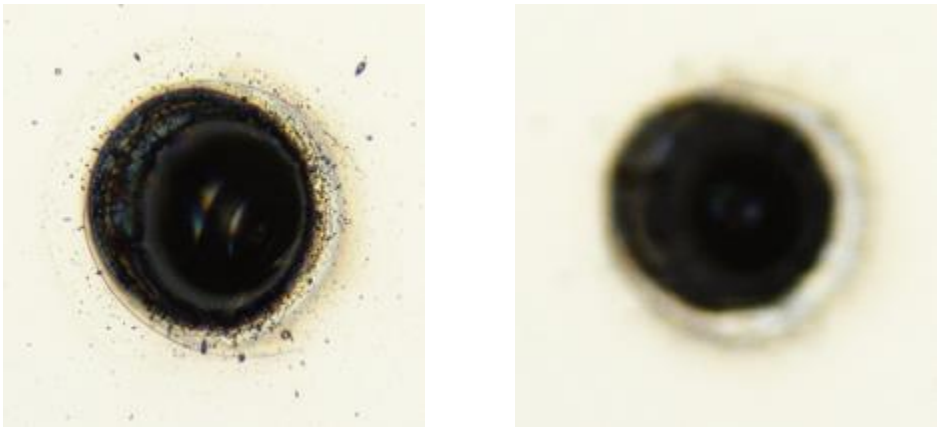

Figure 2.38: An image captured from the Nikon-MM400 showing a typical laser mark (left), and that same image defocused (left) for the purpose of smoothing the contrast transition band.

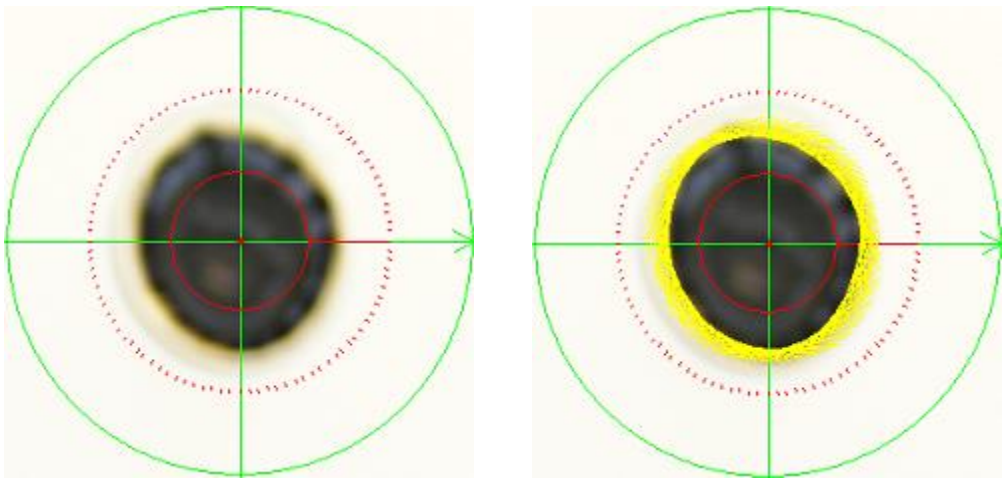

Figure 2.39: An image captured from the Nikon-MM400 showing a laser mark before the contrast transition algorithm is used to find the edge of the mark (left), and that same mark with the image locations and tangent lines selected to represent the mark edge (right).

First, several individual marks, arbitrarily selected from within various substrate grids, were chosen to be indicative of the variation seen in marks throughout all of the grids. For each chosen mark, its center location was found a minimum of ten times sequentially. In between each subsequent determination of a mark's center location, the positioning stages

were used to move the mark out of the machine objective's field of view and back. Such tests were used to establish the repeatability of finding any individual mark's center. The worst peak to peak deviation seen in the determining of any mark's location was less than half a micrometer. This is a quantification of the fore mentioned measurement repeatability from Section 2.4.1.

The more important contribution to measurement uncertainty in the mark center determination process comes from the inherent randomness in creating a laser mark through a burning process. As previously described, every laser mark made in the same location with the scanner's field of view will have a slightly different shape. As such, each will have a slightly different determined center as a result of the machine vision's circle fit. This variation in spot location due to mark randomness is what was described in Section 2.4.1 as marking repeatability. Marking repeatability was quantified in this case by calculating the standard deviation between each individual grid location in the four substrates marked over the build area portion of the scanner's field of view. As these substrates were marked in rapid succession, with the same parameters, it is assumed that any variation seen in their measurement is due to primarily marking repeatability. The largest standard deviation of any grid location over the four substrate measurements was approximately five micrometers. This allows the uncertainty of the entire substrate measurement process to be quantified as the root sum square of the machine rigid body error motion contribution and the machine vision contributions when determining a laser mark center. Below, Table 2.3 and 2.4 summarize the uncertainty contributions of the mark center measurements and the total uncertainty of the measurement of marked substrate grids.

Table 2.3: Summary of measurement uncertainty contribution from the machine vision measurement process during Nikon Microscope Measuring Machine characterization of laser marked grid plates.

Nikon Measuring Microscope Laser Mark Center Determination Uncertainty Contribution	
Uncertainty Source	Contribution [µm]
Measurement Repeatability	0.3
Marking Repeatability	5.0
Combined Standard Uncertainty	5.0

Table 2.4: Summary of total measurement uncertainty in characterization of laser marked grid plates by Nikon Microscope Measuring Machine.

Total Measurement Uncertainty of Marked Substrates Measurement Using Nikon-MM400	
Uncertainty Source	Contribution [µm]
Error Motions of Nikon-MM400	6.4
Laser Mark Center Determination	5.0
Combined Standard Uncertainty	8.1
Expanded Uncertainty (k=2)	**16**

CHAPTER 3: IN-PROCESS METROLOGY OF LASER SINTERING

3.1 The Metrology System

This chapter discusses the development of a metrology system to perform in-situ measurement of powder surfaces specifically within the laser powder bed fusion chamber at Edison Welding Institute. The development of this system has been a collaboration between both the Mechanical Engineering department and the Optical Science department at UNC Charlotte. Specifically, the author of this document has worked jointly with Bin Zhang, a doctoral student in the Optical Science department, and much of this chapter represents his contributions to the project. Many of the details of the metrology system and results of preliminary measurements have been published by Zhang, et. al. and Land, et. al in various conference proceedings [16, 17]. As discussed in Section 1.1, the goal of this process is to measure each individual layer during a build process as a means of capturing geometric features of a part that will be obscured in its final form while they are still accessible. The approach to measuring each sintered layer described here involves the combination of a traditional machine vision system and a digital fringe projection system. The fringe projection technique is used to calculate the area height profile of each layer, while a machine vision algorithm provides the proper planar mapping from camera pixels to in-plane object coordinates. A schematic of the measurement system as mounted on the laser fusion chamber is shown below in Figure 3.1. The process involves the use of one digital single-lens reflex (SLR) camera and a digital light processing (DLP) projector.

Three cameras have been integrated into the fusion chamber for the purpose of future advancement of the measurement process. The availability to measure the powder surface from multiple angles will provide means for a more robust measurement as this project progresses. The primary means of determining the solid-powder boundary within each sintered layer of a build is the measurement of the height profile. The laser powder bed fusion system studied here uses IN625 nickel alloy powder as its printing media. The solidification of this particular powder by sintering causes approximately a 40-50% increase in density, known as consolidation. Hypothetically, the powder regions exposed to the laser during sintering will therefore experience a measureable drop in height as compared to the unaltered regions. By comparing the surface profile of a layer after sintering to a baseline area profile of that same layer prior to laser exposure, the goal of the system is to distinguish solidified area from powder through examining relative height change. Additionally, system operators are interested in the height profile of the powder surface as a means of evaluating hardware performance, flagging possible build errors, and potentially as a path to closed loop feedback for the build system. As noted, the measurement of lateral and vertical coordinates within the powder bed occur independently of each other, and as such, each requires its own calibration and data processing procedure, as will be discussed below.

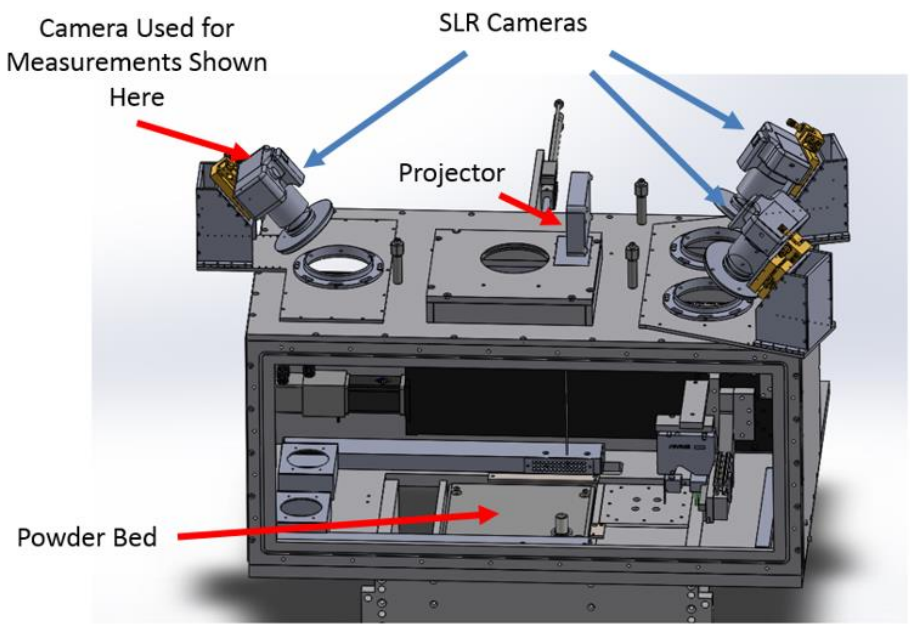

Figure 3.1: Schematic of measurement systems' integration into the laser powder bed fusion chamber at Edison Welding Institute. The camera used to produce the measurements shown in this paper is that shown on the left of the figure.

3.2 Principle of Operation

3.2.1 Planar Coordinate Measurement via Machine Vision

Measuring the planar coordinates of locations within the build area is performed through the processing of a single image of each sintered layer. This measurement relies on the linear mapping of pixel coordinates within each image to an established reference coordinate system within the test chamber. The mapping is created through a calibration procedure, and the calibration's stability, and therefore future measurement accuracy, depends on the spatial relationship between the camera and the build plane remaining constant. As such, rigid fixturing is required to maintain image space orientation throughout the entire build process. The measurement process can be broken down into two basic steps, initial calibration and image mapping.

The calibration process requires a grid plate to be used as a reference artifact. The plate contains an 11 x 11 grid of 7.5 [mm] reamed holes of constant 15 [mm] 2D pitch, thereby covering an area of 150 x 150 [mm]. The pattern has been measured using a CMM contact probe to establish the hole centers at the upper surface of the plate. This measurement and a measure of its uncertainty is used as the global reference for the creation of both a projective transformation matrix and a linear mapping of orthogonal pixel coordinates to metered space, which collectively define the calibration of the system.

After the CMM measurement of the grid plate, the holes were back filled with a non-expanding epoxy to create a flat upper surface for imaging with high greyscale contrast at the hole edges. To calibrate the measurement system, the grid plate is imaged within the chamber where it fully encompasses the area where powder will be fused. Using linear stages within the chamber, the reference artifact is positioned so that its upper surface coincides with the marking field of the laser scanning system, or the "build plane". The image of the grid plate is processed using a contrast thresholding algorithm in order to perform circle fitting to the back filled holes within the plate.

Using the relative center location in pixel coordinates of each hole by means of a least squares circle fit, an inverse projection transformation matrix is calculated using the CMM measured part coordinates of the four corner circles. The projective transformation matrix shown in Eq. 3 is the first output of the calibration procedure. It is used to correct perspective warping in the non-orthogonal images taken of the powder bed. The projective transformation T is defined as,

$$\boldsymbol{T} = \begin{bmatrix} a_{11} & a_{12} & a_{13} \\ a_{21} & a_{22} & a_{23} \\ a_{31} & a_{32} & a_{33} \end{bmatrix} \tag{3}$$

such that,

$$[x'\ y'\ w'] = [u\ v\ 1] \cdot \boldsymbol{T} \tag{4}$$

where [u v] are coordinates in the original image space, and [x'/w' y'/w'] are coordinates in orthogonal planar object space [18]. The transformation matrix calculated from Eq. 3 and 4 during the calibration process is saved and used to remove perspective warping in all future images from the system under the assumption that the imaging system is geometrically stable. The projection transformation matrix is then applied to the entire calibration image to remove the planar perspective warping. This creates an orthogonal image of the grid plate artifact. An example of a processed and transformed image of a calibration grid is shown below in Figure 3.2.

After transformation, to create the linear mapping from orthogonal pixel space to metered space, the relative circle centers in the transformed image are compared to their known relative locations as measured by the CMM. The ratio of the two locations gives a map of linear scaling factors in millimeters per pixel at each of the hole locations within the transformed camera image. The mapping is defined as,

$$\boldsymbol{S}_{x,y}(i) = \frac{\boldsymbol{P}_{CMM_{x,y}}(i)}{\boldsymbol{P}_{OrthoImage_{x,y}}(i)}\ [\frac{mm}{pixel}] \tag{5}$$

Once calculated from the imaging of the calibration grid plate, the scaling map, $\boldsymbol{S}$, may be applied to subsequent images of the same planar space without the grid plate, converting their image coordinates to metered space by,

$$[x\ y] = \boldsymbol{S} \cdot \left[\frac{x'}{w'}\ \frac{y'}{w'}\right]\ [mm] \tag{6}$$

such that P_{CMM} is the vector of X and Y locations for each hole in the grid plate in millimeters, and $P_{OrthoImage}$ is the vector of X and Y locations for each hole in the transformed orthogonal image of the grid plate in pixels. Therefore, Eq 5 implies that any

image taken by the calibrated system can be transformed via Eq 3 & 4 and scaled by ***S*** to arrive at pixelated metered units in the image.

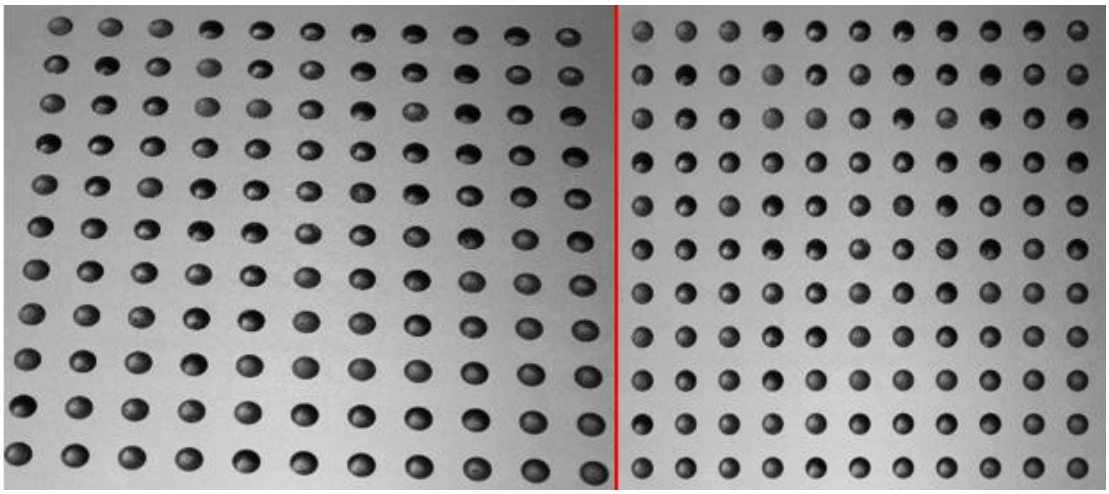

Figure 3.2.: Left is the unaltered image of the calibration grid artifact taken by the imaging system during lateral calibration. The right is the same image in orthogonal space after perspective warping has been removed via planar projection transformation [18].

3.2.2 Digital Fringe Projection System

The measurement of the area height profile is carried out via the projection of light with sinusoidally varying spatial intensity and a traditional phase shifting algorithm. The intensity distributions generated by the DLP projector on the power bed can be expressed as,

$$I_1(x,y) = I_0(x,y) + I_m(x,y) \cdot cos\big(\phi(x,y)\big) \tag{7}$$

$$I_2(x,y) = I_0(x,y) + I_m(x,y) \cdot cos\left(\phi(x,y) + \frac{\pi}{2}\right) \tag{8}$$

$$I_3(x,y) = I_0(x,y) + I_m(x,y) \cdot cos(\phi(x,y) + \pi) \tag{9}$$

$$I_4(x,y) = I_0(x,y) + I_m(x,y) \cdot cos\left(\phi(x,y) + \frac{3\pi}{2}\right) \tag{10}$$

where $I_i(x,y)$ is the intensity at each pixel in one of four pictures captured in the process, $I_0(x,y)$ is the offset intensity in the system, $I_m(x,y)$ is the modulation intensity, and

$\phi(x,y)$ is the phase which is desired to be known at each pixel. Solving Eq. 7 through 10, we obtain the phase as defined by Eq. 11, below.

$$\phi(x,y) = \tan^{-1}\left(\frac{I_4(x,y) - I_2(x,y)}{I_1(x,y) - I_3(x,y)}\right) \tag{11}$$

Through a calibration process, this relative phase information can be turned into relative height information by,

$$h(x,y) = \lambda_{eff}(x,y) \cdot \phi(x,y) \tag{12}$$

where $\lambda_{eff}(x,y)$ is called the effective wavelength at each pixel. It is defined as height change per fringe cycle, and is the output of the calibration procedure [19].

The height information produced must be of sufficient resolution to accurately and robustly resolve the anticipated height drop of nearly 40 micrometers used in determining the solid-powder boundary. The most important factors in determining the resolution of the height map is the spatial frequency of the projected fringes onto the build plane, and the geometric arrangement of the imaging hardware. The placement of hardware in this case is largely dictated by the chamber size and available space given the many integrated sensors and ancillary equipment. Likewise, the ability to increase the spatial frequency of projected fringes is limited by the pixel density of the projector in use. It is beneficial to have multiple pixels per span of greyscale intensity in the fringe pattern to minimize noise and aliasing within the output phase map.

3.2.3 Combining Area Height Profiles with Lateral Measurements

Once both calibrations are complete, fringes can be projected, shifted and imaged for each build layer, and a height map of the fused and un-fused powder surface can be created. Using the machine vision procedure outlined in Section 3.2.1, each pixel within the build area can be assigned relative lateral (X, Y) position. Once the sintered region is determined

through relative height change, a layer-wise point cloud of the part being produced could be obtained. Using data from the vertical stages within the chamber, each layer of data points can be stacked together in post-processing to produce a 3D point cloud that represents the part produced in its entirety, including all obscured features once it is in final form. This high density 3D point cloud is a major goal of the measurement system, however, it relies on several assumptions to be successful. In particular, it assumes that the imaging system is geometrically stable relative to the build area, and it will not take into account any part errors associated with the rigid body motions of the build platform as described in Section 2.1.2.

3.3 System Calibration

3.3.1 Lateral Calibration of the Metrology System

As noted, after the appropriate transformation matrix and map of linear scaling factors have been established, they can be applied to subsequent images from the same stationary system. Post calibration imaging, the grid plate is removed from the chamber, and powder is introduced. The linear stages within the chamber bring the powder bed level with the focal plane of the lasing system. This coincides with the plane of system calibration; and matching the planes of powder bed, laser focus, and calibration is necessary for both quality sintering and measurement. Once the layer of powder has been sintered, an image of the entire build area is captured. The image is then transformed into orthogonal space, and the entire image is passed through the linear mapping from pixels to metered units.

Since the map only has scaling factors at the locations and pitch of the grid plate artifact, each pixel undergoes a bi-linear interpolation within the map to determine the approximate scaling at every pixel location. The mapping of pixel coordinates to metered

space is carried out independently for the X and Y directions respectively, each having their own scaling maps. Below, in Figure 3.3, is a visualization of the lateral errors seen

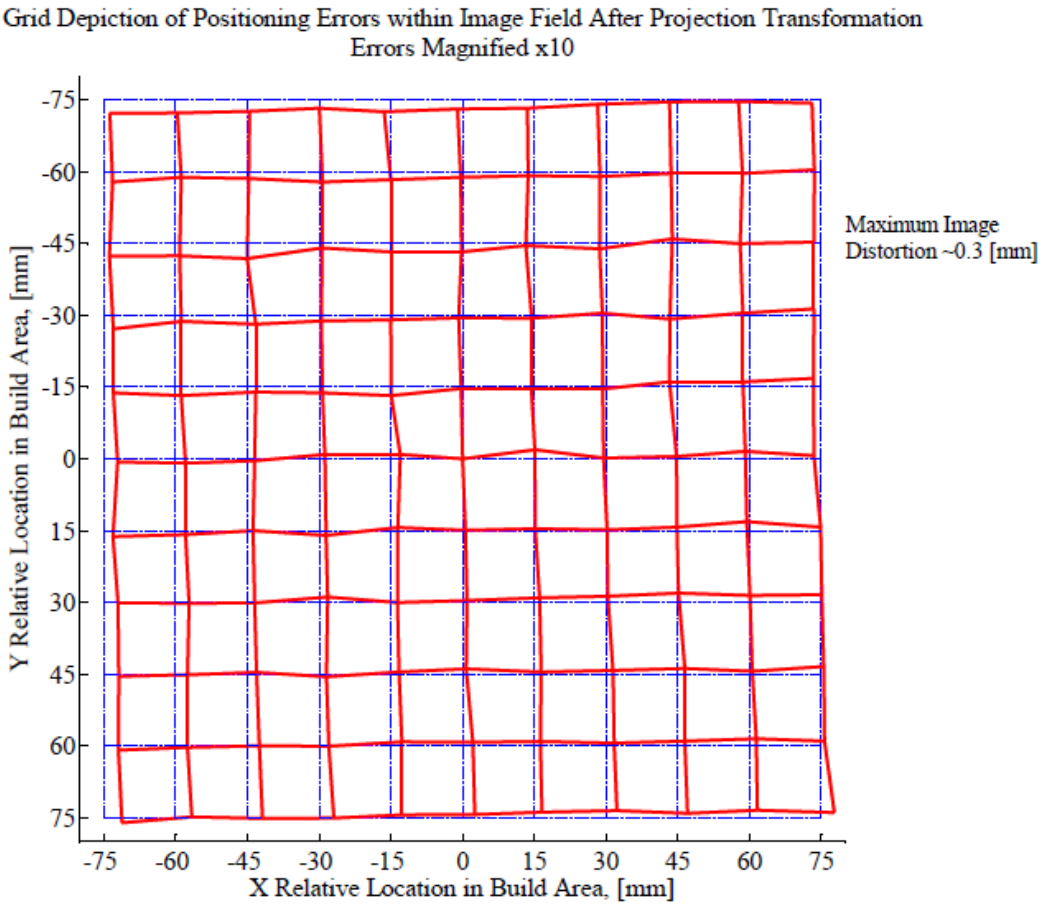

Figure 3.3: A visualization of the lateral spatial distortions seen in the uncalibrated image of the grid plate reference artifact due to imperfect de-keystoning and lens distortions. The intersections of the red lines depict the locations of each hole in the grid plate within the camera image as compared to the blue lines which are the hole locations as measured by a CMM. NOTE, the difference in hole position is magnified tenfold for graphical purposes.

in the uncalibrated orthogonal image space as compared to the calibration grid plate's measurement by tactile CMM. These special distortions are largely due to a simplified and imperfect calculation of the projection transformation matrix, as well as internal camera distortions. They are removed through the application of the X and Y scaling map.

3.3.2 Vertical Calibration of the Metrology System

As described in Section 3.2.2, the conversion of relative phase to a relative height measurement requires the calculation of an effective wavelength. This procedure is called effective wavelength calibration and requires a diffuse flat plate as a reference artifact and a vertical motion translation stage. By counting the number of fringe shifts at the center of the flat plate while recording the corresponding height change, the effective wavelength can be calculated as a simple ratio of the two. However, this approach is only capable of roughly estimating the effective wavelength of the system. A more accurate calibration involves capturing phase at each step height and mapping the effective wavelength at each pixel over the whole field of view [20].

During the calibration, the plate is translated vertically above and below the build plane in equal increments by the build platform's stage. Calibration within the fusion chamber consisted of a 1 mm height range centered around the build plane where incremental steps of 0.1 mm were used to generate the effective wavelength calibration. At each height location, phase shifting and phase unwrapping techniques are applied to obtain the initial phase within the build area. Then the slope of height per initial phase is derived by a least squares fitting of a line at each pixel as shown in Figure 3.4. Since the image space is assumed to remain static relative to the build plane, each pixel is already intrinsically associated to its relative lateral location within the image.

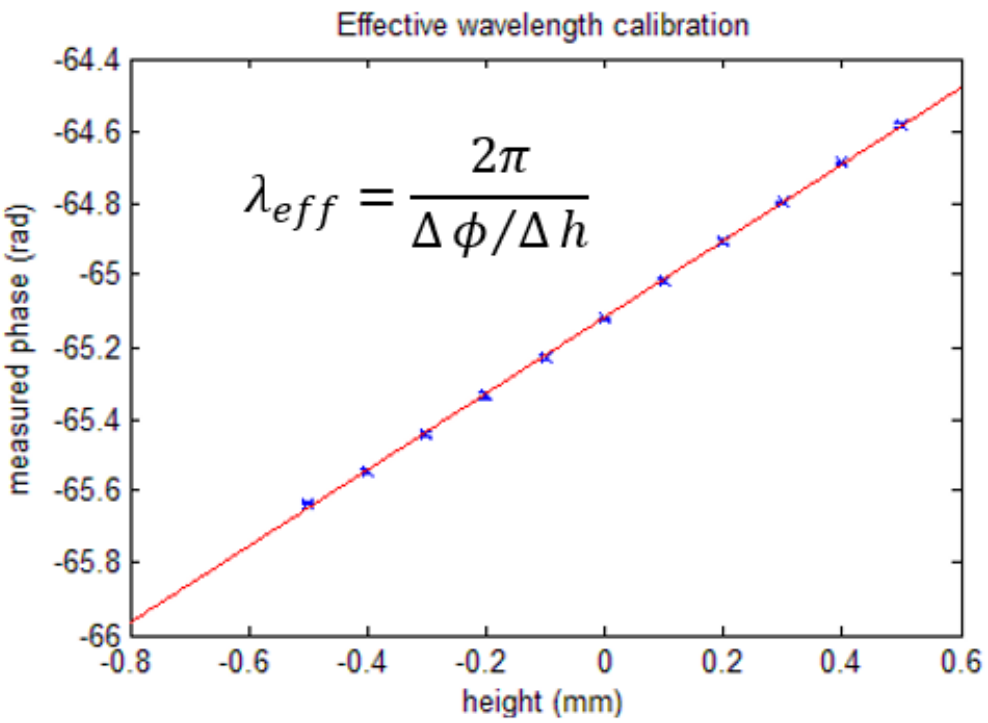

Figure 3.4: An example of the calculation of the effective wavelength for one pixel within the measurement image space. The figure shows the change in phase on the vertical scale of a single pixel as the vertical translation stage moves the calibration flat through a height range on the horizontal scale. The effective wavelength is shown as two pi divided by the slope of a least squares line fit to the tracked phase change.

3.4 Measurement of Build in Progress

3.4.1 Test Procedure

Test builds were imaged at Edison Welding Institute as a means of proving the metrology system concept. Primarily, each test build consisted of a group of six, 10 millimeter square pillars, separated laterally by approximately 3 millimeters. Each pillar was built using a raster scan pattern during laser fusion. The raster pattern was rotated 90 degrees between the fusion of each layer to produce the best results as decided by the chamber operators. Each square pillar was built for a limited number of layers, ranging from 5 total layers to 30 total layers of fused powder in order to measure the material

build up in the final part as a function of layer powder thickness and total number of layers fused. This information is ancillary to the primary goal of height profiles and can be found in Appendix A. Below, in Figure 3.5, a raw greyscale image of the build in-process is shown.

The first layer of powder distributed on the build platform is imaged and used as a height reference for which to compare each subsequent layer. Additionally, Legendre Polynomial fits, up to third order, to the measurement of the first powder layer are subtracted from each measurement as a means of eliminating measurement distortion. The zeroth and first order removes piston and tilt of the measurement; the second order and third order fit remove distortion due to perspective warping and internal camera

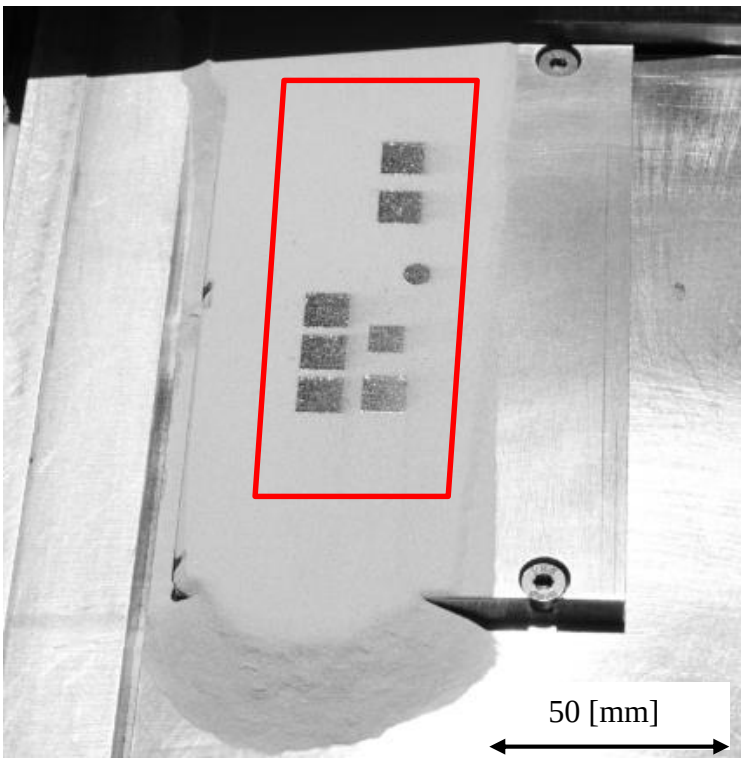

Figure 3.5: An example image taken during a test build at the EWI facility. Several of the square pillars are covered by powder at this point in the build process. The image shows only a portion of the camera's field of view. The outlined area is the portion of the image space analyzed and turned into surface profiles for the particular build shown.

distortion respectively. Additionally, spatial Fourier filtering is applied to the measurement data to eliminate some harmonic noise due to fringe bleed-through during the phase unwrapping process.

Measurements were made at three steps during each build layer cycle. The first measurement images were captured immediately after the powder recoating arm laid a fresh layer of powder. Second, a measurement was made immediately after laser fusion of the powder. Finally, measurement images were captured after the build platform had dropped the nominal layer thickness of 40 micrometers and the powder recoating arm had returned to its original position. The third measurement in each layer was to track the consistency of build platform motion and layer thickness consistency throughout the build process. Below, Figure 3.6 gives an illustration of the measurement points during each build layer.

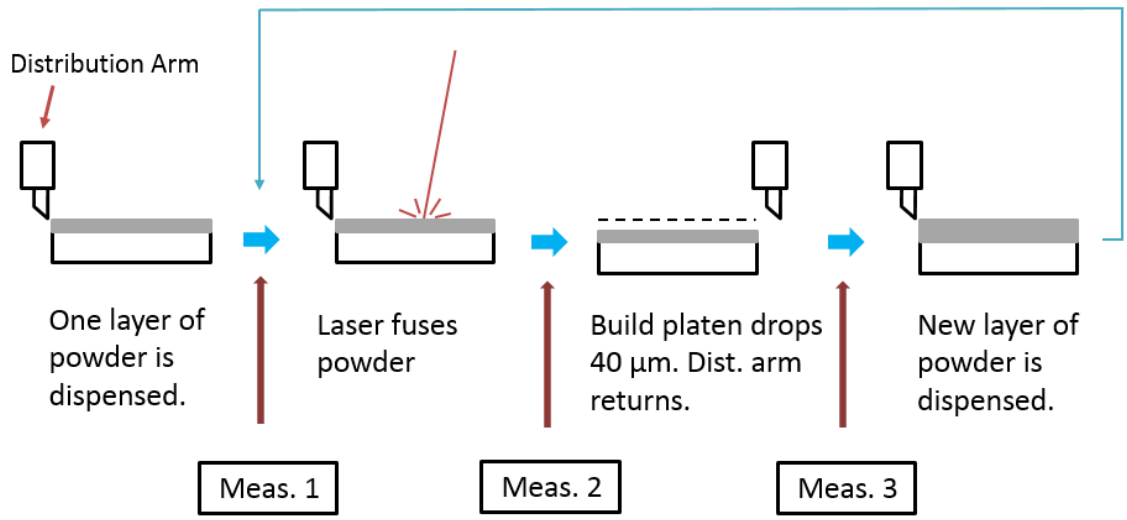

Figure 3.6: An illustration of the measurement points during each build layer cycle.

3.4.2 Results

Results from the measurement of the 30 layer test build are presented below. Data are presented as greyscale height maps. Although the plots appear similar in aesthetic to the greyscale raw images from the camera system, the greyscale here is a measure of relative height. A local close-up example of the data shows its detailed 3D textural content below, in Figure 3.7. Each subsequent figure will show data from the first two measurements made of each build layer as described by Figure 3.6. The final measurement system was able to achieve a lateral resolution of 60 micrometers per pixel, and current vertical measurement fidelity is limited by a peak to valley noise floor of approximately 20 micrometers. Only a fraction of the total surface plots created will be displayed here.

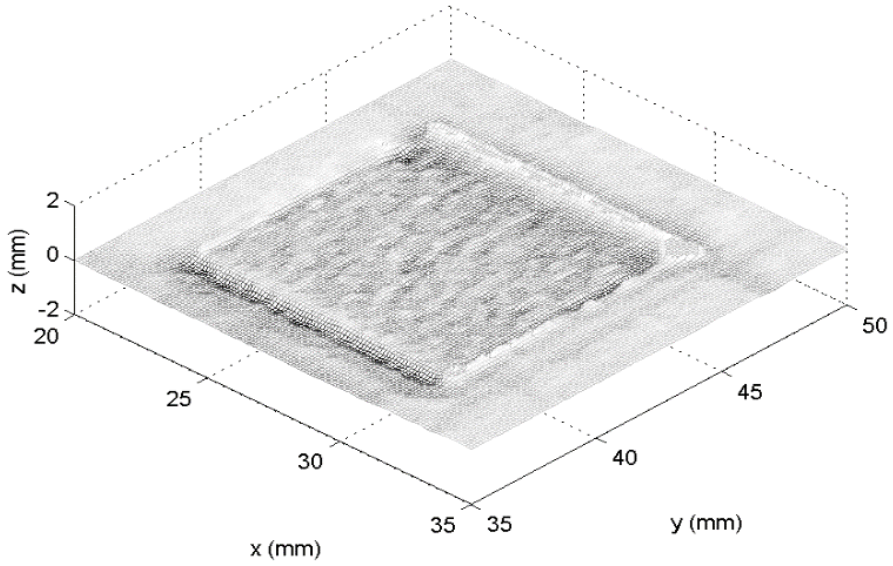

Figure 3.7: An isometric view of local data from a measurement of one of the square pillars during a test build. Relative height information is plotted in greyscale.

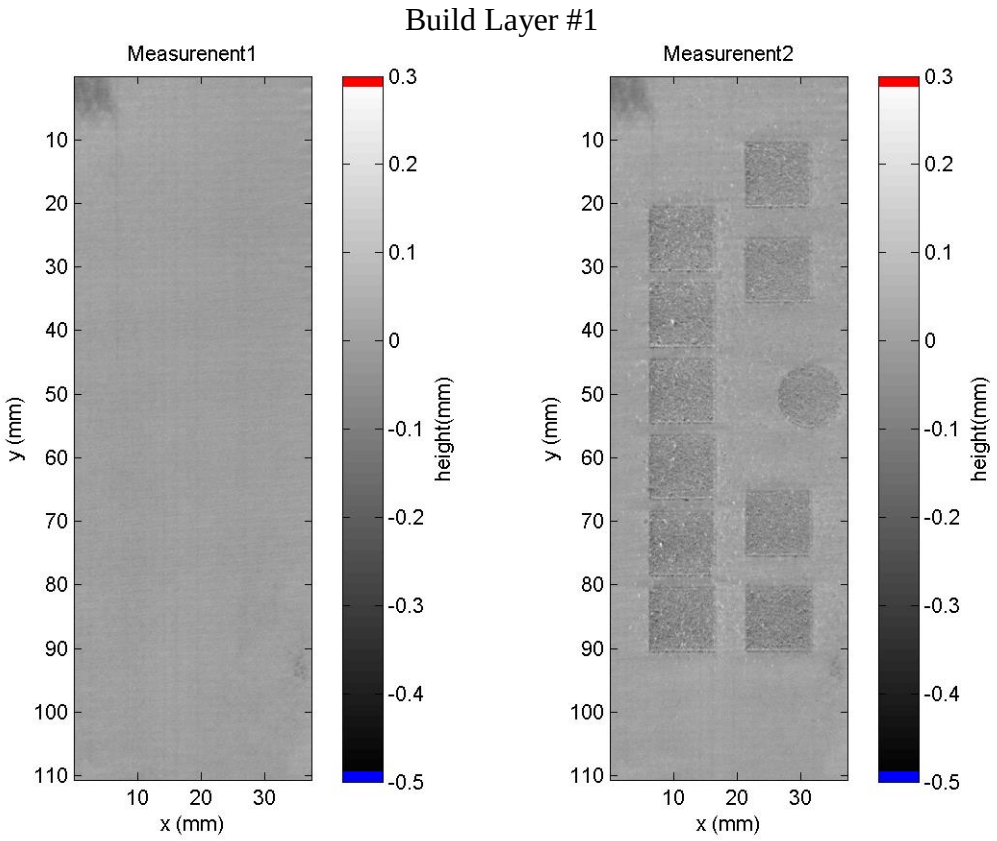

Figure 3.8: Height measurements of the initial powder surface prior to laser fusion (left), and the same powder after fusion (right) of build layer 1.

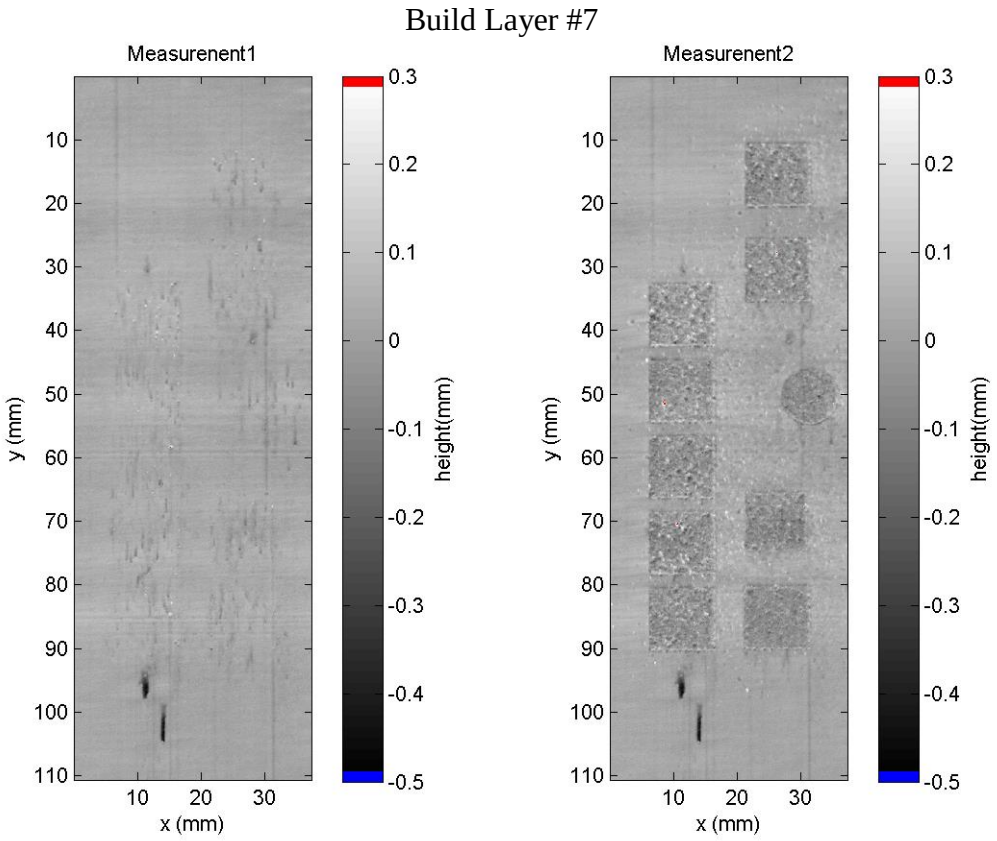

Figure 3.9: Height measurements of the initial powder surface prior to laser fusion (left), and the same powder after fusion (right) of build layer 7.

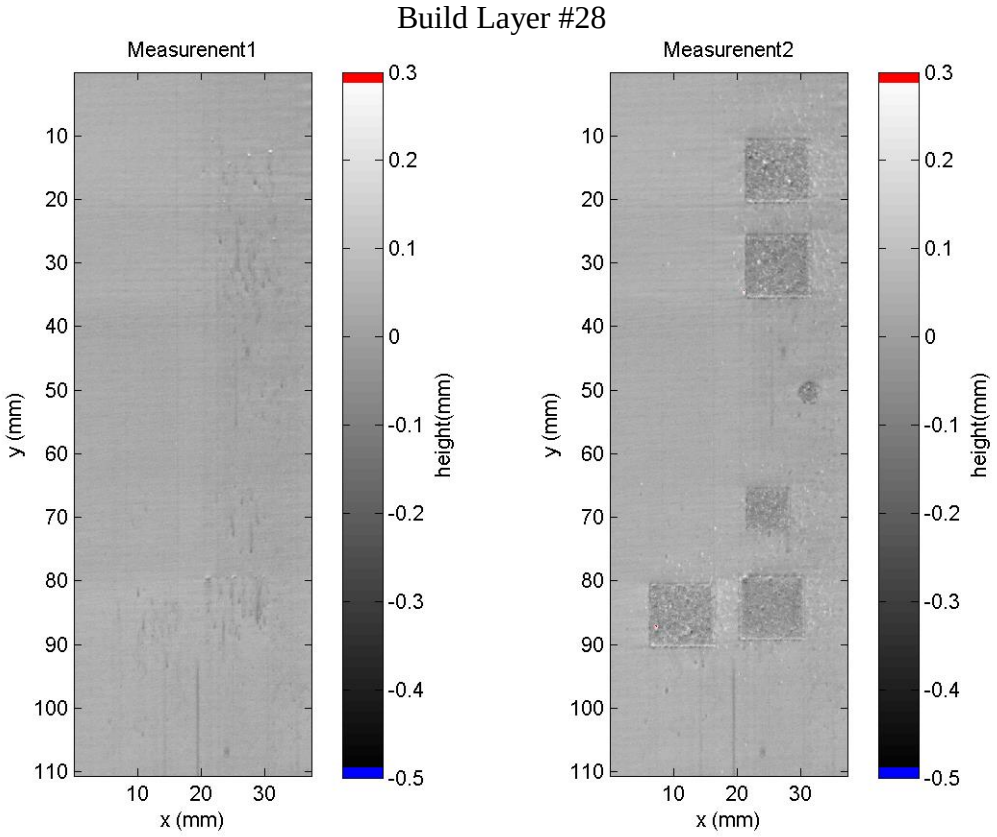

Figure 3.10: Height measurements of the initial powder surface prior to laser fusion (left), and the same powder after fusion (right) of build layer 28.

From this small subset of measurements, one can clearly see a difference in the average height of fused area when compared to each layer's initial height. However, when observed more closely, the apparent qualitative height difference is not so easily distinguishable quantitatively. Additionally, it is possible to see waviness in the unfused powder as clearly shown by Figure 3.9. The waviness in the powder bed lines up directly perpendicular to the motion of the powder recoating arm and seems to be indicative of the types of influences alluded to above in Section 2.1.2.

Below, in Figures 3.11 through 3.13, are select examples of the local surface map a particular pillar, showing cross sectional height traces. Height measurements for a subset of the 30 build layers can be found in Appendix A.

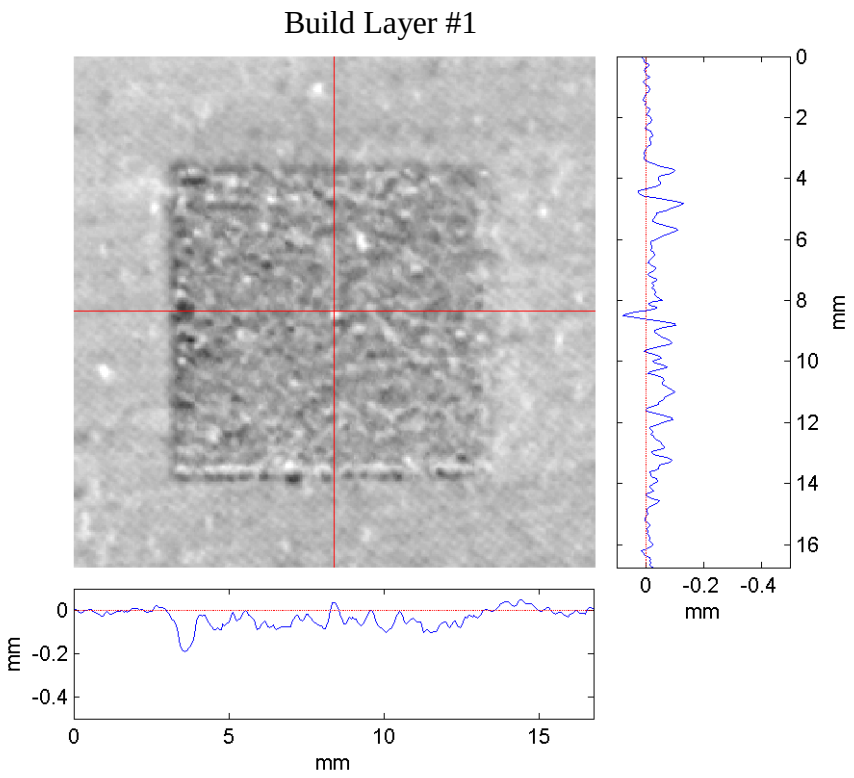

Figure 3.11: A close-up view of the height measurement for build layer 1 immediately after fusion of a particular pillar with cross sectional profile traces provided at bottom and right.

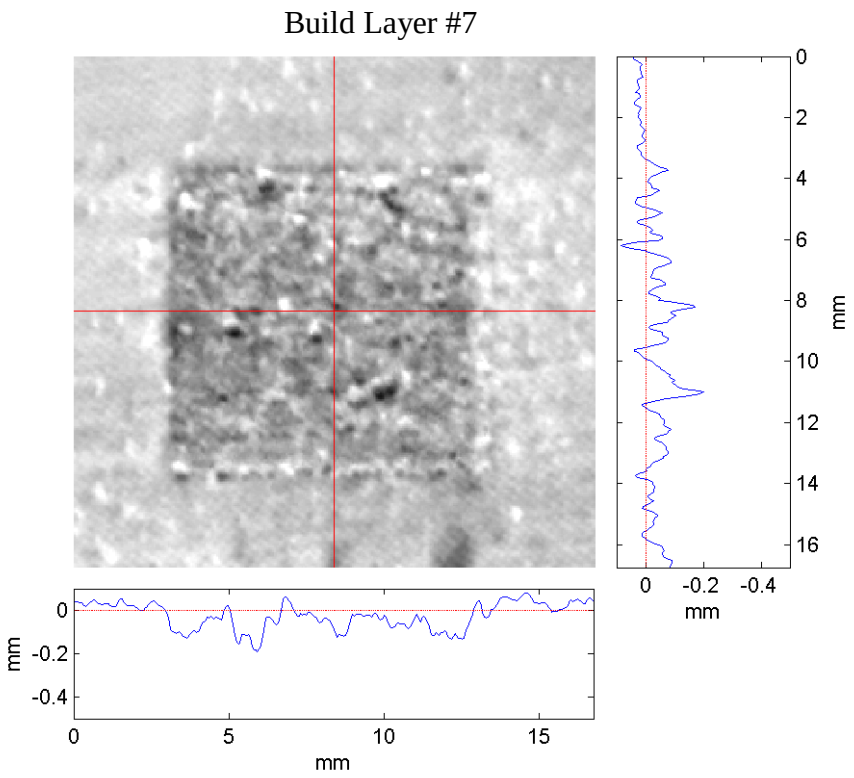

Figure 3.12: A close-up view of the height measurement for build layer 7 immediately after fusion of a particular pillar with cross sectional profile traces provided at bottom and right.

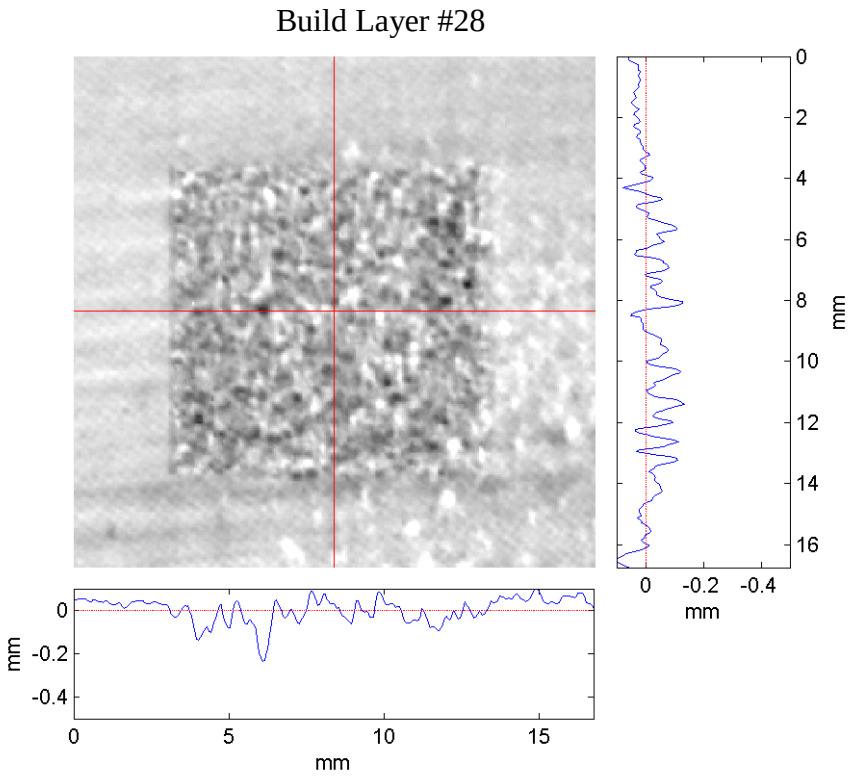

Figure 3.13: A close-up view of the height measurement for build layer 28 immediately after fusion of a particular pillar with cross sectional profile traces provided at bottom and right.

Additionally, by comparing the second and third measurements made during each build layer cycle as described by Figure 3.6, the build platform's relative height drop per layer was tracked. This information is important as a means of verifying the thickness of fresh powder distributed each cycle. Deviations from the nominal height drop can cause errors in the built part as enumerated in Section 2.1.2. Figure 3.14 shows the tracking of build platform height drop as a function of layer number, as calculated by subtracting the average height of the second and third measurements made during each layer cycle.

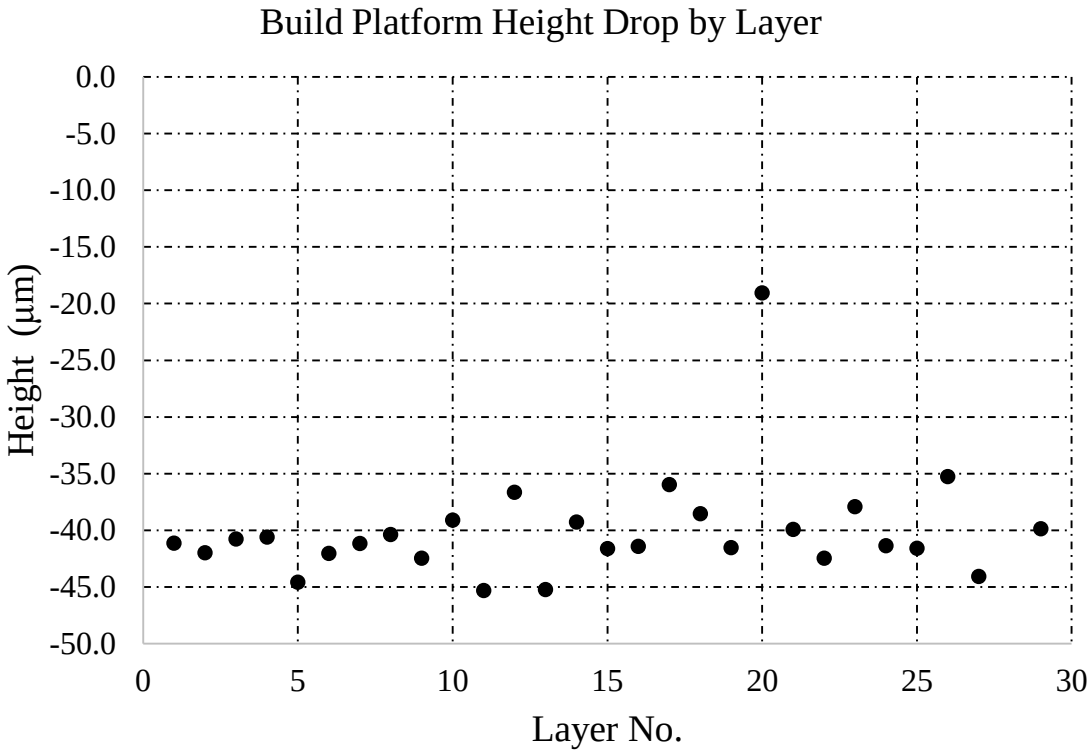

Figure 3.14: The tracking of the build platform's relative height drop after each build cycle through the thirty layer build.

3.4.3 Summary & Conclusions

There are several important takeaways from the results presented above. Primarily, there is clear qualitative ability to distinguish the fused and unfused powder area when visibly examining the areal height maps produced by the measurement system. As a stated goal of this measurement process is the distinction of fused area, it is encouraging to not only verify that the powder is consolidating at anticipated levels, but that this consolidation is detected by the developed metrology system. However, equally as important is the acknowledgment that this distinction is not the result of a simple relative height drop analysis as hoped. The average height of the fused area is clearly below the initial measurement of the unfused powder for each layer. Unfortunately, this height drop is muddled by the gross increase in roughness of the fused area. While visibly, it

seems qualitatively easy to distinguish the fused squares from the surrounding powder, it becomes more mathematically complex to robustly discern the two when you consider the level of surface texture seen in the fused area. One possible solution is to use the increased roughness as a parameter with which to distinguish fused from unfused area. Rather than solely looking for a height drop, a search algorithm could also include a search for increased roughness. Further data analysis must be carried out on the acquired height measurements to investigate efficient ways of post processing the data.

In addition to gaining insight into the surface texture of fused powder, the measurement results show that the system has to ability to see surface textures likely imparted onto the unfused powder as a result of the powder recoating arm's motion. It is valuable for fusion chamber operators to know what the quality of the powder lay is prior to fusion not only to ensure precision within the additive process, but as a means of monitoring machine performance over time. Likewise, Figures 3.9 and 3.10 demonstrate that the measurement system can distinctly show areas where the powder bed has been disturbed by particulate matter being dragged across it by the recoating arm. This information is also valuable information to the operator as these powder disturbances could lead to build errors such as porosity or interstitials in subsequent layers.

Finally, utilizing the second and third measurements of each build cycle allows for a verification of build platform step height consistency. This measurement adds a layer of versatility to the systems capability, and as demonstrated by Figure 3.14h, can help quantify and alleviate some of the potential effects of build platform motion errors on the output part of the system.

3.5 Uncertainty Analysis of the Lateral Measurement Process

As described above, the metrology system developed can be separated into two independent parts, the lateral conversion of pixelated image space to discrete metered space and the vertical conversion of pixelated phase information into discrete height information. As the data processing of these two conversions happen independently of each other, an individual uncertainty analysis must be carried out for both parts of the process. The drivers of the uncertainty in converting pixelated image space into discrete metered units are the measurement of the calibration grid plate itself, and the image processing steps used in its analysis. These two uncertainty contributors have many influences, acting independently on the two separate steps, and some of them have been quantified below.

3.5.1 CMM Measurement Uncertainty of Grid Plate

As previously discussed, the computer vision conversion from pixel coordinates to metered units is carried out by a map of localized linear scaling factors. This map is of the utmost importance to an accurate lateral measurement of a part made within the laser fusion chamber. The key component in the creation of this scaling map is the reference grid plate used to create each localized scaling factor. Therefore, the uncertainty in the lateral conversion of pixel space into metered space can be separated into two contributing steps, the uncertainty in the measurement of the grid plate to be used as reference dimensions and the uncertainty in the image processing used to determine the location of grid plate locations in image space.

The first contributor is the contact CMM measurement of the grid plate reference artifact, as discussed above. The reference grid plate consists of an 11 by 11 grid of reamed 7.5 millimeter diameter holes. They are arranged with a nominal two dimensional pitch of

15 millimeters, thereby covering an area of 150 by 150 millimeters. The specific measurand to be analyzed to quantify the uncertainty in the grid plate measurement is the position in X and Y (only) of the center of each cylindrical hole from the established origin at 20 degrees Celsius. The coordinate system of the plate has been defined by using the center hole's location as the origin. A linear regression of the center horizontal row of holes established the X-axis of the grid plate, and the normal vector of the least squares best fit plane of a scan of the plate's upper surface was used in conjunction with the X-axis to establish a Y-axis through the origin.

In order to construct the coordinate system discussed above and determine the relative position of each hole center, what is considered the center of each hole had to be defined and calculated. For this analysis, a singular scanned profile of each hole, 1.5 millimeters below the top surface of the plate, was used to establish its center using a least squares circle fit to approximately 1000 data points. The profile was taken near the top because the imaging system will be comparing the hole centers to values on the upper surface of the plate. The vector data for each hole scan is compared to the parametric definition of a circle, show below in Eq. 12 and 13, centered about an intial hole center guess as a means of initializing the least squares fitting algorithm.

$$x = z_1 + rcos(\phi) \tag{12}$$

$$y = z_2 + rsin(\phi) \tag{13}$$

In this case, the average X and Y position of each hole's data set is used as an acceptable initial guess of the circle center, seen above as (z_1, z_2). Then, each point's radius from the initialization guess is assembled and averaged to provide an initial guess for r within Eq. 12 and 13. The goal in determining the best circle center constitutes minimizing the sum

of squares of the distance of each data point to the parametrically defined circle as shown in Eq. 14 and 15, below. As such, Eq. 15 is used as the fitness function for running an optimization algorithm which varies z_1, z_2, and r in order to minimize the fitness function output.

$$d_i^2 = [(x_i - x(\phi_i))^2 + (y_i - y(\phi_i))^2] \tag{14}$$

$$\sum_{i=1}^{m} d_i^2 = minimum \tag{15}$$

This process was repeated for each of the hole scans from the plate measurement, outputting the best fit center, (z_1, z_2), as defined above [21].

The least squares defined hole centers are then used in the definition of the measurand, which is the relative position of the holes within the coordinate system established above. The measurand equation is shown below in Eq. 16, and includes recognition of CMM errors propagated through the least squares circle fit, CMM errors between the measurement of hole center positions within the machine volume, thermal expansion error, and probe form errors.

$$P_m(x, y) = P_m(z_{1_m}, z_{2_m}) + \varepsilon_{CircleFit} + \varepsilon_{CMM} + \varepsilon_{Temp} + \varepsilon_{Probe} \tag{16}$$

The goal of the CMM measurement of the grid plate was to achieve an expanded uncertainty of 10 parts per million with a coverage factor of two. This equates to a 2 micrometer measurement uncertainty or less over the full grid plate. The thought being that this level of measurement uncertainty would essentially make overall contributions from the artifact measurement negligible to the creation of the localized scaling map, as the image processing step was anticipated to have an order of magnitude larger contribution, as will be discussed below. As such, the two contributors of concern to the

CCM measurement of the grid plate artifact were the calibration errors provided by the manufacturer and the environment in the metrology lab during measurement.

Temperature can have a large influence on CMM measurements, particularly in the case of measuring aluminum such as in this instance. However, this particular measurement was carried out in a very well controlled environment, with temperature fluctuations below 0.3 degrees Celsius from standard temperature and pressure. As the CMM software performs a temperature correction calculation to all data, the measurement uncertainty contributions from differential thermal expansion and temperature variation are small compared to what they might have been. Assumed uncertainty in temperature measurement is only 0.1 degrees Celsius.

As stated, the tactile probe system has documented uncertainty associated with the probe's form and the electronics involved, but these are much smaller than the other contributors and will be neglected. The most dominant uncertainty however was the stated calibration error of the CMM, specified by the manufacturer as the maximum permissible error (MPE) described by Eq. 17.

$$MPE = 0.5 + \frac{\Delta L\ [mm]}{500} \quad [\mu m] \tag{16}$$

This specification of CMM measurement uncertainty propagates through the least squares circle fit of each hole scan. To estimate the measurement uncertainty associated with the CMM's MPE in the determination of each hole center, a type B Monte Carlo analysis was performed on each circle fit. Each data point within a scan was allowed to vary based on an assumed uniform uncertainty distribution of the magnitude of MPE across the diameter of the hole, in this case 0.502 micrometers. The X and Y data points for each scan were allowed to vary independently during the Monte Carlo simulation. The

estimated uncertainty in the least squares circle fit as determined via Monte Carlo simulation is another contributor to combined standard uncertainty in the measurement of the grid plate, alongside CMM calibration error and material thermal expansion.

As stated in Eq. 16, the MPE of the CMM varies linearly with the distance over which a measurement is taken. As such, its contribution with respect to location within the grid plate is a downward pointing cone centered at zero. Since it is preferable to use a singular value for the combined standard uncertainty of the plate measurement, the largest possible contribution of CMM calibration error, 0.72 micrometers, is conservatively taken as the calibration errors contribution, applied as a uniform distribution over the entire plate area. Additionally, the MPE must be applied, as discussed, in the Monte Carlo simulation of uncertainty in the least squares circle fitting algorithm. Applied over the nominal diameter of each hole, the MPE gives 0.50 micrometers of uniformly distributed uncertainty in the measurement of the relative position of each data point that make up the CMM scans of each hole. This uniform distribution was then allowed to propagate through the circle fit algorithm in a simulation of one million iterations of a circle fit. The circle fitting algorithm, whose only used output is the circle center, acts to average all of the data's uncertainty. The resulting estimated uncertainty contribution from the circle fitting algorithm was less than 30 nanometers.

Lastly in the calculation of measurement uncertainty for the grid plate artifact, the law of propagation of uncertainty was applied to the contribution of material thermal expansion described by Eq. 17, below [15].

$$\varepsilon = \alpha L \Delta T \tag{17}$$

The coefficient of thermal expansion, α, for 6061 aluminum was estimated to be 23.6 ppm/°C, and the maximum length, L, corresponding to the diagonal of the plate, 212 millimeters. The temperature, ΔT, is nominally zero with an uncertainty of 0.1°C. These factors produce an uncertainty contribution from material thermal expansion of approximately 0.50 micrometers. It is worth noting that this is the maximum uncertainty contributed by material growth; it like MPE increases linearly with distance from the origin of the plate measurement, and therefore consists of a downward pointing cone as well when mapped versus position within the plate. A summary of the considered uncertainty contributors and the combined standard uncertainty in the grid plate artifact CMM measurement is shown below in Table 3.1.

Table 3.1: Summary of measurement uncertainty contribution from the contact CMM during characterization of the grid plate reference artifact used for lateral camera calibration.

Ziess Prismo Navigator VAST Gold Tactile Probe Head	
Uncertainty Source	Contribution [µm]
MPE, Full Grid Plate	0.72
MPE, LS Circle Fit	0.03
Differential Thermal Expansion	0.50
Combined Standard Uncertainty	0.87

It should be noted that form errors of the grid plate as well as distortion due to mounting have not been considered above. Variations in the flatness of the plate as well as the cylindricity of the holes will influence measurement uncertainty due to the definition of the coordinate system. Part form errors are influential in all task specific uncertainty analysis as documented by Wilhelm, et al. [22]. However, the form errors of this particular plate

were measured via the CMM and found to be very low in both of the pertinent geometrical constraints mentioned. As such, they were expected to also have negligible influence relative to the MPE and thermal expansion contributions outlined above.

3.5.2 Uncertainty in Conversion of Pixelated to Metered Space

The other step in converting the pixelated image space into metered space is the analysis done on the images of the grid plate artifact described above. Just like the measurement of the grid plate by tactile CMM probe, the processing of its images has many influences which contribute to its measurement uncertainty. Some of these contributors include lighting conditions during imaging, the focal and geometric stability of the system during imaging, and noise in the sensor array. These examples enumerate just a few of the small fluctuations that will affect the contrast transition algorithm used to fit circles to the image of the grid plate. As discussed in Section 3.2.1, the determination of each grid plate hole center in the image space is compared to its relative location in global space as measured by the CMM. Therefore, fluctuations in the determination of each grid plate hole directly impacts measurement uncertainty.

Quantifying the uncertainty related to the creation of the localized linear scaling map was carried out via a statistical analysis. Ten images of the grid plate artifact were collected in rapid succession as to eliminate drift effects. Each image was then passed through the analysis procedure outlined earlier in the chapter, and the variance of each individual hole location in X and Y pixel space was calculated. The maximum standard deviation of any hole location in any direction was taken as the measurement uncertainty for creating the scaling map.

Although quantifying the uncertainty related to scaling map creation is relatively straight forward, what is difficult to determine is how ineffective the use of a bilateral interpolation between scaling locations is at correcting true image distortion. In the distortion map shown in Figure 3.3 there are some signs that linear interpolation between points might be inadequate. There are some changes in directionality of scaling correction between three scaling points, and there are known second order radial distortions due to the lens objective in use. However, without further testing quantification of linear interpolations contribution to uncertainty is nearly impossible. For this simplified uncertainty analysis, an assumed inadequacy of one pixel will be used as a way of including some contribution in a subjective manner. It is likely that a more complicated camera calibration method will need to be implemented in order to better understand and quantify the image processing's effect on measurement uncertainty. Below is a summary of the uncertainty contributions from the image processing step during conversion from pixelated image space to global metered space by grid plate reference artifact calibration.

Table 3.2: Summary of measurement uncertainty contribution from the contact CMM during characterization of the grid plate reference artifact used for lateral camera calibration.

Image Processing Uncertainty Contribution Grid Plate Artifact Imaging	
Uncertainty Source	Contribution [µm]
Repeatability of Measurement, 1.3 [pixels]	78
Bi-Linear Interpolation, 1.0 [pixels]	60
Resolution, 1.0 [pixels]	60
Combined Standard Uncertainty	120

The contributions from the two steps of the lateral measurement discussed above are assumed to be uncorrelated influences on measurement uncertainty. As a result, their uncertainty contributions can be combined in root sum square fashion, as described by the GUM [15]. Below, in Table 3.3, is a summary of total uncertainty in the lateral measurement process by the machine vision portion of the imaging system.

Table 3.3: Summary of total estimated measurement uncertainty in the lateral measurement process by the metrology system developed above.

Image Processing Uncertainty Contribution Grid Plate Artifact Imaging	
Uncertainty Source	Contribution [µm]
CMM Grid Plate Measurement	0.87
Grid Plate Image Processing	120
Combined Standard Uncertainty	120
Expanded Uncertainty (k=2)	**240**

CHAPTER 4: PATHWAY TO PRECISION IN ADDITIVE MANUFACTURING

4.1 Pathway to a Precision Machine

The first step to improving additively produced parts must be applying the near century's worth of accumulated knowledge in precision machine design to the new generation of additive manufacturing machines. Specifically, the practice of volumetric machine tool error modeling and correction must be applied to all additive manufacturing machines. Geometric error modeling has long been applied to subtractive machine tools, and is documented in countless textbooks and publications, such as in Slocum [6].

A geometric error model of the powder bed fusion system discussed herein could alleviate or correct for nearly all of the induced part errors caused by the machine errors described in Chapter 2. A perfect example would be the modeling and correction of induced part errors caused by the build platforms straightness and average orthogonality error, as described by Figure 2.2. In modeling the two directional straightness errors and orthogonality of the build platform as a function of machine position, the laser spot placement could account for and correct the area of fused powder per layer to eliminate induced part error. Figure 4.1 shows the same build platform errors as those described by Figure 2.2, but with layerwise correction to the potential part errors, a high precision part can still be produced. The same volumetric error modeling and correction could be used to correct for build platform's yaw, pitch, and roll effects on the laser spot's placement accuracy as described in Chapter 2.

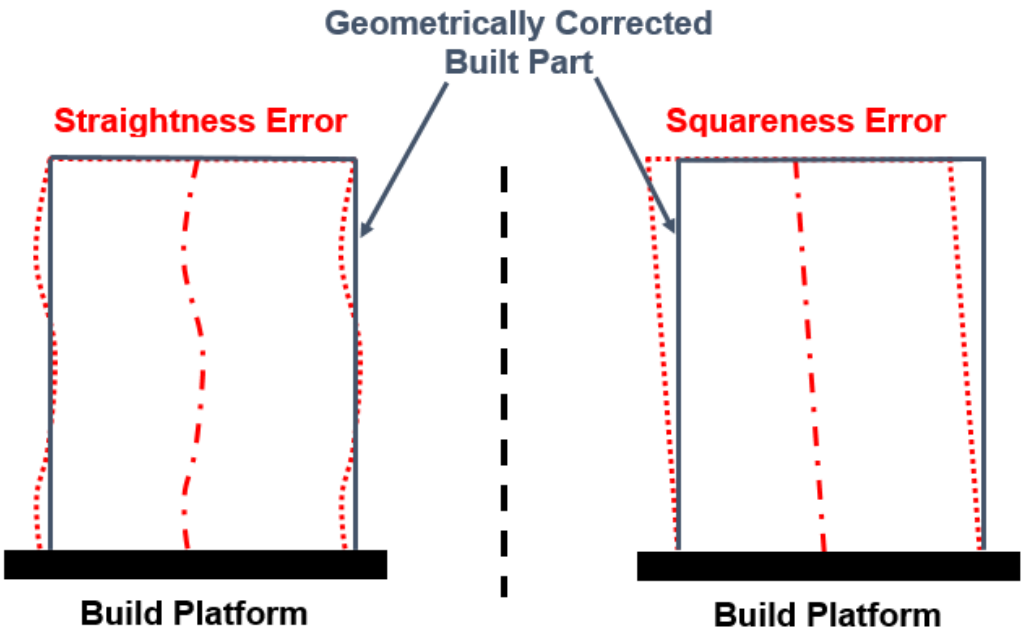

Figure 4.1: Schematic showing the build platform's two directional straightness error (left) and squareness error's (right) potential to induce part errors. However, with these geometric errors modeled and corrected for, their influence can be eliminated from the built part (shown in blue).

Additionally, the mapping and correction of the f-theta lens' distortion of the laser spot's placement accuracy can eliminate its associated part errors to within the measurement uncertainty of the laser spot's position throughout travel.

The only part errors induced by machine component motion that could not be actively corrected for with a complete model of the machine's geometric errors would be those imparted by the recoating arm. However, the principles of symmetry, minimization of abbe offset, and minimizing moment loads on the support structure could be applied to the particular design of the recoating arm in this chamber to drastically reduce the magnitude of its error motions. For example, a bridge support structure, as opposed to a cantilever, would improve the angular errors of the arm's motion due to the heavy offset load. Likewise, the mapping of the recoating arm's errors and their potential to induce part errors would at the least allow for a proper error budget.

Finally, probably the largest contributing group to uncertainty and manufacturing error in this type of process is the thermal effects, which have been neglected for the most part at this point in the research. The powder bed fusion system studied here is operated at an elevated temperature, with large heat sources purposefully integrated into the build platform. Considering the length of the build process (which can be days) and the dynamic heat input from the laser system, there is very little ability to determine the thermal gradients and likewise the differential expansion effects between machine components or the powder bed/part. Just as with the other contributors discussed, the first step is data collection and error budgeting.

The creation of a comprehensive error budget is perhaps the most important aspect of a machine model. It is folly to presume the creation of precision parts without fully understanding the capabilities of one's machine. Knowing the desired tolerances of the parts to be produced and understanding the implications of machine errors are the basics of determinism and precision machine design. Without a volumetric machine error model, insight into the potential thermal effects, and an appropriate part error budget, one lacks the foundation with which to pursue precision manufacturing.

4.2 Pathway to Precision Geometrical Measurement

Just as in traditional manufacturing, there is a definite need for in-process measurement of several aspects of the laser powder fusion process. As discussed in Chapter 1, one of the principle challenges of producing parts additively is the difficulty in measuring their geometric features after the part has been manufactured. Often these features are complex and irregular in shape, and often there exists internal and obscured surfaces which are

unavailable for probing once the part is in final form. It is the assertion of this project that these challenges can be met with in-situ geometric measurement of the build process.

The metrology system developed in this project has the potential to satisfy many of the needs for geometric measurement of the built part, in its entirety. There exists some potential to distinguish between fused and unfused powder area. Although this distinction may not be achieved by simply looking for a relative drop in height as hoped, there are certainly characteristic differences in the profiles of fused and unfused regions that could be exploited for determination. If the distinction of fused powder could be determined with high enough fidelity, the geometric characterization of the entire part, including all internal and externally obscured features, is readily possible. Such capability would solve many of the post process metrology difficulties described in the introduction. However, in order for a system such as the one developed herein to accomplish such a measurement, several improvements need to be made to both the system hardware and the process.

Of the possible ways to improve the measurement fidelity and accuracy of the metrology system developed in this project, the first approach should be to increase pixel density on the measured area of interest. Currently, the system is using relatively cheap, lay consumer oriented cameras that could be upgraded to professional metrology oriented cameras. Similarly, the pixel efficiency of the current arrangement is very low, with approximately 70% of the available pixels focused on the actual build area, and a much fewer percentage used on fused powder and surrounding areas. Adjusting the zoom and field of view of the camera system to achieve higher pixel density would be an easy way to get increased lateral resolution and an improvement in vertical height measurement.

In similar fashion, the digital projector used in this system was selected primarily due to cost and form factor considerations. It too could be replaced for a projector with a higher pixel count, allowing for a higher spatial frequency of the projected fringes and a higher signal to noise ratio in the vertical measurement. The increase in measurement fidelity and accuracy is not as straightforward to predict as it is when increasing the camera pixel density, but replacing the projector would be another quick and easy way to improve the metrology system.

When first introduced, the system was described as only using one of three available cameras for performing measurements. This leaves room for improvement in the measurement process itself. Due to the geometric arrangement of each camera to the build area, no one camera can get an undistorted view of the real areal profile. Features will always be obscured due to viewing angle, and the true shape of features is (predictably) distorted from the perspective effect. By using all three camera images, it is possible to perform averaging and combination of the information contained to arrive at a more accurate measurement of the surface. This convolution could take significant software development, but the potential for improvements in both measurement resolution and uncertainty is tremendous.

Finally, as with all precision measuring devices, the output of the digital fringe projection system employed in this metrology process must undergo a rigorous measurement uncertainty analysis. Areal profile measurements are very complicated, and their associated uncertainty is spatial bandwidth dependent. A deeper understanding of the major uncertainty contributors and their implications on various spatial ranges of the measurement data is important to develop to achieve a worthwhile measuring machine. It

has already been discovered that variations in fused surface specularity due to surface lay from varying fusing strategies can greatly influence measurements from layer to layer. Precision employment of such a measurement strategy is impossible without a well understood device.

4.3 Pathway to Precision Parts

There are a tremendous number of input parameters and physical processes that impact the overall product of the laser powder bed fusion process. As discussed by Taylor, the pathway to precision part creation lies in the linking of these input parameters through their respective physical process impacts to the resulting part features and characteristics [23]. The key to discovering these links is data collection and correlation. Below, Figure 4.2 shows a schematic of a part made via powder bed fusion, and connects just a few of the input parameters to their possible effects in part outcome.

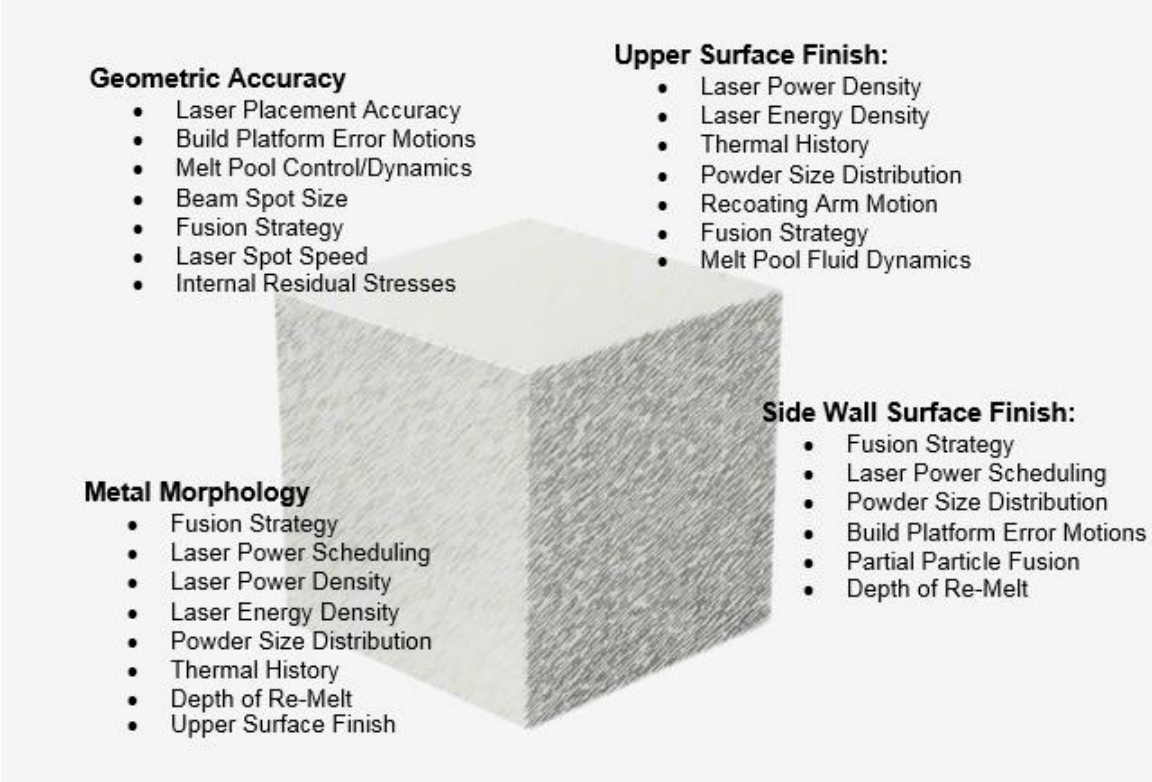

Figure 4.2: Enumerated build parameters separated by their potential impact on different features of the finished built part.

Introduced in the literature review, the development of thermography systems for monitoring melt pool temperatures and dynamics has great potential to provide valuable information about the fusion process. Melt pool monitoring can potentially lead to a volumetric thermal history of the part, which could lead to volumetric prediction and planning of grain structures and metal morphology. Additionally, incorporating melt pool edge determination into geometric measurements of the process could provide a much higher fidelity measurement and prediction of final part boundaries.

Incorporating other in-situ monitoring systems, such as thermographic data, with measurement systems such as the one developed in this project into a unified data collection and analysis protocol for the eventual qualification, standardization, and regulation of additively produced metal parts is one of the major steps necessary to

understand and control with deterministic results the many additive manufacturing processes. It is not inconceivable that eventually, the same software that is used to produce the part also collects and analyzes the data from many monitoring systems and produces a part qualification form containing geometric accuracies, metal morphologies, and levels of potential residual stresses. Although the goal of achieving high precision, high functionality parts is potentially far in the future, data collection and correlation is the first step down the path.

REFERENCES

[1] Wohler, T.T., “Wohlers Report 2013: Rapid prototyping & manufacturing state of the industry.” *Annual Worldwide Progress Report*. Wohlers Associates. (2012).

[2] Mani, Mahesh, et al. "Measurement Science Needs for Real-time Control of Additive Manufacturing Powder Bed Fusion Processes." *Natl. Inst. Stand. Technology IR 8036.* (2015).

[3] Slotwinski, J. A., et al. "Characterization of metal powders used for additive manufacturing." *J. Res. Natl. Inst. Stand. Technology* 19 (2014).

[4] Xiao, Bin, and Yuwen Zhang. "Partial melting and resolidification of metal powder in selective laser sintering." *Journal of thermophysics and heat transfer*20.3 (2006): 439-448.

[5] Simchi, A. "Direct laser sintering of metal powders: Mechanism, kinetics and microstructural features." *Materials Science and Engineering: A* 428.1 (2006): 148-158.

[6] Slocum, Alexander H. *Precision machine design*. Society of Manufacturing Engineers, 1992.

[7] Moylan, Shawn, et al. "Infrared thermography for laser-based powder bed fusion additive manufacturing processes." *40TH ANNUAL REVIEW OF PROGRESS IN QUANTITATIVE NONDESTRUCTIVE EVALUATION: Incorporating the 10th International Conference on Barkhausen Noise and Micromagnetic Testing*. Vol. 1581. No. 1. AIP Publishing, 2014.

[8] Dressler, M., et al. "Temperature distribution in powder beds during 3D printing." *Rapid Prototyping Journal* 16.5 (2010): 328-336.

[9] Dinwiddie, Ralph B., et al. "Thermographic in-situ process monitoring of the electron-beam melting technology used in additive manufacturing." *SPIE Defense, Security, and Sensing*. International Society for Optics and Photonics, 2013.

[10] Moylan, Shawn, et al. "Proposal for a standardized test artifact for additive manufacturing machines and processes." *Proceedings of the 2012 Annual International Solid Freeform Fabrication Symposium*. 2012.

[11] Bauza, Marcin B., et al. "Study of accuracy of parts produced using additive manufacturing." *Proceedings of the 2014 ASPE Spring Topical Meeting on Dimensional Accuracy and Surface Finish in Additive Manufacturing.* (2014). 86-91.

[12] Kruth, Jean-Pierre, et al. "Lasers and materials in selective laser sintering." *Assembly Automation* 23.4 (2003): 357-371.

[13] Gibson, Ian, and Dongping Shi. "Material properties and fabrication parameters in selective laser sintering process." *Rapid Prototyping Journal* 3.4 (1997): 129-136.

[14] Land. "Effective calibration and implementation of galvanometer scanners as applied to direct metal laser sintering." *Proceedings of the 2014 ASPE Spring Topical Meeting on Dimensional Accuracy and Surface Finish in Additive Manufacturing.* (2014).

[15] BIPM; IEC; IFCC; ISO; IUPAP; OIML. (1995). "Guide to the expression of uncertainty in measurement." Geneva: ISO TAG4.

[16] Zhang, Land, Ziegert, and Davies. "In-situ monitoring of laser powder bed fusion of additive manufacturing using digital fringe projection technique." *Proceedings of the 2015 ASPE Spring Topical Meeting on Dimensional Accuracy and Surface Finish in Additive Manufacturing.* (2015).

[17] Land, Zhang, Ziegert, and Davies. "In-situ metrology system for laser powder bed fusion additive process." *Proceedings of the 43rd NAMRC International Manufacturing Research Conference.* (2015).

[18] G. Wolberg. "Digital Image Warping." *IEEE Computer Society Press*. Los Alamitos, CA, USA, 1994. 41-56.

[19] Purcell, et al. "Effective wavelength calibration for moire fringe projection." *Applied Optics*. Vol. 45, No. 34. (2006). 8629-8635.

[20] Arai and Yokozeki. "Improvement of measurement accuracy in shadow moiré by considering the influence of harmonics in the moiré profile." *Optical Society of America*, 1999.

[21] Gander, Golub, and Strebel. "Least-squares fitting of circles and ellipses." *BIT Numerical Mathematics*, Vol. 34, (1994). 558-578.

[22] Wilhelm, Hocken, and Schwenke. "Task specific uncertainty in coordinate measurement." *CIRP Annals – Manufacturing Technology*. Vol. 50, No. 2 (2001). 553-563.

[23] Taylor. “Physical processes linking input parameters and surface morphology in additive manufacturing.” *Proceedings of the 2015 ASPE Spring Topical Meeting on Dimensional Accuracy and Surface Finish in Additive Manufacturing.* (2015).

APPENDIX A: MEASUREMENT RESULTS FOR A SELECTION OF CLOSE UP LAYER PROFILES FROM THE TEST BUILD AT EWI FACILITY

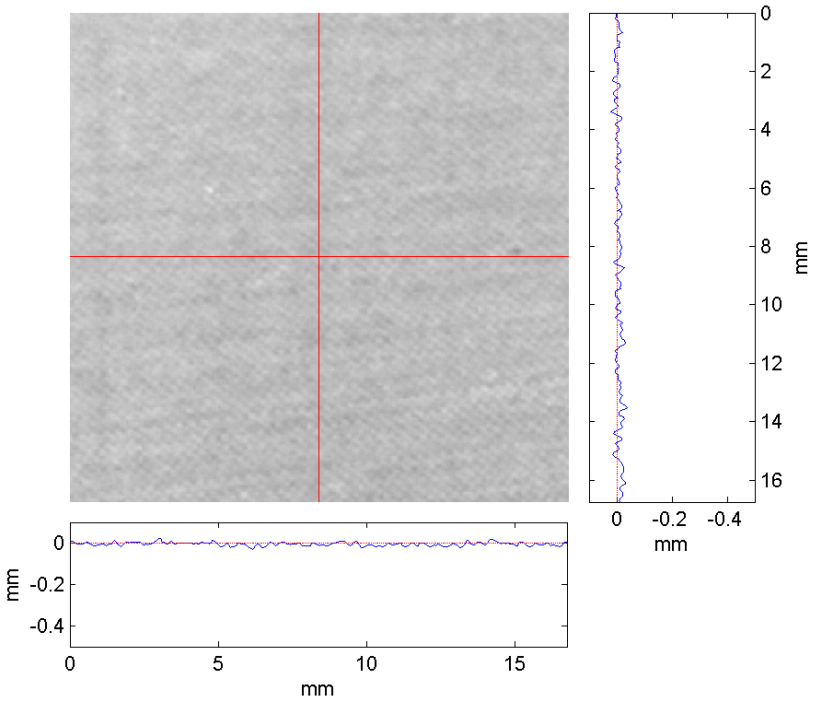

Figure A.1: A close-up view of the height measurement for build layer 1 immediately prior fusion of a particular pillar with cross sectional profile traces provided at bottom and right.

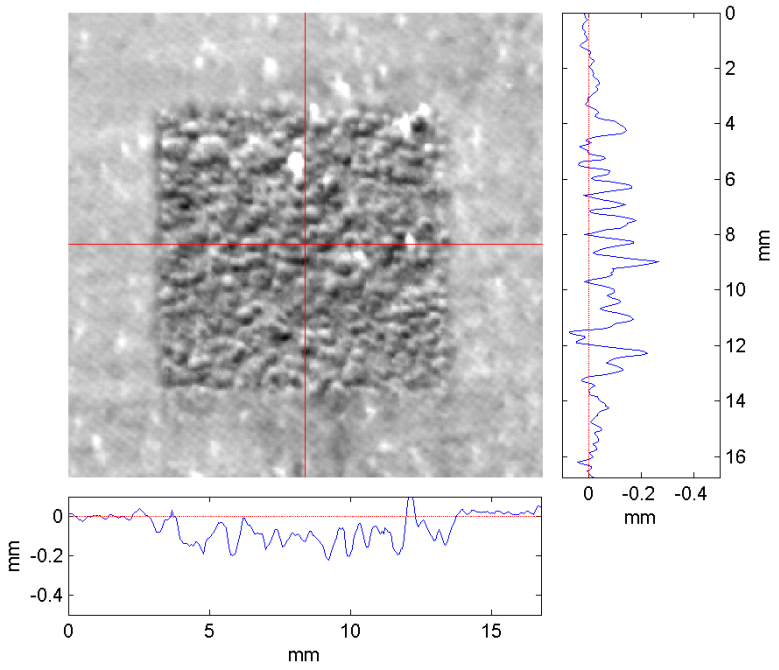

Figure A.2: A close-up view of the height measurement for build layer 1 immediately after fusion of a particular pillar with cross sectional profile traces provided at bottom and right.

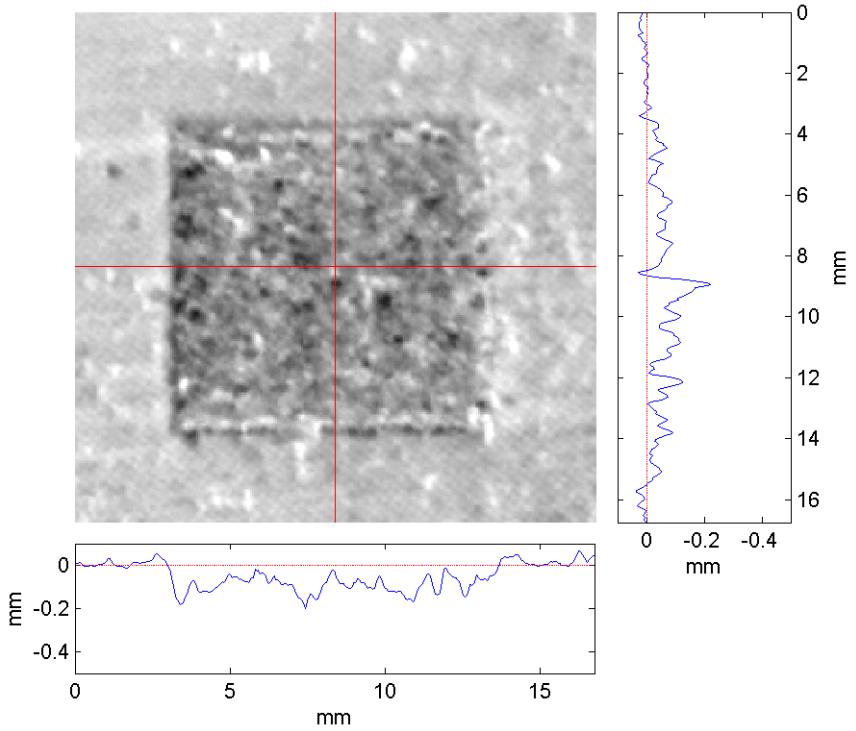

Figure A.3: A close-up view of the height measurement for build layer 2 immediately after fusion of a particular pillar with cross sectional profile traces provided at bottom and right.

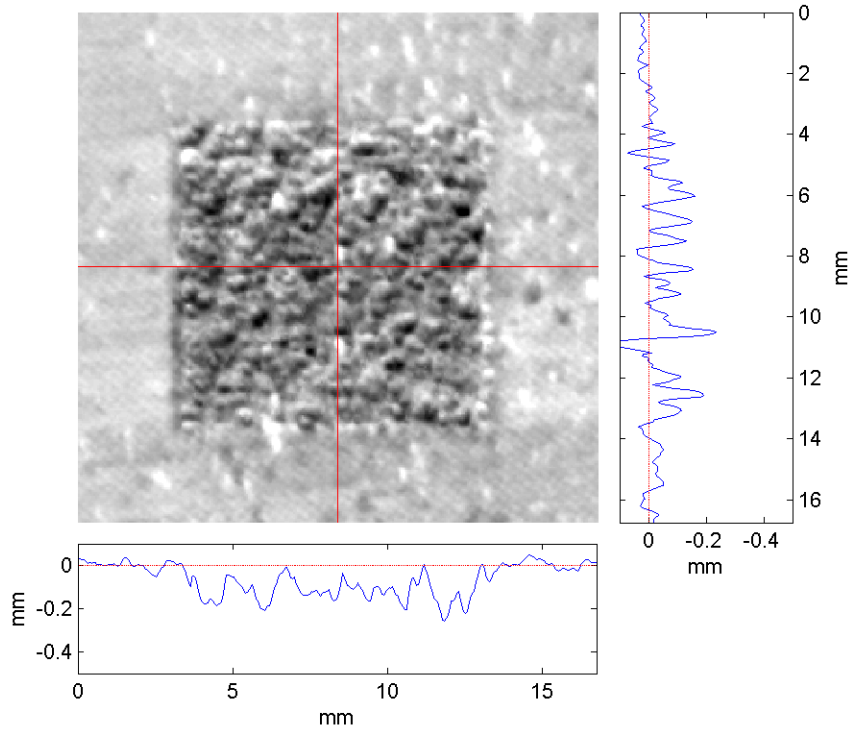

Figure A.4: A close-up view of the height measurement for build layer 3 immediately after fusion of a particular pillar with cross sectional profile traces provided at bottom and right.

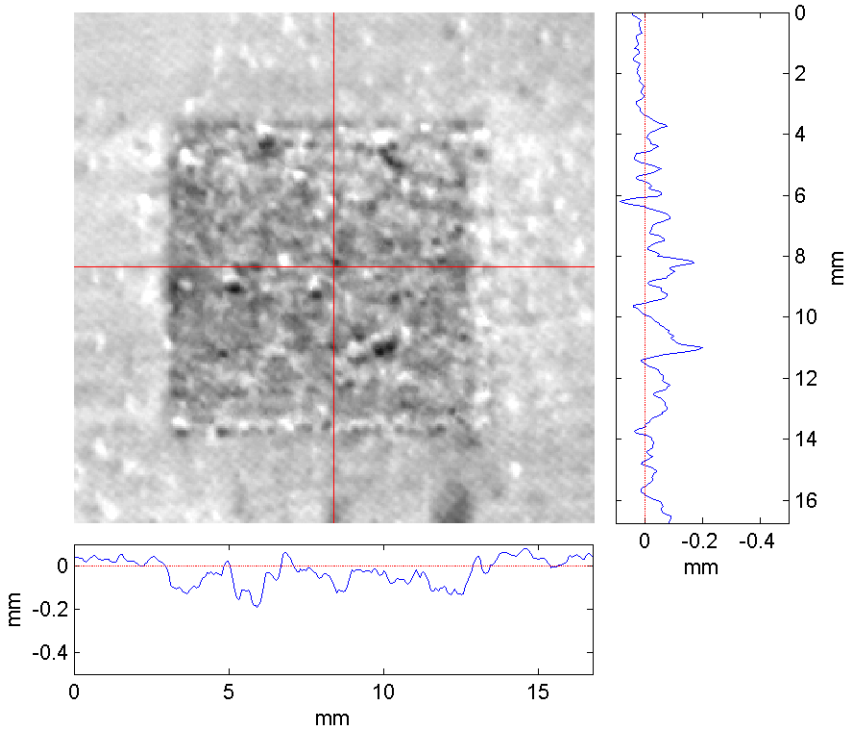

Figure A.5: A close-up view of the height measurement for build layer 5 immediately after fusion of a particular pillar with cross sectional profile traces provided at bottom and right.

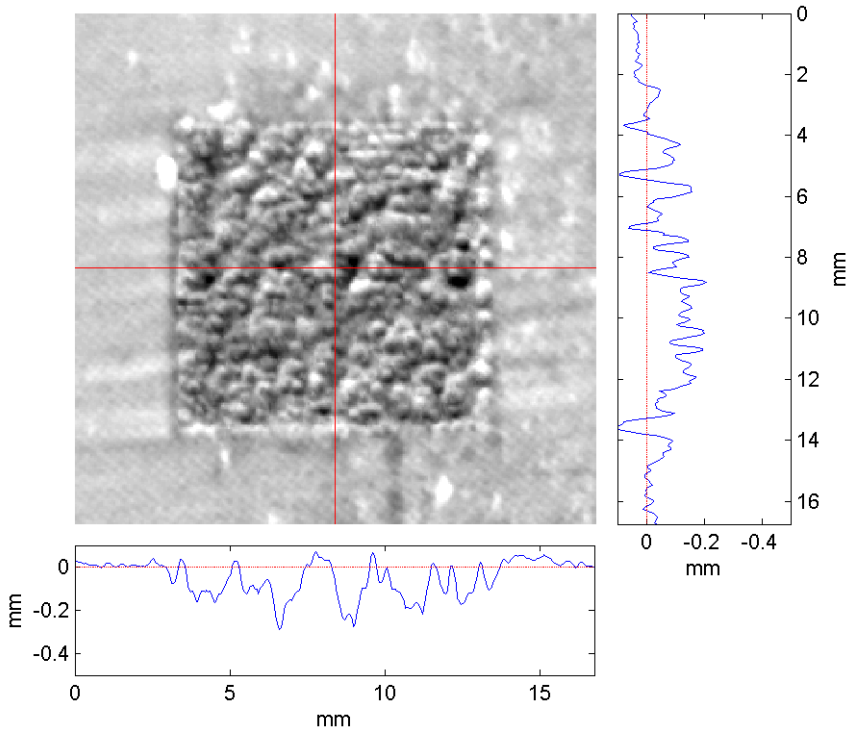

Figure A.6: A close-up view of the height measurement for build layer 10 immediately after fusion of a particular pillar with cross sectional profile traces provided at bottom and right.

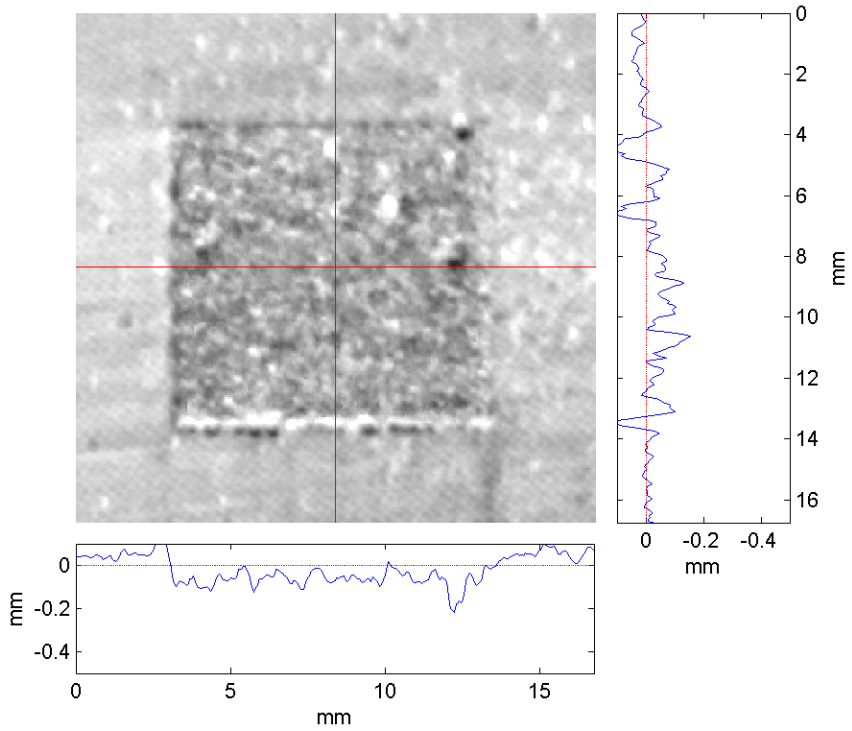

Figure A.7: A close-up view of the height measurement for build layer 15 immediately after fusion of a particular pillar with cross sectional profile traces provided at bottom and right.

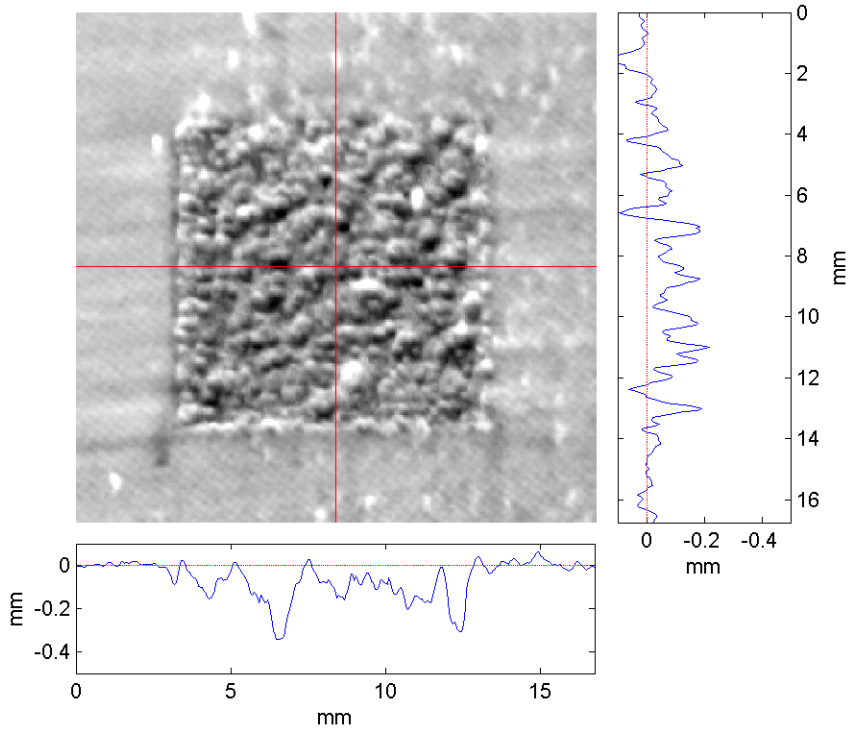

Figure A.8: A close-up view of the height measurement for build layer 20 immediately after fusion of a particular pillar with cross sectional profile traces provided at bottom and right.

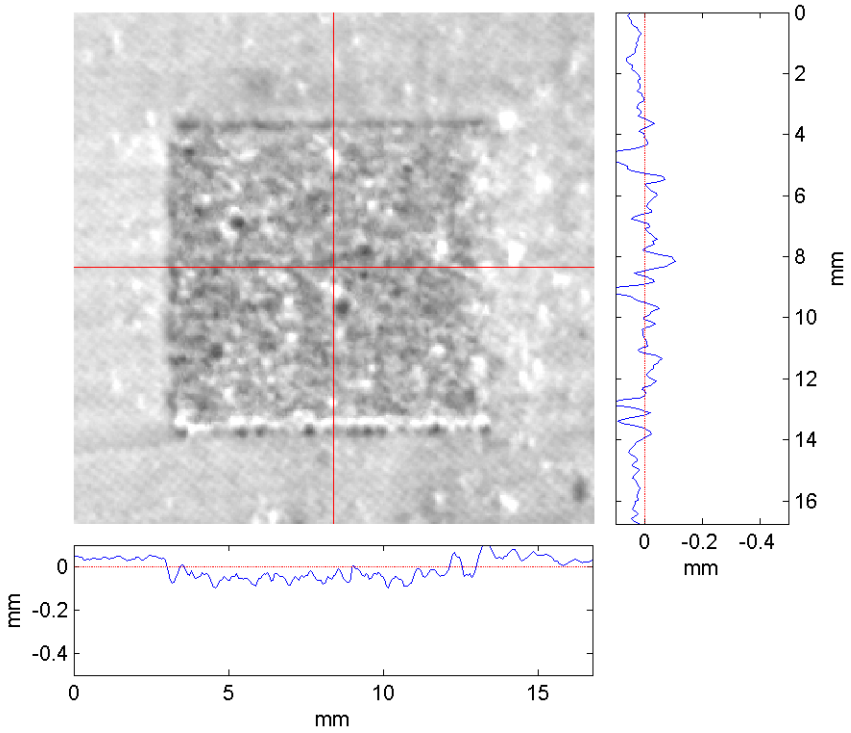

Figure A.9: A close-up view of the height measurement for build layer 25 immediately after fusion of a particular pillar with cross sectional profile traces provided at bottom and right.

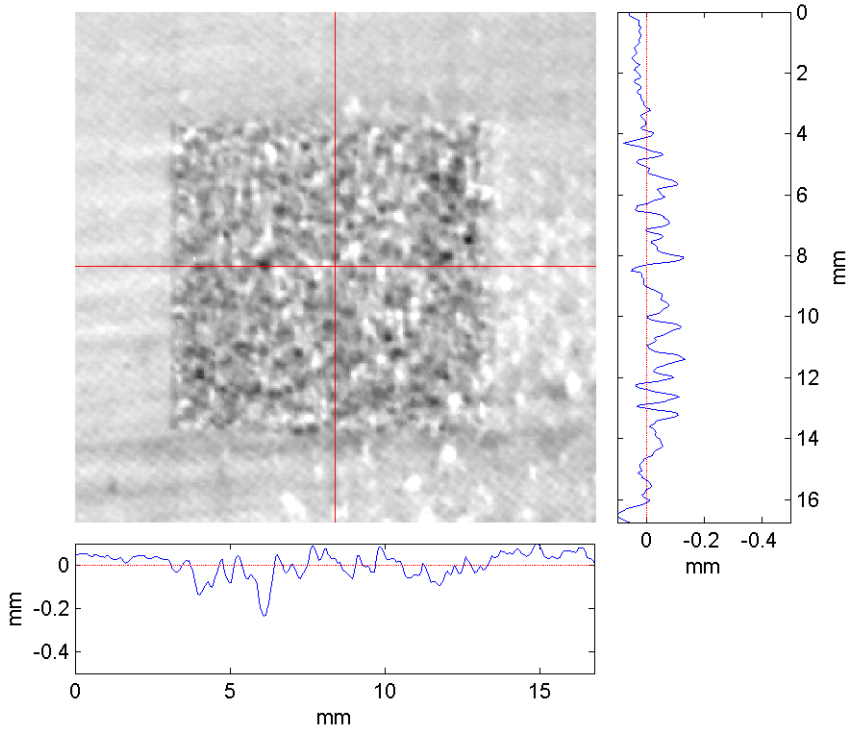

Figure A.10: A close-up view of the height measurement for build layer 30 immediately after fusion of a particular pillar with cross sectional profile traces provided at bottom and right.